8-2014

Experimental Terahertz Imaging and Spectroscopy of Ex-vivo Breast Cancer Tissue

Tyler C. Bowman
University of Arkansas, Fayetteville

Experimental Terahertz Imaging and Spectroscopy of Ex-vivo Breast Cancer Tissue

Experimental Terahertz Imaging and Spectroscopy of Ex-vivo Breast Cancer Tissue

A thesis submitted in partial fulfillment
of the requirements for the degree of
Master of Science in Electrical Engineering

by

Tyler C. Bowman
University of Arkansas
Bachelor of Science in Electrical Engineering, 2012

August 2014
University of Arkansas

This thesis is approved for recommendation to the Graduate Council.

Dr. Magda El-Shenawee
Thesis Director

Dr. Roy McCann
Committee Member

Dr. David Zaharoff
Committee Member

Abstract

This thesis presents experimental results of terahertz imaging and spectroscopy techniques to analyze excised breast cancer tissue. The pulsed terahertz system at the University of Arkansas was used to assess formalin-fixed, paraffin-embedded breast cancer tissue obtained from 22, 40, and 46 year old patients. The tissue for this research was sliced to relatively thin sections of 10 μm thick and mounted on glass slides. Terahertz reflection time and frequency domain images of the breast cancer tissue were then obtained and compared to histopathology slides from the same patient. Results showed good correlation between the reflection images and histopathology slides for the 40 and 46 year old patients. However, there were inconsistent results for the 22 year old patient, possibly due to the age of the patient. The measurements obtained from reflection imaging were also compared to the theoretical solution of the reflection coefficient. The theoretical solution used tissue properties found via terahertz spectroscopy. Thus the strong correlation of this comparison indicated good agreement between the two techniques.

Standard electromagnetic techniques were used to formulate the expression for spectroscopy of a single dielectric layer, and the results were validated against literature for the glass slide. Then the formulation was developed to find the properties of tissue on a glass slide via terahertz spectroscopy. A large number of points across the samples were measured to find the electrical properties of infiltrating ductal carcinoma and fibroglandular tissue up to 1.2 THz that best matched the analytical solution. Statistical analysis of the spectroscopy data showed distinct characteristics between the cancerous and normal tissue in the 40 and 46 year old patient consistent with the terahertz reflection imaging. However, there was a wide margin of error in these measurements due to the large absorption in the glass slide. Overall, terahertz was found to have a strong potential for applications with breast cancer tissue.

Acknowledgements

The Author would like to acknowledge Dr. Magda El-Shenawee for her work as the advisor and thesis director of this work, without which this thesis would not have been possible. He would also like to thank the committee members of this thesis, Dr. David Zaharoff and Dr. Roy McCann, for their participation and contribution to this work. The Author would like to thank the faculty of the Biomedical Engineering Department of the University of Arkansas for advice and support throughout this work, with special thanks to Dr. Wolchok and Dr. Zaharoff for the use of their lab space and equipment.

The Author would like to thank Dr. S. G. Sharma with the Department of Pathology at UAMS and Dr. Lucas Campbell with NWA Pathology and Associates for providing the histopathology assessment for this work. The Author also would like to thank Dr. Suzanne Klimberg, MD, Professor of Surgery and Breast Cancer Oncology at UAMS for providing the medical insight on breast cancer lumpectomy and margins that inspired this research.

Finally the Author would like to thank Dr. Taday of TeraVIEW, Ltd. for his training and feedback, the Computational Electromagnetics Group members at the University of Arkansas for their support, and all family and friends whose patience and support made this work possible.

Funding for the Pulsed Terahertz System used in this work was provided by NSF/MRI award #1228958. Student funding for this research was provided by the NSF GRFP, the NSF GK-12 Program as part of award #1228958, and the University of Arkansas Distinguished Doctoral Fellowship. This research was supported by a grant from the Arkansas Breast Cancer Research Programs (ABCRP). The University of Arkansas for Medical Sciences Translational Research Institute (CTSA Grant Award # UL1TR000039) provided resources during the review and selection process. Additional support was given by the Arkansas Biosciences Institute (ABI).

Table of Contents

I. Introduction

A. Motivation

Breast cancer is one of the primary medical concerns among women in the world today. In the United States an estimated 1 in 8 women will develop an invasive breast cancer, and breast cancer is the second most common cause of cancer-related death in women [1]. For breast cancer tumors with a diameter under 5 cm, one of the preferred methods of treatment is for the patient to undergo breast conserving surgery or lumpectomy [1],[2]. It has been shown that successful lumpectomy treatment greatly increases the survival rate from cancer to the same degree as full mastectomy [3],[4]. The objective of this procedure is to surgically remove the tumor as well as a sufficient amount of surrounding normal tissue from the breast. The tissue present in this surrounding region, known as the margin, is of critical importance when determining the success of the lumpectomy procedure. With conventional lumpectomy procedures, as many as 20-40% of surgeries are found to have an insufficient amount of removed tumor tissue [2]. Additionally, 75-90% of cases involving the local recurrence of breast cancer tumors following surgery are located within the surgical cavity [5]. However, the amount of healthy tissue removed by the surgery must also be minimized in order to avoid any significant cosmetic effects on the patient. Thus the ability to balance sufficient tumor removal with minimal negative impact on the patient is of key importance in treating breast cancer tumors via lumpectomy.

The standard technique for margin analysis of breast cancer tissue is pathology assessment. Following the lumpectomy procedure, the excised tissue is preserved in formalin and mounted in a paraffin block. This formalin-fixed, paraffin-embedded (FFPE) tissue is then sliced into thin sections with a standard pathology thickness of 4-5 μm and placed on glass slides. The section is stained using hematoxylin and eosin (H&E) for analysis by the pathologist. The

pathologist then classifies the tissue in the margin: positive with cancerous tissue extending to the edge of the excision, negative with no cancerous tissue within 2 mm of the edge, or close with cancerous tissue within 2 mm of the edge [5]. The detection of a positive or close margin typically results in a second surgery in order to remove the remaining cancerous tissue in the surgical cavity as a precaution to prevent local recurrence [6]-[11].

The pathology process for margin assessment is generally considered the gold standard by which all other applications are judged. However, there many concerns exist with using pathology assessment alone for finding positive margins following a lumpectomy. One drawback of the standard pathology procedure is the amount of time required to process the tissue from a freshly excised mass to a stained pathology slide for analysis. For this reason a full pathology analysis of the excised tissue can take several days to complete. In cases with a positive margin requiring a second surgery, this time delay can cause a significant burden on the resources of the medical provider and increases the financial, emotional, and cosmetic effects on the patient [10],[11]. Studies have shown that intraoperative margin assessment techniques have a strong potential to reduce the need for second surgeries [12]. While some methods exist for more rapid pathology assessment, such as frozen section analysis, these techniques are limited in the amount of the excised tissue that can be assessed at once due to pathology sections only observing 4-5 μm of tissue at a time. Additionally, in many cases a lack of pathology resources can prevent the entirety of the margin from being submitted for analysis, especially in the event that palpable abnormalities are not detected [2]. Finally, there is always the potential for human error in relying solely on pathology assessment. Thus there is a need to improve on the standard pathology technique for margin assessment in order to provide an analysis method with reasonable accuracy that can operate within the lumpectomy procedure.

Many techniques have been developed that attempt to address the problem of positive margins at two stages in the lumpectomy procedure: (i) better localization of the tumor prior to surgery and (ii) improved margin assessment and tumor removal during surgery. The most common technique for detection and localization of the tumor prior to surgery is the use of portable X-ray mammography. This method is often used in conjunction with ultrasound in order to provide a clearer picture of the tumor location, size, and shape. However, mammography alone has been shown to have some limitations in detecting the full extent of the tumor [2]. The use of magnetic resonance imaging (MRI) has gained popularity as a preoperative assessment tool of the tumor, but clinically it has not been shown to significantly improve the rate of positive margin occurrence [13]. MRI also tends to be very costly compared to other localization methods. Thus even with advancing preoperative localization there is still a need for improved intraoperative margin assessment in order to properly detect residual tumor tissue in the surgical cavity.

Traditional localization of the tumor during surgery is achieved by using mammography to implant a small wire next to the tumor region. However, as stated previously, relying on this method alone results in a high rate of positive margins [2]. Therefore several other techniques are currently in practice to improve intraoperative localization and reduce positive margin occurrence. Common methods for this purpose are ultrasound, radio frequency, and cryoprobe localizations [2], [14]. Ultrasound, when used intraoperatively, allows for better real-time localization of the tumor. Furthermore, both ultrasound and radio frequency techniques have been explored for margin assessment of the tissue after it has been excised. However, ultrasound is unable to detect non-palpable tumor regions or ductal carcinoma in situ, and radio frequency assessment has not been shown to reliably improve positive margin rates. Radio frequency

techniques also lack the depth resolution needed to assess close tumor margins [2], [14]. Cryoprobe localization makes use of ultrasound in order to locate and freeze tumors for excision with minimal cosmetic effect, but this technique is limited to smaller tumors and has little improvement in positive margin occurrence after surgery [2].

In addition to attempts at better localization of breast cancer tumor, several techniques have been developed in order to attempt rapid margin assessment during the surgery. The aforementioned ultrasound and radio frequency assessment of excised tissue apply in this category of techniques as well. Another technique currently in use for this application is specimen radiology, which applies mammography to the excised bulk tissue to assess the margins. However, as with other non-contact margin assessment techniques, the specimen radiology lacks the accuracy needed to be reliable on its own [2]. The use of specimen radiology intraoperatively also requires the availability of a radiologist at the time of surgery and may not be feasible for many scenarios. There are also techniques that make use of standard pathology processes intraoperatively in the form of touch prep cytology and the aforementioned frozen section analysis [2], [15]. Touch prep cytology uses a single layer of cells from the outside of the margin for pathology assessment, but lacks the depth analysis necessary to detect close margins. Meanwhile, frozen section analysis is a relatively cheap procedure, but it requires the presence of a pathologist and can still take up to a half hour following the excision to provide results. Frozen sectioning is also limited in the amount of tissue that can be assessed due to the relatively small 4-5 μm thick sections required for pathology, and the freezing process has the potential to damage the tissue before standard pathology can be performed [2]. Therefore, while many techniques for improving the margin assessment during breast conserving surgery are being employed, there is still need for faster, more reliable, and non-destructive methods.

Beyond margin detection, there are already techniques in use for dealing with positive margins discovered intraoperatively. Cavity shaving, radiofrequency ablation, and local radiation therapy are all methods currently used for this purpose [16], [17]. These techniques have already been shown to reduce the incidence of positive margins when used as standalone methods. However, better localization and intraoperative margin assessment would allow for much more precise application of these techniques. This would improve the reliability of these techniques by reducing the cosmetic effects of the procedure and by decreasing the occurrence of positive margins following the lumpectomy surgery.

Breast cancer margin assessment remains an area of importance for improving lumpectomy procedures and thereby improving the treatment of breast cancer. While the aforementioned methods are already used in conjunction with standard pathology to reduce the rate of positive margins in lumpectomies, there is still a need for more reliable techniques for rapid assessment. The objective of this work was to begin to develop the methodologies that can be employed for the use of terahertz for this margin assessment.

B. Introduction to Terahertz for Biomedical Applications

Terahertz (THz) technology has recently become a field of great interest in electromagnetic and optical research. Traditionally this frequency range from 0.1 to 10 THz has been largely inaccessible for practical use. The resulting THz frequency ‘gap’ exists primarily due to said frequencies lying between the ranges attainable by microwave technology and optical techniques in the far infrared region. Since THz frequencies are outside of each technology’s range, there has historically been a lack of reliable sources capable of producing and receiving THz signals using conventional methods [18]. For this reason it was not until recently that reliable THz sources could be used for research applications on a wider scale. With the

development of better THz sources and detectors, this field is currently of great interest for a wide range of research with the goal of determining the potential applications of this technology. Such research areas include material characterization [18], the assessment of material processing techniques through defect detection [19], and security applications via explosive detection and identification [20].

One of the primary research areas for the use of THz frequencies is in biomedical applications. With respect to other biomedical technologies, the use of THz can be categorized as a high frequency electromagnetic technique alongside optical techniques in the infrared frequencies. Optical frequencies have already shown potential for margin assessment using fluorescence imaging and chemical indicators [14], [21]-[26]. However, it has experimentally been shown in [27] that THz waves provided a significant enhancement in transmission imaging contrast in biological material compared to near-infrared techniques. This effect can be explained as the difference between the tissue interactions with the longer THz wavelengths compared to NIR and optical radiation. The scattering in the tissue is a combined effect of the tissue's refractive index, extracellular constituents, and mammalian cells. The photons of an electromagnetic wave are scattered most strongly by objects with sizes comparable to the incident wavelength. Cellular components of tissue tend to be closer to infrared and optical wavelengths, resulting in stronger scattering of optical signals and weaker scattering in the longer wavelengths of terahertz radiation. Due to the weaker Rayleigh scattering of the THz signal, its transmission through biological tissue can be assumed to be dominated by absorption. On the other hand, optical signals are subject to a much stronger Mie scattering, and transmission through biological tissue is not as reasonable [28]. Thus THz frequencies, while similar to other

high frequency techniques in the infrared range, can be used to obtain information at greater depths than optical techniques [27], [28].

The decreased scattering of THz radiation in biological applications compared to optical techniques is one of many reasons that it has become an attractive frequency range for biomedical imaging and characterization [29]. In comparison to lower frequencies used in microwave imaging technologies, THz radiation is able to provide a higher feature resolution when imaging due to its smaller wavelength [30]. Additionally, THz sources at present tend to have low output power, and the radiation is non-ionizing. Thus THz radiation is unlikely to cause damage to biological tissue or to change its properties, which would interfere with other processing or imaging techniques. This makes THz applications ideal for use in conjunction with standard techniques like the histopathology assessment used in breast cancer surgery [30], [31]. Finally, THz radiation is sensitive to water content due to strong absorption peaks of liquid water in the THz frequency range. Thus it is useful for biological applications where the water content of tissues is a distinguishing factor [30], [32].

THz frequency techniques have already been applied to a wide range of biomedical applications, with particular interest in cancer applications [33]. Some non-cancer research areas for which THz has shown promising results include differentiation between normal cardiac tissue and regions damaged by myocardial infarction [34], assessment of the severity and depth of burns on skin [35], imaging of cirrhosis of the liver [36], imaging and thickness measurements of tooth enamel [37], general characterization of many body tissue constituents and organs [38], [39], and assessment of thin histopathology samples [40]. For cancer applications, some of the earliest characterization and imaging was performed on basal cell carcinoma due to its ability to be researched without surgical techniques to access or obtain the tissue [41]. Subsequent research

has explored the potential for THz analysis of lung cancer [42], freshly excised and fixed colorectal cancer [43], [44], and oral cancer [45]. However, the primary focus of this work is the application of THz technology to breast cancer applications.

Recent publications in literature have reported several studies started in the UK of experimental imaging and characterization of freshly excised breast cancer specimens [46]-[48]. Fitzgerald *et al*. reported in [46] the reflection mode imaging of tissues excised from 22 breast cancer patients through wide local excision or mastectomy. Subsequent imaging was performed by measuring the maximum and minimum values of the reflected electric field at each point in the imaging scan [46]. The reported results showed the potential for THz waves to distinguish cancerous and non-cancerous tissue from excised breast tumors using a pulsed THz signal with frequency components up to 2 THz. Further work was reported by Ashworth *et al*. in [47], where characterization of freshly excised tissue was obtained within the same frequency range. The reported electrical properties of the cancer, fibroglandular, and fatty tissue showed clear distinctions in the different tissue regions across the THz frequency range. These results give further credibility to the use of THz analysis of breast cancer tissue for characterization and imaging. Previous work in this group used simulation and preliminary experimental results for breast cancer imaging, which was presented in various conferences [49]-[51], and previous experimental work with electronics has shown the potential for THz imaging of three-dimensional objects [52]. This thesis presents experimental work in the use of THz spectroscopy and imaging on breast cancer tissue at the University of Arkansas, and portions of the work have been presented in several conferences [53]-[57].

C. Breast Cancer Sample Data

The samples that were analyzed throughout this research were obtained from the Cooperative Human Tissue Network (CHTN) division at the University of Alabama at Birmingham. It should be noted that three tissue sets were obtained from CHTN, but that in many cases there was trouble in proper tissue adhesion to the glass slides or in the cancer content of the tissue. Thus for this work only the set of tissue with good adhesion and cancer presence was addressed. Additional tissue has since been obtained from the National Disease Research Interchange (NDRI), but those samples were not addressed in this work and are currently part of ongoing research. Samples of formalin-fixed, paraffin-embedded (FFPE) tissue on glass slides were obtained from three different women with the request that the tissue obtained from each sample contained both tumor tissue and normal tissue adjacent to one another. In addition to the FFPE slides, some slides were processed using standard pathology staining with hematoxylin and eosin (H&E) in order to provide a method for pathology analysis of the samples. Each sample was also accompanied by a surgical pathology report designating the type of cancer and other relevant details. The pathology assessment for each H&E slide was provided by Dr. Shree Sharma, Assistant Professor of Pathology at the University of Arkansas for Medical Sciences in Little Rock, AR.

Twelve slides were obtained from each of the three samples. The distribution of the slides from each sample was as follows:

- One 5 μm thick section with H&E staining and cover slip (slide #1), which was delivered to CHTN for analysis.
- One 10 μm thick section with H&E staining and cover slip (slide #2), used for pathology assessment in this work.

- Ten 10 μm thick sections left as FFPE tissue (slides #3-#12).

Additionally, slide #12 from each set was used in an attempt to study the effects of paraffin removal on the imaging of the tissue. It was found that removal of paraffin decreased the thickness of the tissue to the extent that imaging was no longer possible, thus excluding the slide from additional work in this research. Therefore the available tissue for this research from each of the three samples included the 20 μm H&E stained slide (#2) and nine usable 20 μm thick sections of FFPE tissue (#3-#11). The H&E pathology assessment performed on slide #2 of each sample set included low power (low magnification) microscopy images of the slides. These images were subsequently stitched together using the open source panorama editor HugIn [58]. The particular details of each of the samples will be addressed in the following sections.

Sample 1: Tissue Obtained from 40 Year Old Patient

The first sample was obtained from a 40 year old Caucasian woman following a radical mastectomy. The primary diagnosis of the tissue was grade III/III triple negative infiltrating ductal carcinoma (IDC). However, it was also noted in the pathology report that the cancer was

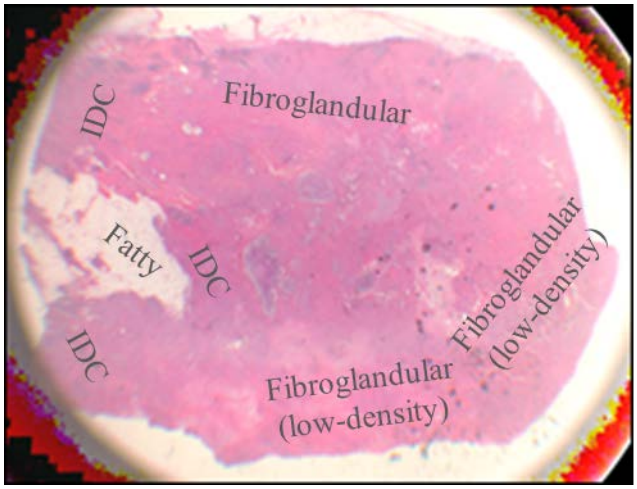

Figure 1.1: Low power pathology image of sample from 40 year old Caucasian woman diagnosed with poorly-differentiated infiltrating ductal carcinoma (IDC). Regions of fibroglandular, fatty, and low-density fiboglandular tissue are also denoted.

poorly differentiated. This indicates that the regions of cancer present in the tumor were not characteristic of the typical tissue of this area and were heavily mingled with the surrounding tissue, making clearly defined regions difficult to determine. The pathology assessment of this sample was able to denote regions of IDC, fibroglandular, and fatty tissue present on the H&E slide. There were also regions denoted as low-density fibroglandular tissue, which is fibroglandular tissue with a somewhat higher percentage of fat. The stitched pathology image obtained from this sample is given in Fig. 1.1.

Sample 2: Tissue Obtained from 46 Year Old Patient

The second sample was obtained from a 46 year old Caucasian woman following mastectomy. The primary diagnosis of the tissue was grade III/III triple negative infiltrating ductal carcinoma. The pathology assessment of this sample was able to denote regions of IDC and fibroglandular tissue along with a smaller region of fatty tissue. The stitched low power pathology imaging of slide #2 obtained from this sample is given in Fig. 1.2.

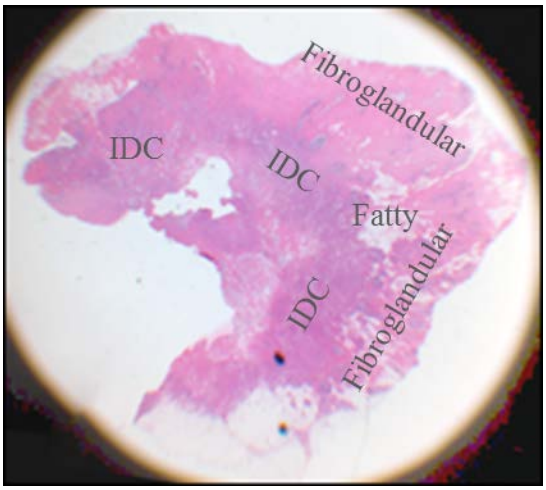

Figure 1.2: Low power pathology image of sample from 46 year old Caucasian woman diagnosed with infiltrating ductal carcinoma (IDC). Regions of fibroglandular and fatty tissue are also denoted.

Sample 3: Tissue Obtained from 22 Year Old Patient

The third sample used in this research was obtained from a 22 year old Caucasian woman who underwent a lumpectomy procedure and subsequent breast conservation surgery. The age of this patient is exceptionally young for having undergone a lumpectomy, and many techniques report troubles with the assessment of cancer in younger patients. The primary diagnosis was grade II/III triple negative infiltrating ductal carcinoma as well as ductal carcinoma in situ (DCIS). The pathology assessment of this tissue denoted regions of IDC, fibroglandular, and DCIS, corroborating with the surgical pathology report. The stitched low power pathology imaging of slide #2 obtained from this sample is given in Fig. 1.3.

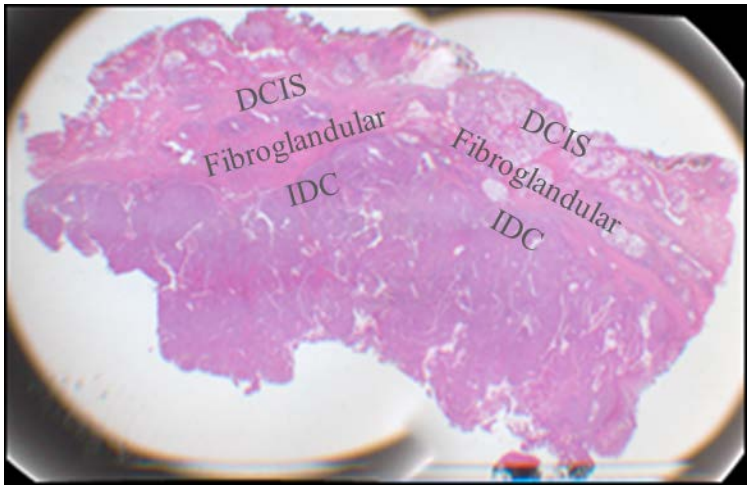

Figure 1.3: Low power pathology image of sample from 22 year old Caucasian woman diagnosed with infiltrating ductal carcinoma (IDC). Regions of fibroglandular tissue and ductal carcinoma in situ (DCIS) are also denoted.

D. Pulsed Terahertz Imaging and Spectroscopy System (TPS Spectra 3000)

Basic System Information

The system that was used for this research was the TPS Spectra 3000, a commercial pulsed terahertz system that was purchased from TeraVIEW, Ltd., UK [59]. A basic diagram of the signal path of the system is outlined in Fig. 1.4. This system produces a time domain THz

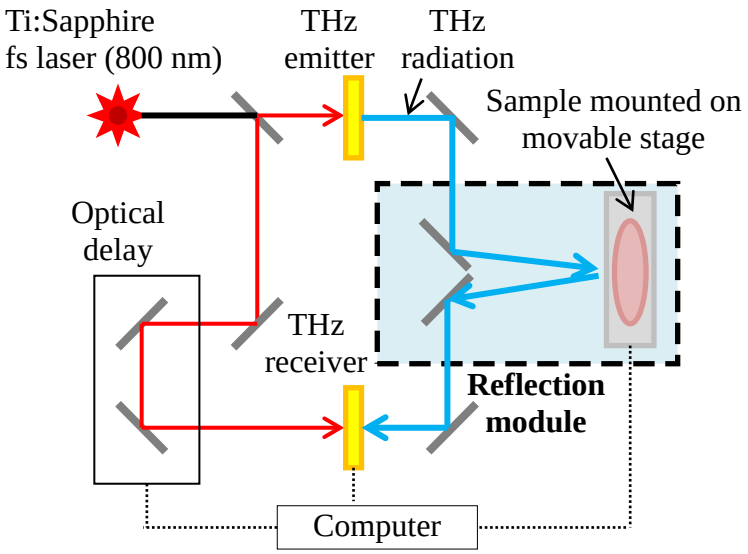

Figure 1.4. Diagram of TPS Spectra 3000 signal generation for reflection imaging mode.

signal by first exciting a biased GaAs antenna using a series of 800 nm Ti:Sapphire laser pulses. The antenna then produces a time domain THz pulse with an approximate width of 500 fs. The generated signal passes through the sample space, in which the system components and sample under test are placed, and returns to the receiver. The THz receiver in this system is another GaAs antenna that is excited by a split from the same laser pulse. In the case of Fig. 1.4 the reflection imaging module path and sample orientation is shown, but there are various modules that can be installed in the system for different applications that will be addressed in the next section. The generated voltage across the receiver antenna is recorded as the measured signal along with the optical delay in order to obtain the time domain signal measurement. Use of Fourier transform on the measured time domain pulse provides a spectrum of complex frequency domain values ranging from approximately 100 GHz to 4 THz. The comparison of the time domain and frequency domain signals obtained from transmission spectroscopy of the system with an empty sample space can be seen in Figure 1.5. The time domain signal in Fig. 1.5(a) is the impulse measured by the system, and the frequency domain signal in Fig. 1.5(b) is expressed

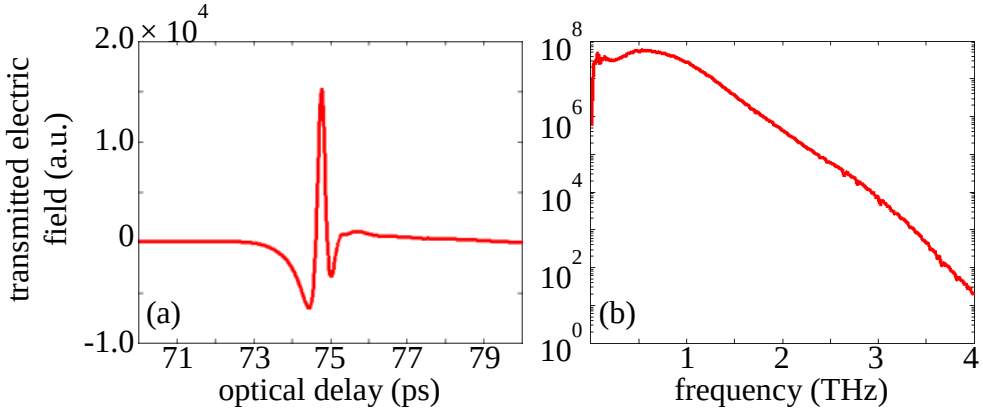

Figure 1.5. (a) Time domain and (b) frequency domain signals transmitted through empty sample space following nitrogen purge.

as the magnitude of the signal at each frequency following the Fourier transform used by the THz system. Ideally any application of the project using this source would be able to provide frequency domain analysis across the entire range illustrated in Fig. 1.5(b).

System Modules

Six modules for spectroscopy and imaging are included in the THz system at the University of Arkansas:

(1) the standard spectroscopy module,

(2) heated cell spectroscopy,

(3) cryostat spectroscopy,

(4) reflection imaging module,

(5) transmission imaging module, and

(6) gantry system.

For general room temperature spectroscopy, the standard spectroscopy module shown in Fig. 1.6 is used. The time domain signal is transmitted through the window of the module at incidence normal to the sample surface and measured on the other side. Generally the sample under test is placed in a specialized sample holder or on a windowed aperture in order to mount

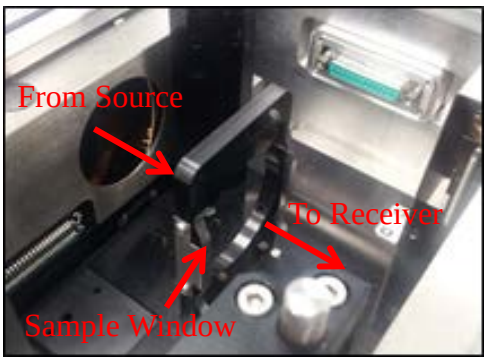

Figure 1.6. Standard spectroscopy module inside system chamber.

the object in the center of the beam. There is also an additional sample holder specifically for liquid samples. For spectroscopy over a range of temperatures, the heated cell or cryostat spectroscopy modules are used. These two modules are shown in Fig. 1.7. The heated cell in Fig. 1.7(a) uses an external temperature controller in order to heat the system up to 573 K, and a thermal probe provides the temperature for measurement correlation. The cryostat module in Fig. 1.7(b) makes use of a double-vacuum cell with liquid helium cooling with a minimum temperature of 3.4 K. Within the scope of this research, only the room temperature spectroscopy of the samples was required, so the standard spectroscopy module was used.

The two imaging modules of the system are shown in Fig. 1.8. For both imaging modules

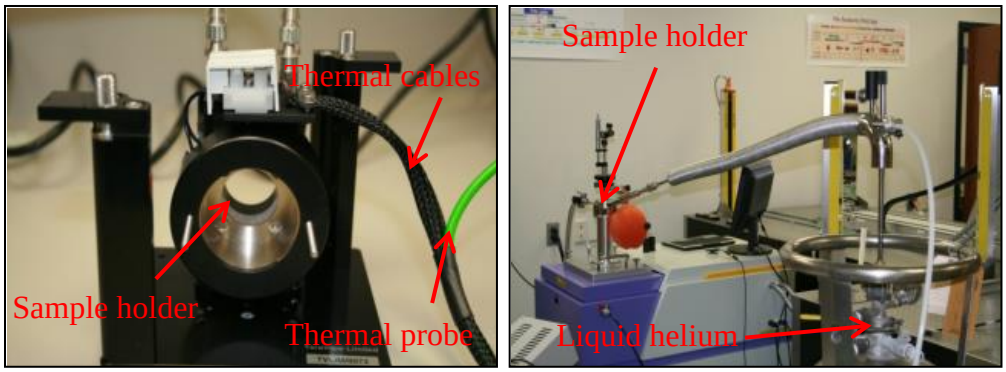

(a) (b)

Figure 1.7. Modules for temperature-dependent spectroscopy.
(a) Heated cell up to 573 K and (b) cryostat system down to 4 K.

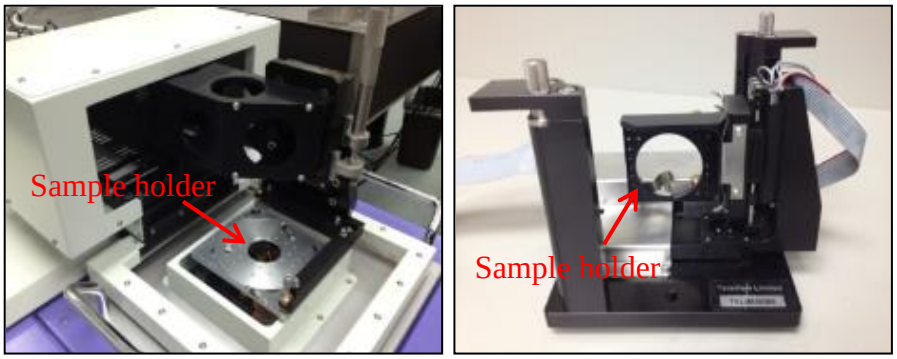

(a) (b)

Figure 1.8. Terahertz system imaging modules for (a) reflection and (b) transmission modes.

the sample window is controlled via micromotors to perform a raster scan with an adjustable step size as small as 50 μm. The sample window of both imaging modules has a diameter of 3.5 cm. However the space limitations of the sample chamber limit the motor range of the transmission imaging module to an effective scan area of 1.9 cm × 1.9 cm. Unlike the transmission imaging module, the reflection imaging module (RIM) sits above the sample chamber of the system and can fully image the entire sample holder window. A mirror base directs the signal upward to reflect on the sample from below. In order to accommodate for both the incident and reflected signal paths, the signal is directed to reflect from the sample at an angle 30° from normal.

The final module of the system is the gantry setup shown in Fig. 1.9. This accessory system receives a laser signal from the main THz system that excites a separate pair of emitter

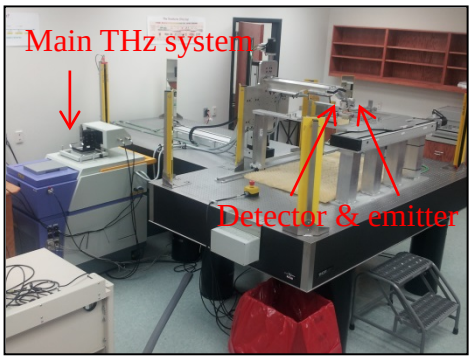

Figure 1.9. Gantry system for imaging of samples up to 70 cm × 70 cm.

and receiver antennas. The sample holder and antenna setup are both motorized, allowing for scan areas as large as 70 cm × 70 cm. Additionally the positioning of the arms holding the antennas can be adjusted to permit either reflection or transmission imaging of the large scale samples. For this work the samples were small enough to use on the core system modules, so the gantry was not used. Additionally it was found that the glass slides on which the samples were mounted significantly attenuated the transmission signal that passed through it. This combined with the relatively small thickness of the tissue on the glass slide resulted in a complete loss of contrast in transmission imaging. Thus only the reflection imaging module was utilized within the scope of this research so far. Ongoing research is investigating the use of thicker tissue up to 40 μm on less absorptive slide materials and should permit for future transmission imaging. However that is outside of the scope of what was possible for the work presented here.

E. Overview of Thesis Chapters

This first chapter has been used in order to provide the background and motivation of the work in this thesis, as well as to provide basic information on the tissue samples and the pulsed THz system used in the experimental work. Chapter II will show the results of THz imaging of the samples as well as the correlation with spectroscopy results via reflection characterization. Chapter III will present the calculations and experimental results for the THz spectroscopy of the tissue samples on glass. Chapter IV will correlate the results of both spectroscopy and imaging and discuss future work. A flowchart of the thesis layout is shown in Fig. 1.10.

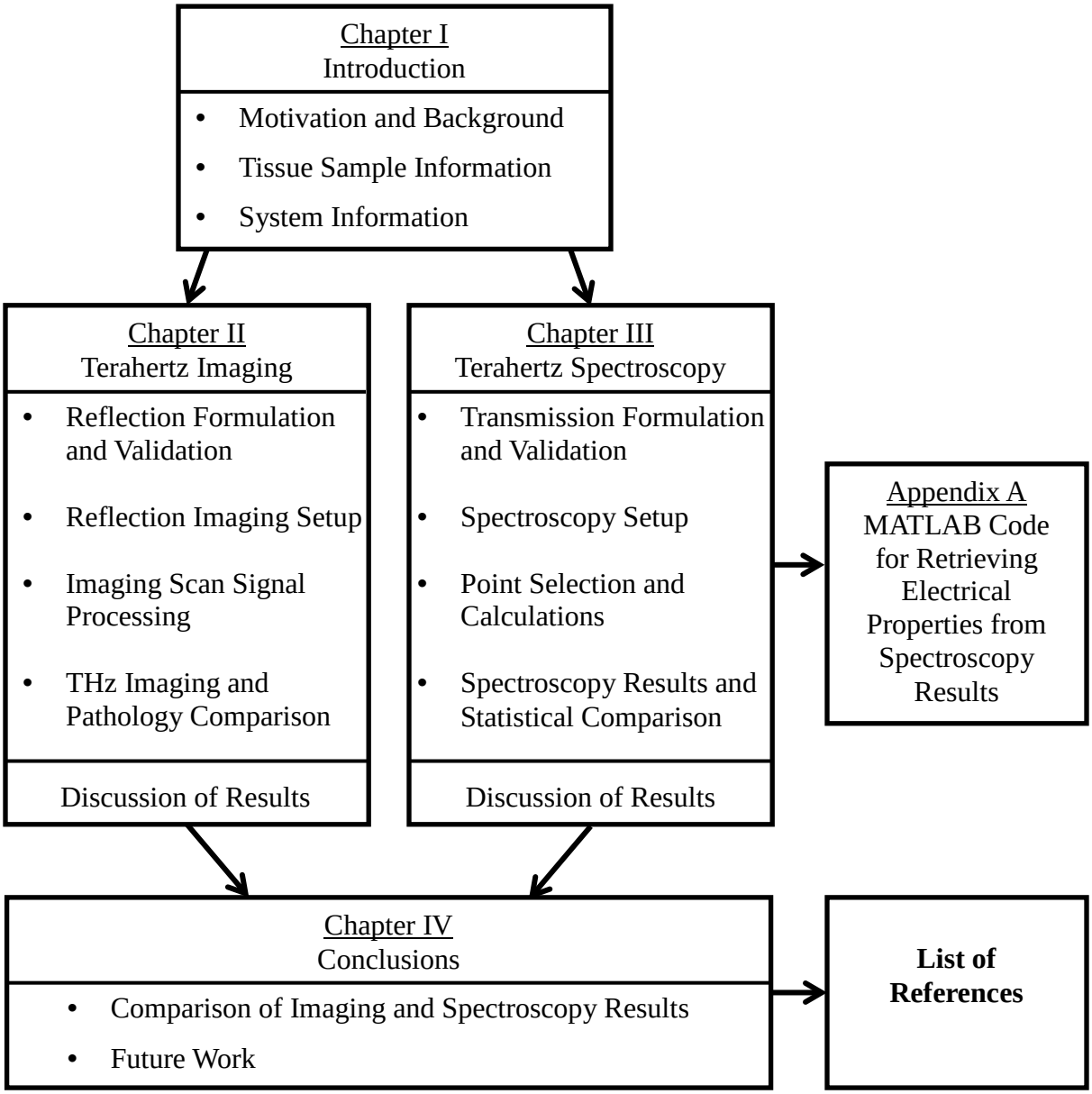

Figure 1.10. Flowchart of Master's Thesis chapters

II. Terahertz Imaging of Ex-vivo Breast Cancer Tissue

A. Reflection Formulation in TE/TM Polarization

An important step in making use of the reflection imaging of the THz system was to be able to express the signal obtained from the reflection analytically in terms of the dielectric properties of each region in the sample under test. Having a theoretical representation of this signal made it possible to compare the measured reflected signals with the expected reflection using the retrieved properties of the sample obtained from transmission spectroscopy. In the case of the reflection imaging, the value of the reflected signal from the sample with respect to the incident signal or some reference needed to be found.

The expression of this reflected signal will vary depending on the angle of incidence as well as the polarization of the incident E-field with respect to the plane of incidence. There are two potential orientations of this polarization as shown in Fig. 2.1. In this diagram, the electric field in each region is denoted as $\overline{E}$ and the magnetic field is denoted as $\overline{H}$. $\overline{k}$ is a complex vector denoting the propagation of the signal. Superscript + indicates the components of the field for

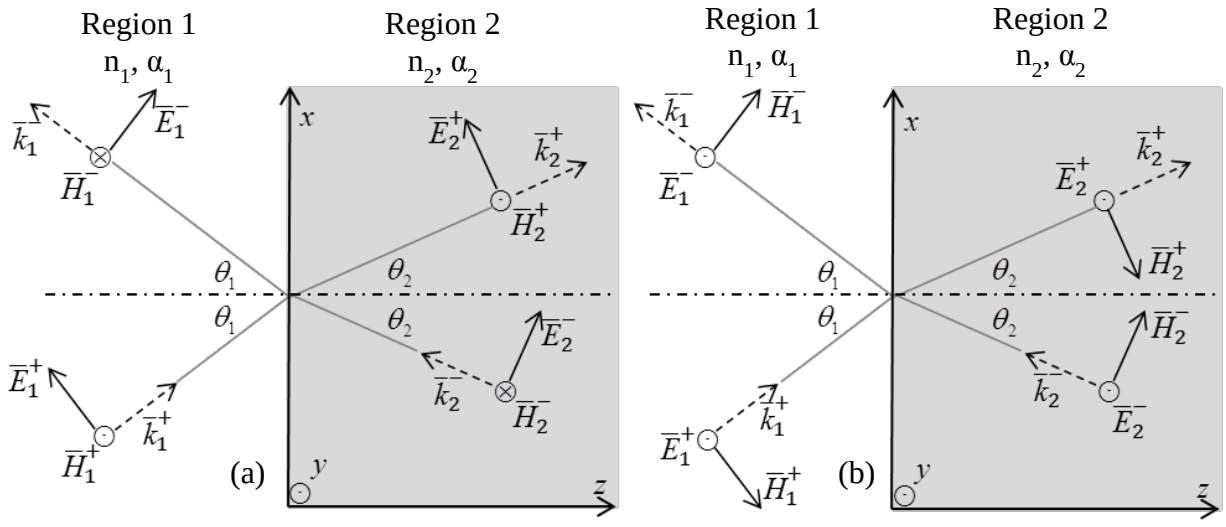

Figure 2.1. Signal interaction at boundary of two media for (a) transverse magnetic (TM), parallel, or p-polarization and (b) transverse electric (TE), perpendicular, or s-polarization.

which the propagation direction contains a positive *z*-component, and – indicates that the propagation contains a negative *z*-component. Finally the subscript denotes the region in which each term lies. The first orientation of the fields, as shown in Fig. 2.1(a), is denoted as transverse magnetic (TM) polarization since the magnetic field is transverse to the *z*-axis. This is also denoted as parallel polarization since the electric field is parallel to the plane of incidence (*x*-*z* plane) or as p-polarization. The second orientation shown in Fig. 2.1(b) is denoted as transverse electric (TE) polarization since the electric field is now transverse to the *z*-axis. It is also denoted as perpendicular polarization, since the electric field is perpendicular to the plane of incidence, or as s-polarization [60]. The signal of the reflection imaging module is believed to be TE mode, but the complex mirror arrangement that directs the incident signal made it difficult to confirm. Thus the full solution for both polarizations was calculated and compared in this work.

The solution presented here was primarily obtained following the steps provided in references [60] and [61]. Before the equations of the sample under test in the reflection imaging were calculated, the equations for a single interface given in Fig. 2.1 had to be found. The relationship between the angles of the propagation in the two regions is given by the well-known equation of Snell's Law.

$$\tilde{n}_1 \sin\theta_1 = \tilde{n}_2 \sin\theta_2 \tag{2-1}$$

Where $\tilde{n}_1$ and $\tilde{n}_2$ denote the complex refractive index of the left and right sides of the interface in Fig. 2.1, respectively, and θ_1 and θ_2 are the angles of propagation with respect to the z-direction on each side. The solution at the interface seeks to satisfy the boundary conditions when there is no current present:

$$E_{t1} - E_{t2} = 0\,, \quad E_{t1} = E_{t2} \tag{2-2}$$

$$\hat{n} \times (H_1 - H_2) = 0\,, \quad H_{t1} = H_{t2} \tag{2-3}$$

Where $\hat{n}$ is the unit vector normal to the boundary plane (in this case corresponding to the *z*-direction), and E_t and H_t are the electric and magnetic fields tangential to the boundary. The field components in each region are then given by the following equations:

$$\overline{E}_1(\bar{r}) = \overline{E}_1^+ e^{-\gamma_1 \cdot \bar{r}} + \overline{E}_1^- e^{\gamma_1 \cdot \bar{r}} \tag{2-4}$$

$$\overline{H}_1(\bar{r}) = \frac{\overline{E}_1^+}{\tilde{\eta}_1} e^{-\gamma_1 \cdot \bar{r}} - \frac{\overline{E}_1^-}{\tilde{\eta}_1} e^{\gamma_1 \cdot \bar{r}} \tag{2-5}$$

$$\overline{E}_2(\bar{r}) = \overline{E}_2^+ e^{-\gamma_2 \cdot \bar{r}} + \overline{E}_2^- e^{\gamma_2 \cdot \bar{r}} \tag{2-6}$$

$$\overline{H}_2(\bar{r}) = \frac{\overline{E}_2^+}{\tilde{\eta}_2} e^{-\gamma_2 \cdot \bar{r}} - \frac{\overline{E}_2^-}{\tilde{\eta}_2} e^{\gamma_2 \cdot \bar{r}} \tag{2-7}$$

Where γ is the complex propagation constant, $\tilde{\eta}$ is the intrinsic impedance in each region, and $\bar{r}$ is the Cartesian distance vector defined as:

$$\gamma = j\omega\sqrt{\mu\tilde{\varepsilon}} = j\omega\sqrt{\mu\left(\varepsilon - j\frac{\sigma}{\omega}\right)} \tag{2-8}$$

$$\tilde{\eta} = \sqrt{\frac{\mu}{\tilde{\varepsilon}}} = \sqrt{\frac{\mu}{\left(\varepsilon - j\frac{\sigma}{\omega}\right)}} \tag{2-9}$$

$$\bar{r} = x\hat{x} + y\hat{y} + z\hat{z} \tag{2-10}$$

Where $\tilde{\varepsilon}$ is the complex permittivity, μ is the permeability, σ is the conductivity, and ω is the angular frequency. The values in equations (2-8) and (2-9) can then be expressed in terms of the complex refractive index $\tilde{n}$ using the definition $\tilde{n} = \sqrt{\tilde{\varepsilon}_r} = n - j\kappa$ and assuming a region of non-magnetic material where $\mu = \mu_0$.

$$\tilde{\varepsilon} = \tilde{\varepsilon}_r \varepsilon_0 , \quad c = \frac{1}{\sqrt{\mu_0 \varepsilon_0}} , \quad \eta_0 = \sqrt{\frac{\mu_0}{\varepsilon_0}} \tag{2-11}$$

$$\gamma = j\omega\sqrt{\mu_0 \varepsilon_0 \tilde{\varepsilon}_r} = j\frac{\omega}{c}\tilde{n} \tag{2-12}$$

$$\tilde{\eta} = \sqrt{\frac{\mu_0}{\varepsilon_0 \tilde{\varepsilon}_r}} = \frac{\eta_0}{\tilde{n}} \tag{2-13}$$

Where $c = 3\times10^8 \text{m/s}$ is the speed of light in a vacuum and $\eta_0 = 120\pi\ \Omega$ is the total field impedance in a vacuum. Finally, using the definition of the complex refractive index and the alternate definition of the propagation constant:

$$\gamma = \alpha + j\beta \text{ cm}^{-1} = j\frac{\omega}{c}\tilde{n} = j\frac{\omega}{c}n + \frac{\omega}{c}\kappa \tag{2-14}$$

$$n = \frac{c}{\omega}\beta , \quad \kappa = \frac{c}{\omega}\alpha \tag{2-15}$$

Where α is the attenuation constant and β is the phase constant of the signal as it propagates. For the sake of later comparison, γ will be expressed in terms of refractive index n and the absorption coefficient α_{abs}. These particular two values are chosen to represent the dielectric properties in this research due to being the primary values that the THz system's spectroscopy calculates. The absorption coefficient is defined as the exponential decay of the power of the wave, which can be found using the Poynting vector.

$$\overline{P}(z) = \overline{E} \times \overline{H}^* = E_x^+ e^{-\gamma z}\hat{a}_x \times \left(H_y^+ e^{-\gamma z}\right)^* \hat{a}_y = \left(E_x^+ e^{-(\alpha + j\beta)z}\right)\left(\frac{E_x^{+*}}{\tilde{\eta}^*} e^{-(\alpha - j\beta)z}\right)\hat{a}_z \tag{2-16}$$

$$\overline{P}(z) = \frac{\left|E_x^+\right|^2}{\tilde{\eta}^*} e^{-2\alpha z}\hat{a}_z = \frac{\left|E_x^+\right|^2}{\tilde{\eta}^*} e^{-\alpha_{abs} z}\hat{a}_z \tag{2-17}$$

$$\alpha_{abs} = 2\alpha \tag{2-18}$$

This was solved for an arbitrary case in which the electric field was exclusively in the *x* direction and the magnetic field was exclusively in the *y* direction, but the result is the same for any orientation of the wave. Thus the final expression for γ in terms of refractive index and absorption coefficient is given as:

$$\gamma = \frac{\alpha_{abs}}{2} + j\frac{\omega}{c} n \text{ cm}^{-1} \tag{2-19}$$

For the sake of the calculations of the TE and TM modes, the propagation constant will be expressed in a different means using the complex constant $\tilde{k}$ which can be broken down into *x* and *z* components for each signal present in Fig. 2.1 [60]:

$$\gamma = j\tilde{k} = j\frac{\omega}{c}\tilde{n} \tag{2-20}$$

$$\begin{aligned} \bar{k}_1^+ &= \tilde{k}_1 \sin\theta_1 \hat{x} + \tilde{k}_1 \cos\theta_1 \hat{z}, \quad \bar{k}_1^- = \tilde{k}_1 \sin\theta_1 \hat{x} - \tilde{k}_1 \cos\theta_1 \hat{z} \\ \bar{k}_2^+ &= \tilde{k}_2 \sin\theta_2 \hat{x} + \tilde{k}_2 \cos\theta_2 \hat{z}, \quad \bar{k}_2^- = \tilde{k}_2 \sin\theta_2 \hat{x} - \tilde{k}_2 \cos\theta_2 \hat{z} \end{aligned} \tag{2-21}$$

Where $\bar{k}_1^+$, $\bar{k}_1^-$, $\bar{k}_2^+$, and $\bar{k}_2^-$ are the propagation vectors in each region of Fig. 2.1, and $\tilde{k}_1$ and $\tilde{k}_2$ in these equations are different expressions of the complex propagation coefficient in each region. Finally, the relation of the propagation coefficient to the distance travelled is defined by using the dot product of the propagation vector with the Cartesian distance vector $\bar{r}$. Below is an example of the exponential expression for the propagation using the propagation vector $\bar{k}_1^+$.

$$e^{-j\bar{k}_1^+ \bullet \bar{r}} \Rightarrow e^{-j\tilde{k}_1(\sin\theta_1 x + \cos\theta_1 z)} \tag{2-22}$$

TM Polarization

In addition to the propagation vector, for TM polarization the electric field in Fig. 2.1a can also be separated into terms in the *x* and *z* directions based on the angle of propagation.

$$\overline{E}_1^+(x,z) = \left(\cos\theta_1 \hat{x} - \sin\theta_1 \hat{z}\right) E_{m1}^+ e^{-j\tilde{k}_1(\sin\theta_1 x + \cos\theta_1 z)} \tag{2-23}$$

$$\overline{E}_1^-(x,z) = \left(\cos\theta_1 \hat{x} + \sin\theta_1 \hat{z}\right) E_{m1}^- e^{-j\tilde{k}_1(\sin\theta_1 x - \cos\theta_1 z)} \tag{2-24}$$

Where E_{m1}^+ and E_{m1}^- denote the magnitude of the electric field in region 1 corresponding to the signals with positive and negative propagation with respect to *z*, respectively. The magnetic field component instead lies exclusively in the *y* direction.

$$\overline{H}_1^+(x,z) = \hat{y}\frac{E_{m1}^+}{\tilde{\eta}_1} e^{-j\tilde{k}_1(\sin\theta_1 x + \cos\theta_1 z)} \tag{2-25}$$

$$\overline{H}_1^-(x,z) = -\hat{y}\frac{E_{m1}^-}{\tilde{\eta}_1} e^{-j\tilde{k}_1(\sin\theta_1 x - \cos\theta_1 z)} \tag{2-26}$$

Since the reflection coefficients are found by solving for the fields at the boundary and only fields tangential to the boundary are included in the boundary conditions, the total electric field in the *x* direction is considered.

$$E_{x1}(x,z) = \cos\theta_1 \hat{x}\left(E_{m1}^+ e^{-j\tilde{k}_1\cos\theta_1 z} + E_{m1}^- e^{j\tilde{k}_1\cos\theta_1 z}\right) e^{-j\tilde{k}_1\sin\theta_1 x} \tag{2-27}$$

$$E_{x1}(x,z) = \hat{x}\cos\theta_1 E_{m1}^+ e^{-j\tilde{k}_1\cos\theta_1 z}\left(1 + \tilde{\Gamma}_{TM,1}(z)\right) e^{-j\tilde{k}_1\sin\theta_1 x} \tag{2-28}$$

$$\tilde{\Gamma}_{TM,1}(z) = \frac{E_{m1}^-}{E_{m1}^+} e^{j2\tilde{k}_1\cos\theta_1 z} \tag{2-29}$$

Where E_{x1} denotes the total electric field in the *x* direction for region 1. The boundary conditions in equations (2-2) and (2-3) state that the fields tangential to the interface in both regions are the same at the boundary. Thus the ratio of the electric to magnetic field is also continuous at the boundary. Additionally the propagation in the *x* direction on either side of the interface represented by $-j\tilde{k}_i \sin\theta_i x$ will always be equal due to Snell's Law in equation (2-1). Thus the term cancels out when comparing at the interface.

$$H_{y1}(z)=\frac{1}{\tilde{\eta}_1}\hat{y}\left(E_{m1}^{+}e^{-j\tilde{k}_1\cos\theta_1 z}-E_{m1}^{-}e^{j\tilde{k}_1\cos\theta_1 z}\right)e^{-j\tilde{k}_1\sin\theta_1 x}=\hat{y}\frac{E_{m1}^{+}}{\tilde{\eta}_1}e^{-j\tilde{k}_1\cos\theta_1 z}\left(1-\tilde{\Gamma}_{TM,1}(z)\right)e^{-j\tilde{k}_1\sin\theta_1 x} \quad (2\text{-}30)$$

$$\tilde{Z}_{TM,1}(z)=\frac{E_{x1}(z)}{H_{y1}(z)}=\tilde{\eta}_1\cos\theta\frac{1+\tilde{\Gamma}_{TM,1}(z)}{1-\tilde{\Gamma}_{TM,1}(z)} \quad (2\text{-}31)$$

$$\tilde{\Gamma}_{TM,1}(z)=\frac{\tilde{Z}_{TM,1}(z)-\tilde{\eta}_1\cos\theta_1}{\tilde{Z}_{TM,1}(z)+\tilde{\eta}_1\cos\theta_1} \quad (2\text{-}32)$$

If one assumes that the diagram in Fig. 2.1(a) indicates two infinite regions and that there is no reflected wave in the second medium then the reflection coefficient at the interface $z=0$ can be found.

$$\tilde{Z}_{TM,2}(0)=\tilde{\eta}_2\cos\theta_2=\tilde{Z}_{TM,1}(0) \quad (2\text{-}33)$$

$$\tilde{\Gamma}_{TM,1}(0)=\frac{\tilde{\eta}_2\cos\theta_2-\tilde{\eta}_1\cos\theta_1}{\tilde{\eta}_2\cos\theta_2+\tilde{\eta}_1\cos\theta_1}=\frac{\tilde{n}_1\cos\theta_2-\tilde{n}_2\cos\theta_1}{\tilde{n}_1\cos\theta_2+\tilde{n}_2\cos\theta_1} \quad (2\text{-}34)$$

This equation agrees with the expression of the reflection coefficient for the parallel polarization in [61]. This can be expressed in the same form as the reflection of an interface at normal incidence by a simple substitution.

$$\tilde{n}_{TM,i}=\frac{\tilde{n}_i}{\cos\theta_i},\quad \tilde{\eta}_{TM,i}=\frac{\eta_0}{\tilde{n}_{TM,i}}=\tilde{\eta}_i\cos\theta_i \quad (2\text{-}35)$$

$$\tilde{\Gamma}_{TM,1}(0)=\frac{\tilde{n}_{TM,1}-\tilde{n}_{TM,2}}{\tilde{n}_{TM,1}+\tilde{n}_{TM,2}} \quad (2\text{-}36)$$

Where $\tilde{n}_i$ is the complex refractive index of an arbitrary region *i* expressed as a substitution of (2-20) into (2-19):

$$\tilde{n}_i=n_i-j\frac{c}{2\omega}\alpha_{abs,i} \quad (2\text{-}37)$$

TE Polarization

The solution for the reflection coefficients for the TE (perpendicular) polarization is solved by following the same process as the TM polarization with the consideration of Fig. 2.1(b), where the electric field now lies solely in the *y* direction and the magnetic field is separable into *x* and *z* components.

$$\overline{E}_1^+(x,z) = \hat{y}E_{m1}^+ e^{-j\tilde{k}_1(\sin\theta_1 x + \cos\theta_1 z)} \tag{2-38}$$

$$\overline{E}_1^-(x,z) = \hat{y}E_{m1}^- e^{-j\tilde{k}_1(\sin\theta_1 x - \cos\theta_1 z)} \tag{2-39}$$

$$\overline{H}_1^+(x,z) = \left(-\cos\theta_1\hat{x} + \sin\theta_1\hat{z}\right)\frac{E_{m1}^+}{\tilde{\eta}_1} e^{-j\tilde{k}_1(\sin\theta_1 x + \cos\theta_1 z)} \tag{2-40}$$

$$\overline{H}_1^-(x,z) = \left(\cos\theta_1\hat{x} + \sin\theta_1\hat{z}\right)\frac{E_{m1}^-}{\tilde{\eta}_1} e^{-j\tilde{k}_1(\sin\theta_1 x - \cos\theta_1 z)} \tag{2-41}$$

Once again, only the terms tangential to the boundary surface are considered in boundary conditions. However, it should also be noted that for electric field in the *y* direction and for the component of the propagation normal to the boundary in the *z* direction, the right-hand rule dictates that the magnetic field in the *–x* direction must be considered to avoid a sign error.

$$E_{y1}(x,z) = \hat{y}\left(E_{m1}^+ e^{-j\tilde{k}_1\cos\theta_1 z} + E_{m1}^- e^{j\tilde{k}_1\cos\theta_1 z}\right)e^{-j\tilde{k}_1\sin\theta_1 x} = \hat{y}E_{m1}^+ e^{-j\tilde{k}_1\cos\theta_1 z}\left(1+\tilde{\Gamma}_{TE,1}(z)\right)e^{-j\tilde{k}_1\sin\theta_1 x} \tag{2-42}$$

$$\tilde{\Gamma}_{TE,1}(z) = \frac{E_{m1}^-}{E_{m1}^+} e^{j2\tilde{k}_1\cos\theta_1 z} \tag{2-43}$$

$$H_{-x1}(x,z) = \hat{x}\frac{\cos\theta_1}{\tilde{\eta}_1} E_{m1}^+ e^{-j\tilde{k}_1\cos\theta_1 z}\left(1-\tilde{\Gamma}_{TE,1}(z)\right)e^{-j\tilde{k}_1\sin\theta_1 x} \tag{2-44}$$

$$\tilde{Z}_{TE,1}(z) = \frac{E_{y1}(x,z)}{H_{-x1}(x,z)} = \frac{\tilde{\eta}_1}{\cos\theta_1}\frac{1+\tilde{\Gamma}_{TE,1}(z)}{1-\tilde{\Gamma}_{TE,1}(z)} \tag{2-45}$$

$$\tilde{\Gamma}_{TE,1}(z)=\frac{\tilde{Z}_{TE,1}(z)-\left(\tilde{\eta}_1/\cos\theta_1\right)}{\tilde{Z}_{TE,1}(z)+\left(\tilde{\eta}_1/\cos\theta_1\right)} \tag{2-46}$$

As in the case for TM polarization, the reflection from a single boundary at $z=0$ with no returning signal in the second region can be found [61].

$$\tilde{Z}_{TE,2}(0)=\left(\tilde{\eta}_2/\cos\theta_2\right)=\tilde{Z}_{TE,1}(0) \tag{2-47}$$

$$\tilde{\Gamma}_{TE,1}(0)=\frac{\left(\tilde{\eta}_2/\cos\theta_2\right)-\left(\tilde{\eta}_1/\cos\theta_1\right)}{\left(\tilde{\eta}_2/\cos\theta_2\right)+\left(\tilde{\eta}_1/\cos\theta_1\right)}=\frac{\tilde{n}_1\cos\theta_1-\tilde{n}_2\cos\theta_2}{\tilde{n}_1\cos\theta_1+\tilde{n}_2\cos\theta_2} \tag{2-48}$$

This equation also agrees with the reflection coefficients defined for perpendicular polarization in [61]. Once again a substitution can be used to express the reflection in a format similar to the normal incidence.

$$\tilde{n}_{TE,i}=\tilde{n}_i\cos\theta_i\ ,\quad \tilde{\eta}_{TE,i}=\frac{\eta_0}{\tilde{n}_{TE,i}}=\frac{\tilde{\eta}_i}{\cos\theta_i} \tag{2-49}$$

$$\tilde{\Gamma}_{TE,1}(0)=\frac{\tilde{n}_{TE,1}-\tilde{n}_{TE,2}}{\tilde{n}_{TE,1}+\tilde{n}_{TE,2}} \tag{2-50}$$

Reflection of Tissue on Glass

The setup for the analytical solution corresponding to the reflection imaging is shown in Fig. 2.2. The expressions for reflection and impedance at an oblique incidence for both TM and TE polarizations are now known. So it is possible to analytically solve for the reflected field from the tissue on the glass, provided that the properties of region 2 and region 3 are known. This process works by solving the reflection in each region from right to left, using the impedance at each boundary to relate the two regions. The value obtained from the analytical solution of the reflection can then be compared with the reflection mode imaging measurements obtained from the pulsed THz system.

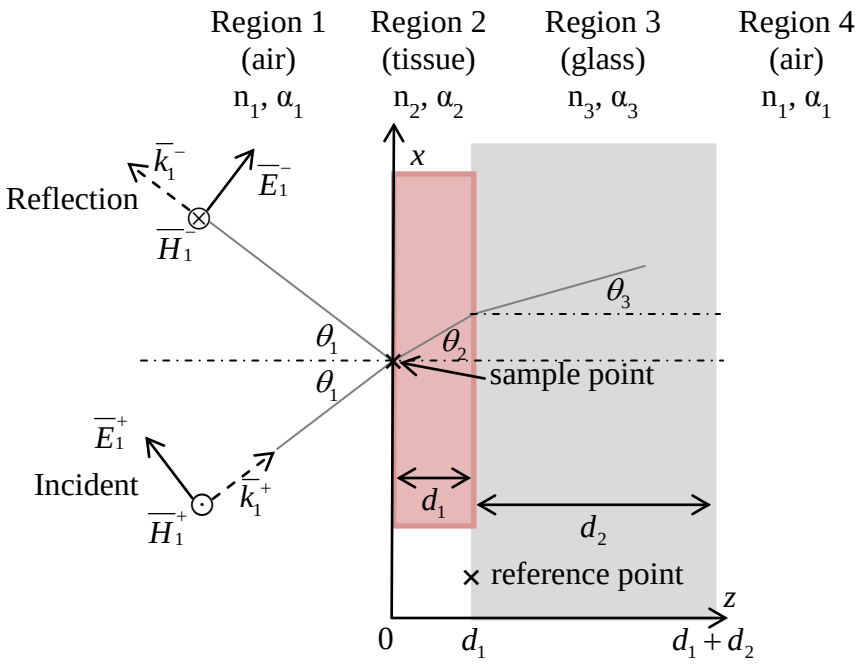

Figure 2.2. Reflection orientation of tissue on glass (TM polarization shown).

For the transmission of the sample it is necessary to obtain the transmitted field in region 4 of Fig. 2.2 by relating it back to the fields in each region until the incident field was found. However, for the reflection setup it was sufficient to simply find the reflection coefficient at the interface $z = 0$. Furthermore, it can be seen that applying the substitutions in equations (2-35) and (2-49) to the equations for impedance and reflection in each polarization results in equations (2-31) and (2-32) following the same form as equations (2-45) and (2-46) with the only difference being the polarization-dependent substitution. This allows for a general solution where the substitution can be undone once the final expression is known.

$$\tilde{n}_T = \tilde{n}_{TM} \text{ or } \tilde{n}_T = \tilde{n}_{TE} \tag{2-51}$$

$$\tilde{\eta}_T = \tilde{\eta}_{TM} \text{ or } \tilde{\eta}_T = \tilde{\eta}_{TE} \tag{2-52}$$

$$\tilde{Z}_T(z) = \tilde{\eta}_T \frac{1+\tilde{\Gamma}_T(z)}{1-\tilde{\Gamma}_T(z)} \tag{2-53}$$

$$\tilde{\Gamma}_T(z)=\frac{\tilde{Z}_T(z)-\tilde{\eta}_T}{\tilde{Z}_T(z)+\tilde{\eta}_T}=\frac{E_m^-}{E_m^+}e^{j2\tilde{k}\cos\theta z} \tag{2-54}$$

In this case the regions on either end of the setup in Fig. 2.2 extend indefinitely, so there is no returning signal in region 4 and therefore zero reflection. Thus it is possible to solve for the reflection at $z=0$ by finding the impedance and reflection values from right to left.

$$\tilde{\Gamma}_{T,4}\left(d_1+d_2\right)=0 \tag{2-55}$$

$$\tilde{Z}_{T,4}\left(d_1+d_2\right)=\tilde{\eta}_{T,4}=\tilde{Z}_{T,3}\left(d_1+d_2\right) \tag{2-56}$$

$$\tilde{\Gamma}_{T,3}\left(d_1+d_2\right)=\frac{\tilde{\eta}_{T,4}-\tilde{\eta}_{T,3}}{\tilde{\eta}_{T,4}+\tilde{\eta}_{T,3}}=\frac{\tilde{n}_{T,3}-\tilde{n}_{T,4}}{\tilde{n}_{T,3}+\tilde{n}_{T,4}} \tag{2-57}$$

$$\tilde{\Gamma}_{T,3}\left(d_1\right)=\tilde{\Gamma}_{T,3}\left(d_1+d_2\right)e^{-j2\tilde{k}_3\cos\theta_3 d_2}=\frac{\tilde{n}_{T,3}-\tilde{n}_{T,4}}{\tilde{n}_{T,3}+\tilde{n}_{T,4}}e^{-j2\tilde{k}_3\cos\theta_3 d_2} \tag{2-58}$$

$$\tilde{Z}_{T,3}\left(d_1\right)=\tilde{\eta}_{T,3}\frac{1+\tilde{\Gamma}_{T,3}\left(d_1\right)}{1-\tilde{\Gamma}_{T,3}\left(d_1\right)}=\tilde{Z}_{T,2}\left(d_1\right) \tag{2-59}$$

$$\tilde{\Gamma}_{T,2}\left(d_1\right)=\frac{\tilde{Z}_{T,2}\left(d_1\right)-\tilde{\eta}_{T,2}}{\tilde{Z}_{T,2}\left(d_1\right)+\tilde{\eta}_{T,2}}=\frac{\tilde{\eta}_{T,3}\dfrac{1+\tilde{\Gamma}_{T,3}\left(d_1\right)}{1-\tilde{\Gamma}_{T,3}\left(d_1\right)}-\tilde{\eta}_{T,2}}{\tilde{\eta}_{T,3}\dfrac{1+\tilde{\Gamma}_{T,3}\left(d_1\right)}{1-\tilde{\Gamma}_{T,3}\left(d_1\right)}+\tilde{\eta}_{T,2}}=\frac{\dfrac{\tilde{n}_{T,2}-\tilde{n}_{T,3}}{\tilde{n}_{T,2}+\tilde{n}_{T,3}}+\tilde{\Gamma}_{T,3}\left(d_1\right)}{1+\dfrac{\tilde{n}_{T,2}-\tilde{n}_{T,3}}{\tilde{n}_{T,2}+\tilde{n}_{T,3}}\tilde{\Gamma}_{T,3}\left(d_1\right)} \tag{2-60}$$

$$\tilde{\Gamma}_{T,2}\left(0\right)=\tilde{\Gamma}_{T,2}\left(d_1\right)e^{-j2\tilde{k}_2\cos\theta_2 d_1} \tag{2-61}$$

$$\tilde{Z}_{T,2}\left(0\right)=\tilde{\eta}_{T,2}\frac{1+\tilde{\Gamma}_{T,2}\left(0\right)}{1-\tilde{\Gamma}_{T,2}\left(0\right)}=\tilde{Z}_{T,1}\left(0\right) \tag{2-62}$$

$$\tilde{\Gamma}_{T,1}\left(0\right)=\frac{\tilde{Z}_{T,1}\left(0\right)-\tilde{\eta}_{T,1}}{\tilde{Z}_{T,1}\left(0\right)+\tilde{\eta}_{T,1}}=\frac{\tilde{\eta}_{T,2}\dfrac{1+\tilde{\Gamma}_{T,2}\left(d_1\right)e^{-j2\tilde{k}_2\cos\theta_2 d_1}}{1-\tilde{\Gamma}_{T,2}\left(d_1\right)e^{-j2\tilde{k}_2\cos\theta_2 d_1}}-\tilde{\eta}_{T,1}}{\tilde{\eta}_{T,2}\dfrac{1+\tilde{\Gamma}_{T,2}\left(d_1\right)e^{-j2\tilde{k}_2\cos\theta_2 d_1}}{1-\tilde{\Gamma}_{T,2}\left(d_1\right)e^{-j2\tilde{k}_2\cos\theta_2 d_1}}+\tilde{\eta}_{T,1}} \tag{2-63}$$

$$\tilde{\Gamma}_{T,1}(0)=\frac{\frac{\tilde{n}_{T,1}-\tilde{n}_{T,2}}{\tilde{n}_{T,1}+\tilde{n}_{T,2}}+\tilde{\Gamma}_{T,2}(d_1)e^{-j2\tilde{k}_2\cos\theta_2 d_1}}{1+\frac{\tilde{n}_{T,1}-\tilde{n}_{T,2}}{\tilde{n}_{T,1}+\tilde{n}_{T,2}}\tilde{\Gamma}_{T,2}(d_1)e^{-j2\tilde{k}_2\cos\theta_2 d_1}}=\frac{E^{-}_{m1,\text{tissue}}}{E^{+}_{m1}}=\frac{E_{sample}}{E_{inc}} \quad (2\text{-}64)$$

The final form of the reflection is presented in the form of equation (2-64) because the incident signal was not necessarily known during the measurement process. In order to compare the analytical solution to the measured fields, then, a reference signal from another point in the same scan must be taken. In this case the reflected signal from the slide glass in the absence of tissue can be used as shown in Fig. 2.3. The sample was not removed from the setup in order to obtain the reference signal. Instead, the same orientation was used with the measurement taken at a point off of the tissue, meaning that the distance from the emitter and receiver of the system to each interface did not change.

It should be noted that for this setup the additional distance d_1 in air constitutes a different phase shift than the one present in the setup with tissue on glass. This phase shift must

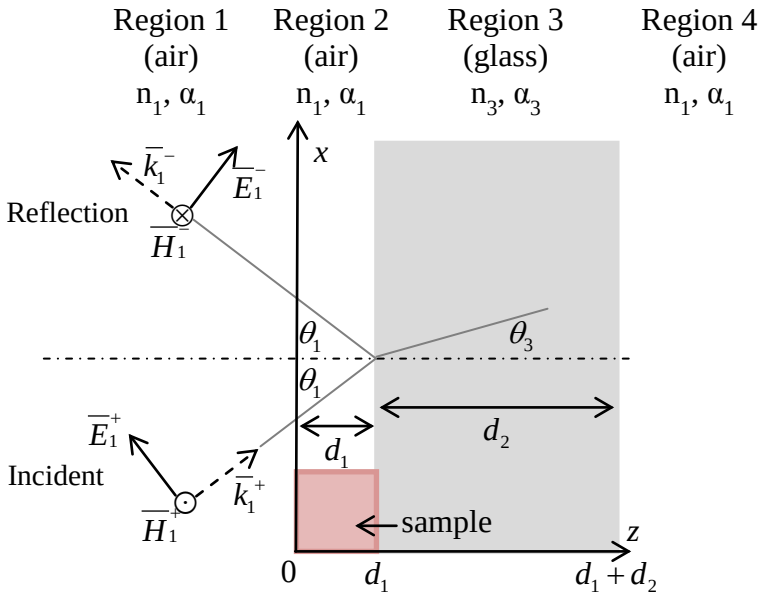

Figure 2.3. Diagram of reference signal calculation for reflection imaging.

be accounted for in the analytical solution. The formulation for the reflection in this case followed the same steps as the solution for the tissue on glass up to the impedance at $z = d_1$ given in equation (2-59).

$$\tilde{Z}_{T,3}(d_1) = \tilde{\eta}_{T,3}\frac{1+\tilde{\Gamma}_{T,3}(d_1)}{1-\tilde{\Gamma}_{T,3}(d_1)} = \tilde{Z}_{T,2}(d_1) \tag{2-65}$$

$$\tilde{\Gamma}_{T,2}(d_1) = \frac{\tilde{Z}_{T,2}(d_1)-\tilde{\eta}_{T,1}}{\tilde{Z}_{T,2}(d_1)+\tilde{\eta}_{T,1}} = \frac{\tilde{\eta}_{T,3}\dfrac{1+\tilde{\Gamma}_{T,3}(d_1)}{1-\tilde{\Gamma}_{T,3}(d_1)}-\tilde{\eta}_{T,1}}{\tilde{\eta}_{T,3}\dfrac{1+\tilde{\Gamma}_{T,3}(d_1)}{1-\tilde{\Gamma}_{T,3}(d_1)}+\tilde{\eta}_{T,1}} = \frac{\dfrac{\tilde{n}_{T,1}-\tilde{n}_{T,3}}{\tilde{n}_{T,1}+\tilde{n}_{T,3}}+\tilde{\Gamma}_{T,3}(d_1)}{1+\dfrac{\tilde{n}_{T,1}-\tilde{n}_{T,3}}{\tilde{n}_{T,1}+\tilde{n}_{T,3}}\tilde{\Gamma}_{T,3}(d_1)} \tag{2-66}$$

$$\tilde{\Gamma}_{T,1}(0) = \tilde{\Gamma}_{T,2}(0) = \tilde{\Gamma}_{T,2}(d_1)e^{-j2\tilde{k}_1\cos\theta_1 d_1} \tag{2-67}$$

$$\boxed{\frac{E^-_{m1,glass}}{E^+_{m1}} = \frac{\dfrac{\tilde{n}_{T,1}-\tilde{n}_{T,3}}{\tilde{n}_{T,1}+\tilde{n}_{T,3}}+\tilde{\Gamma}_{T,3}(d_1)}{1+\dfrac{\tilde{n}_{T,1}-\tilde{n}_{T,3}}{\tilde{n}_{T,1}+\tilde{n}_{T,3}}\tilde{\Gamma}_{T,3}(d_1)}e^{-j2\tilde{k}_1\cos\theta_1 d_1} = \frac{E_{ref}}{E_{inc}}} \tag{2-68}$$

Upon dividing equation (2-64) by equation (2-68), the dependence on E_{inc} is dropped and the remaining function is the term E_{samp}/E_{ref}, which are both measured values. A substitution for the reflection at a single interface can be used for clarity prior to this division.

$$\rho_{T,ij} = \frac{\tilde{n}_{T,i}-\tilde{n}_{T,j}}{\tilde{n}_{T,i}+\tilde{n}_{T,j}}, \quad \text{i, j} = 1,2,3,4... \tag{2-69}$$

$$\frac{E_{sample}}{E_{inc}} = \frac{\rho_{T,12}+\tilde{\Gamma}_{T,2}(d_1)e^{-j2\tilde{k}_2\cos\theta_2 d_1}}{1+\rho_{T,12}\tilde{\Gamma}_{T,2}(d_1)e^{-j2\tilde{k}_2\cos\theta_2 d_1}} = \frac{\rho_{T,12}+\dfrac{\rho_{T,23}+\tilde{\Gamma}_{T,3}(d_1)}{1+\rho_{T,23}\tilde{\Gamma}_{T,3}(d_1)}e^{-j2\tilde{k}_2\cos\theta_2 d_1}}{1+\rho_{T,12}\dfrac{\rho_{T,23}+\tilde{\Gamma}_{T,3}(d_1)}{1+\rho_{T,23}\tilde{\Gamma}_{T,3}(d_1)}e^{-j2\tilde{k}_2\cos\theta_2 d_1}} \tag{2-70}$$

$$\frac{E_{ref}}{E_{inc}} = \frac{\rho_{T,13}+\tilde{\Gamma}_{T,3}(d_1)}{1+\rho_{T,13}\tilde{\Gamma}_{T,3}(d_1)}e^{-j2\tilde{k}_1\cos\theta_1 d_1} \tag{2-71}$$

$$\tilde{\Gamma}_{T,3}\left(d_1\right) = \rho_{T,31} e^{-j2\tilde{k}_3 \cos\theta_3 d_2} \tag{2-72}$$

Where $\rho_{T,ij}$ represents the reflection in arbitrary region *i* at a single interface with arbitrary region *j* for TE or TM polarization denoted by subscript *T*. Thus the relationship between the measured signals is defined as the following expression:

$$\frac{E_{sample}}{E_{ref}} = \left[\frac{\rho_{T,12} + \dfrac{\rho_{T,23} + \rho_{T,31} e^{-j2\tilde{k}_3 \cos\theta_3 d_2}}{1 + \rho_{T,23}\rho_{T,31} e^{-j2\tilde{k}_3 \cos\theta_3 d_2}} e^{-j2\tilde{k}_2 \cos\theta_2 d_1}}{1 + \rho_{T,12} \dfrac{\rho_{T,23} + \rho_{T,31} e^{-j2\tilde{k}_3 \cos\theta_3 d_2}}{1 + \rho_{T,23}\rho_{T,31} e^{-j2\tilde{k}_3 \cos\theta_3 d_2}} e^{-j2\tilde{k}_2 \cos\theta_2 d_1}} \right] \left[\frac{1 + \rho_{T,13}\rho_{T,31} e^{-j2\tilde{k}_3 \cos\theta_3 d_2}}{\rho_{T,13} + \rho_{T,31} e^{-j2\tilde{k}_3 \cos\theta_3 d_2}} \right] e^{j2\tilde{k}_1 \cos\theta_1 d_1} \tag{2-73}$$

The reflected signal for the TM and TE modes can then be found by substituting the different values of ρ_T in (2-73) with the appropriate reflection expression from equation (2-34) or (2-48), respectively. Also, in a setup where the incident signal arrives from a region of air, with the assumption that $\tilde{n}_{air} = 1$. Thus any term comparing the refractive index and angle can be expressed in terms of the incident angle.

$$\tilde{n}_1 \sin\theta_1 = \tilde{n}_2 \sin\theta_2 = \tilde{n}_3 \sin\theta_3 = \ldots = (1)\sin\theta_{inc} \tag{2-74}$$

Where θ_{inc} is the angle of the incident signal in air. In the setup of Fig. 2.2 and 2.3 this is the same angle θ_1 for the incident signal arriving in region 1. Applying this substitution to equations (2-34) and (2-48) shows that any given reflection in equation (2-69) can be defined in in terms of the incident angle in region 1 using Snell's law.

$$\tilde{n}_i \cos\theta_j = \tilde{n}_i \sqrt{1 - \sin^2\theta_j} = \tilde{n}_i \sqrt{1 - \tilde{n}_j^{-2} \sin^2\theta_{inc}} \tag{2-75}$$

$$\rho_{TM,ij} = \frac{\tilde{n}_i \cos\theta_j - \tilde{n}_j \cos\theta_i}{\tilde{n}_i \cos\theta_j + \tilde{n}_j \cos\theta_i} = \frac{\tilde{n}_i^2 \sqrt{\tilde{n}_j^2 - \sin^2\theta_{inc}} - \tilde{n}_j^2 \sqrt{\tilde{n}_i^2 - \sin^2\theta_{inc}}}{\tilde{n}_i^2 \sqrt{\tilde{n}_j^2 - \sin^2\theta_{inc}} + \tilde{n}_j^2 \sqrt{\tilde{n}_i^2 - \sin^2\theta_{inc}}} \tag{2-76}$$

$$\rho_{TE,ij} = \frac{\tilde{n}_i \cos\theta_i - \tilde{n}_j \cos\theta_j}{\tilde{n}_i \cos\theta_i + \tilde{n}_j \cos\theta_j} = \frac{\sqrt{\tilde{n}_i^2 - \sin^2\theta_{inc}} - \sqrt{\tilde{n}_j^2 - \sin^2\theta_{inc}}}{\sqrt{\tilde{n}_i^2 - \sin^2\theta_{inc}} + \sqrt{\tilde{n}_j^2 - \sin^2\theta_{inc}}} \quad (2\text{-}77)$$

This means of expressing the reflection terms is primarily for convenience in computation. Additionally, the expressions in equations (2-76) and (2-77) and the recursive relationship of the reflection coefficients shown in equations (2-64) and (2-68) agree with the methodology for finding reflection from multiple layers detailed in [62].

B. Validation of Experimental Reflected Signals with TE and TM Formulations

The reflection imaging signals were validated by comparing the calculated values in equation (2-73) to measured values obtained from the reflection imaging scan. The calculated values in this comparison were found using the values of the refractive index, absorption coefficient, and thickness of each tissue region from each sample. While the data of the glass could be obtained from literature, the properties of the FFPE breast cancer tissue had not been obtained previously. Thus this work used the results from Chapter 3 for each of these regions. The measured ratio was obtained by selecting five points from each tissue region defined on the sample and averaging the frequency domain signals for E_{sample}, then taking the point of highest reflection from the glass as E_{ref}. For the sake of this comparison, only the magnitude was used, so the phase in the equation for the calculated reflection can be dropped.

$$\left|\frac{E_{sample}}{E_{ref}}\right| = \left|\left[\frac{\rho_{T,12} + \dfrac{\rho_{T,23} + \rho_{T,31}e^{-j2\tilde{k}_3\cos\theta_3 d_2}}{1+\rho_{T,23}\rho_{T,31}e^{-j2\tilde{k}_3\cos\theta_3 d_2}} e^{-j2\tilde{k}_2\cos\theta_2 d_1}}{1+\rho_{T,12}\dfrac{\rho_{T,23} + \rho_{T,31}e^{-j2\tilde{k}_3\cos\theta_3 d_2}}{1+\rho_{T,23}\rho_{T,31}e^{-j2\tilde{k}_3\cos\theta_3 d_2}} e^{-j2\tilde{k}_2\cos\theta_2 d_1}}\right]\left[\frac{1+\rho_{T,13}\rho_{T,31}e^{-j2\tilde{k}_3\cos\theta_3 d_2}}{\rho_{T,13}+\rho_{T,31}e^{-j2\tilde{k}_3\cos\theta_3 d_2}}\right]\right| \quad (2\text{-}78)$$

As stated in the previous section, the reflection components of equation (2-78) are dependent on the polarization of the incident signal. However since the polarization of the

system could not be confirmed with certainty the comparison was made using both modes. From a mathematical standpoint the use of an exclusively TE or exclusively TM solution represents the limits of the reflection at an oblique angle, and solutions of non-specific polarizations should be a combination of the two polarizations. Ideally then, the ratio of the measured tissue reflection to the measured glass reflection should also be a combination of the two different solutions.

The comparison was made for slide #3 of each sample, with Sample 1 given in Fig. 2.4, Sample 2 given in Fig. 2.5, and Sample 3 given in Fig. 2.6. Each plot shows the values of the ratio between the measured sample reflection and measured reference compared to the reflection for the TE mode in equations (2-78) and (2-77), the TM mode in equations (2-78) and (2-76).

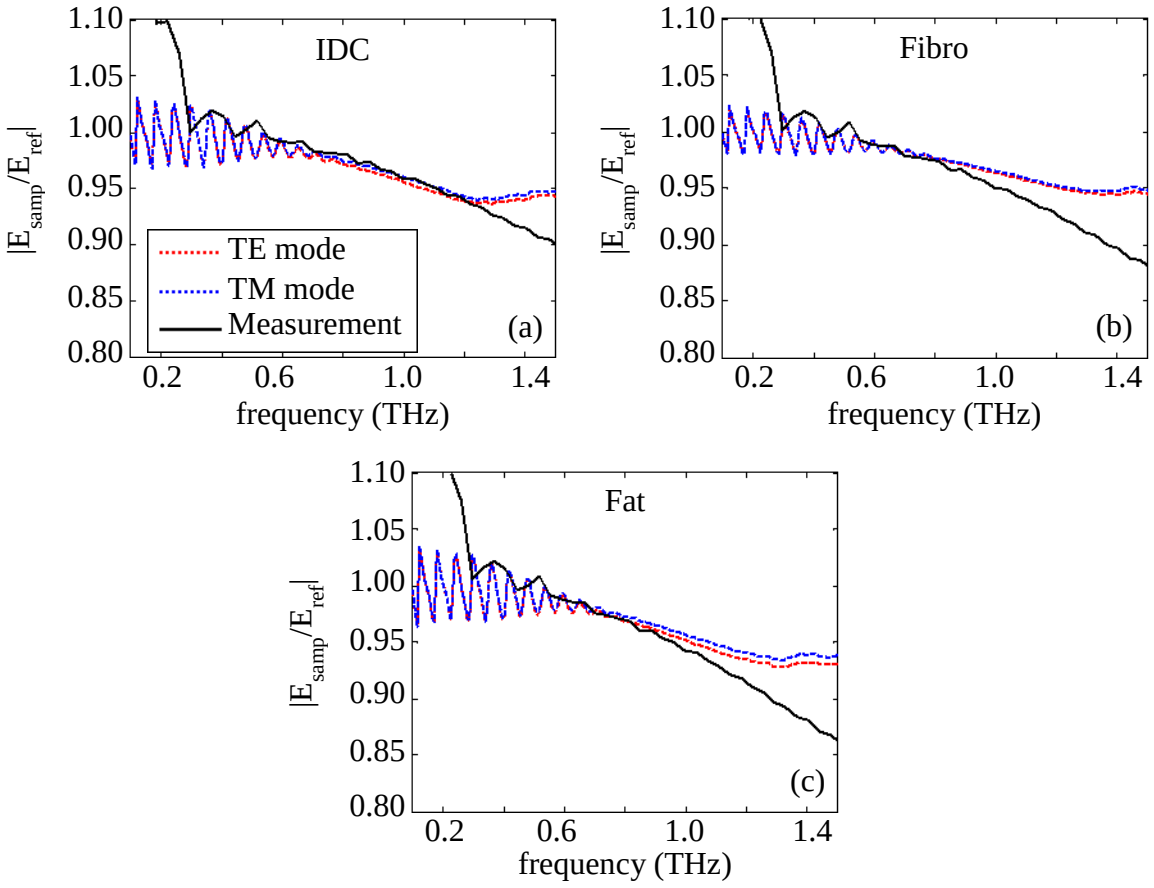

Figure 2.4. Comparison for slide #3 of 40 year old patient (Sample 1) of tissue reflections versus reference for (a) IDC, (b) fibroglandular, and (c) fatty tissue.

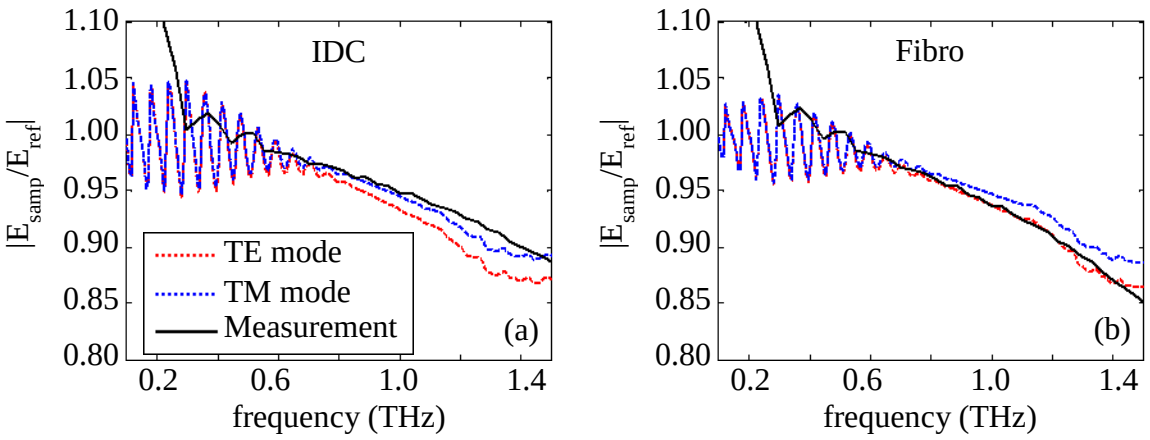

Figure 2.5. Comparison for slide #3 of 46 year old patient (Sample 2) of tissue reflections versus reference for (a) IDC and (b) fibroglandular tissue.

The incident angle θ_{inc} used in equations (2-76) and (2-77) was 30° in accordance with the system setup.

Overall the comparison of the measurements of the three different samples was in very good agreement to the theoretical reflections of TE and TM modes from equation (2-78). It was observed that there was small numerical error at low frequencies. The primary differences that appear in all cases were in the low frequency band, where the calculated values had strong oscillations while the measured values showed much less movement. For the sake of simplicity the frequencies below 0.25 THz were not considered in this case due to the strong divergence of the measured ratios to the calculated values at that limit. The low frequency oscillations of the calculated reflections were primarily due to the theoretical formulations of the reflection taking into account multiple reflections in the glass slide. This can be seen intuitively by noting that the oscillations decrease with increasing frequency. The dielectric properties of the glass obtained from Chapter 3 indicated that the absorption of the glass increases with frequency as well. This means that high frequency signals were absorbed rather than providing multiple reflections in the measurement.

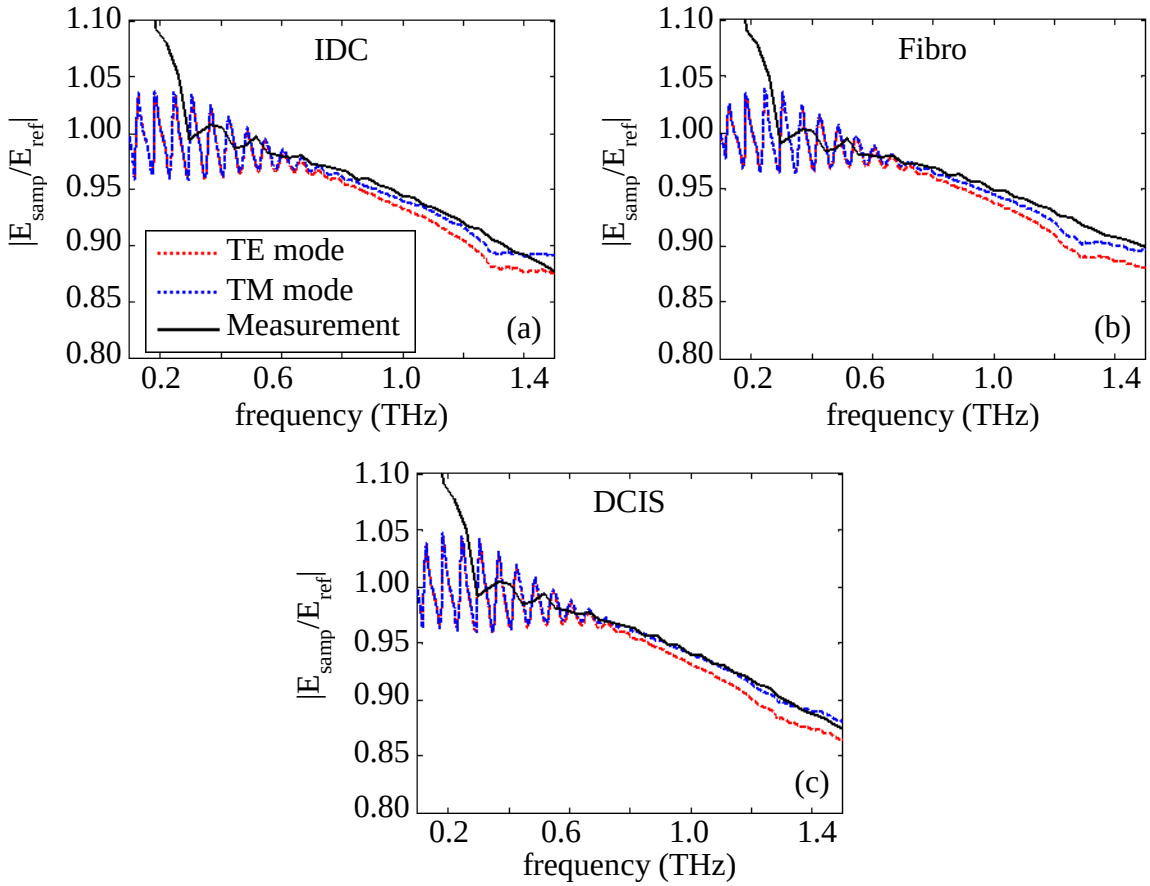

Figure 2.6. Comparison for slide #3 of 22 year old patient (Sample 3) of tissue reflections versus reference for (a) IDC, (b) fibroglandular, and (c) DCIS.

There were two possibilities for why the same effect was not witnessed in the measurement signals. The first was that while the calculated values solve for all reflections, the time gating of the reflection measurements was limited. Thus many of the additional reflections that may have been present later in the time domain signal were not accounted for in the measurement. The second potential reason was in the discretization of the frequency domain plots. The plots obtained from theoretical formulations had a $\Delta f_{theory} = 6.07$ GHz , while the plot of the measurement values had a much larger discretization of $\Delta f_{meas} = 36.90$ GHz . These numbers were significant when attempting to discretize highly oscillating data at lower frequencies. In other words many of the oscillations may not have been captured between the

frequency points of the measurement data. The upward deflection of the theoretical values at 1.2 THz was due to the valid limits of the signal properties obtained in Chapter 3.

C. Terahertz Imaging System Setup

The imaging of the tissue samples throughout this research used the reflection imaging module (RIM) of the pulsed THz system shown in Fig. 2.7. The overall imaging steps used for the samples were established via early imaging of the tissue samples presented in Section 1.3 as well as on an earlier sample set of tissue from CHTN. Unfortunately the samples obtained prior to the ones detailed in this work were found to not contain a significant amount of cancerous tissue, nor was the preparation of the FFPE sections on slides suitable for further research. However, the work performed on those samples was used to establish the methodology of imaging the samples for this work. Transmission imaging was also applied to the current sample set, but it was found that the glass slide attenuates the signal significantly such that a proper image cannot be resolved. Thus only reflection imaging is considered for the purpose of this research.

The standard setup for the reflection imaging began with optimizing the reflected signal from a gold mirror. This process involved first purging the chamber holding the RIM mirror base

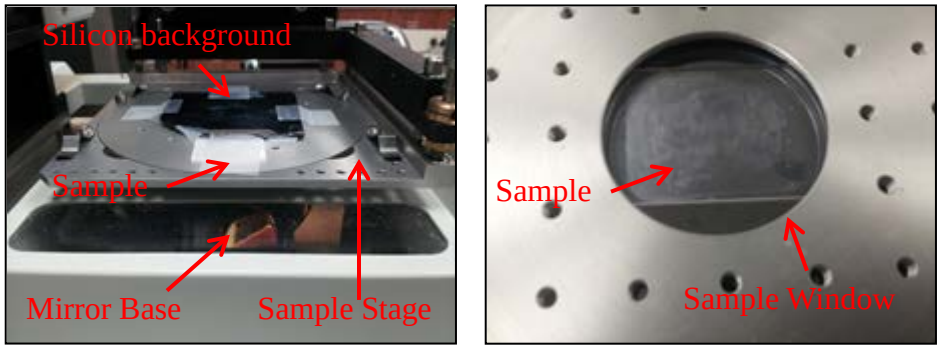

(a) (b)

Figure 2.7. Tissue sample on glass slide mounted in the reflection imaging module, depicted with a silicon background. Views given from (a) the side and (b) below.

with nitrogen for no less than 15 minutes in order to remove any water vapor from the chamber. The system chamber below the RIM remained sealed throughout the imaging process, meaning that only the initial purge caused a delay, and a constant low flow of nitrogen maintained the neutral air in the chamber for subsequent imaging. The next calibration step required setting the *z*-position of the RIM stage in order to maximize the reflected signal. Then the RIM platform holding the sample was adjusted in both *x* and *y* directions in order to minimize any change in the *z*-position across the surface of the mirror. The gold mirror was the standard calibration tool for preparing the reflection imaging since it provided a nearly complete reflection of the incident signal. Thus it served as a reasonable reference for the imaging application.

Early system strength testing showed that the measured field reflected from the gold mirror varied slightly over time. While the effects of this small deviation are not significant for all applications, in this case the samples being imaged were very thin, so the reflection difference between the unique tissue regions was small. For this reason it was necessary to have an accurate measurement of the incident signal strength or an equivalent reference that could be compared against the signals acquired in any given imaging scan. Thus each scan included saving the waveform of the signal reflected from the mirror after the RIM stage was balanced. In this way the scans could be adjusted based on the signal strength at the time of the image acquisition in order to make measurements across several days comparable. A comparison of the images obtained across several days is given in Fig. 2.8. Each image was obtained by plotting the time domain peak after the signal has been normalized against the peak value of the signal reflected from the gold mirror reference. The slide used for this comparison was from slide #3 from Sample 2. This basic comparison showed that the images can be reliably compared via normalization even with shifts in the reference peak.

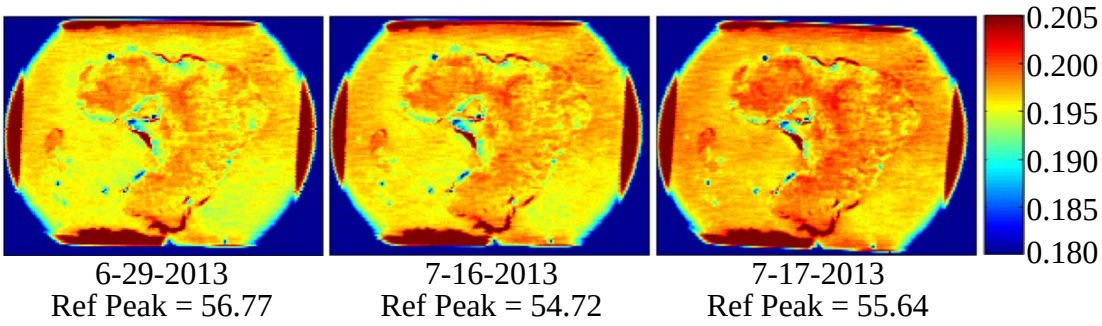

Figure 2.8. Day to day comparison of reflection images of 46 year old patient (Sample 2), slide #3, with date stamps and reference peak values listed. All values are normalized against reference peak.

Once the system was calibrated to offer the maximum reflection across the surface of the gold mirror, the mirror was removed and a baseline measurement was taken of the empty RIM stage. This baseline served as a measurement of the overall internal system noise at the time of scanning and was used in the deconvolution process. In all of the measurements used in this research the baseline was very small compared to the reference and sample signals, so any effect of noise inside of the system was negligible.

Following the baseline measurement, the tissue section being imaged was placed on the RIM stage as shown in Fig. 2.7(a). As mentioned previously, all of the tissue samples in this research were obtained already mounted on glass slides. For the reflection imaging the glass served as a background material with reasonably strong reflection. An additional piece of undoped silicon was used to mount the glass slide and tissue such that the slide was inverted on the RIM with the tissue exposed to the incident signal. Testing of the silicon backing showed that there was no significant difference in the resulting images from the silicon. Thus it simply allowed for consistent mounting and positioning of the sample and prevented any interference from outside sources. Once the sample was positioned in the window of the imaging module as shown in Fig. 2.7(b), the system was once again checked by adjusting the *z*-position and *x* and *y*

balance of the RIM stage to ensure a maximum and consistent reflection across the surface of the sample and the glass.

The standard setup for consistent scan positioning across several samples involved a two-step scanning process. The first step used a rapid, low-resolution scan over a large area of the RIM window in order to determine the exact positioning of the sample on the stage. For all imaging in this research the positioning step used a scan area of 3.5 cm × 3.5 cm with a step size of 400 μm. From this scan it was possible to define the area of interest for the more detailed scan. The next step utilized a scan with a smaller scan area and a step size of 200 μm, allowing for a higher resolution scan of the tissue. An example of this process to obtain the high resolution imaging scan can be seen in Fig. 2.9 for slide #3 of Sample 1. The circular edge on the left and right sides of the scan indicates the circular sample holder window in the RIM where the magnitude of the reflection is outside of the color range being plotted. The flat edge at the top and bottom of the scan corresponds to the edge of the glass slide where the signal does not reflect significantly. This figure also shows that reducing the step size of the scan by half improved the

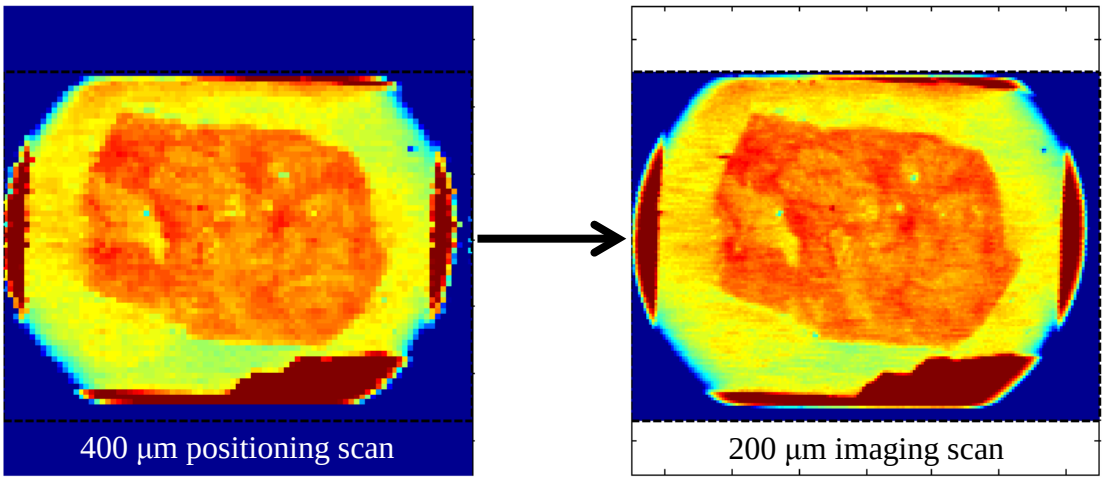

Figure 2.9. Standard imaging steps: positioning scan with a 400 μm step size used to define window area for the 200 μm step size imaging scan.

resolution of the resulting image in order to better view the features of the sample under test. For this reason the 200 μm step size for the reflection imaging was considered sufficient for subsequent imaging of the breast cancer samples in this research as it provided a balance of image resolution and scanning time.

D. Signal Processing for Terahertz Imaging

Following the image acquisition, the data from the scan was saved as a time domain waveform across an array of points corresponding to the scan steps. It was possible to perform individual processing on each of these waveforms in order to construct a set of THz images from the scan. The most basic means of comparing the images obtained across several samples or several days was mentioned previously as the normalization used in Fig. 2.8. In this basic process the entire time domain signal for each point in the scan was divided by a peak value of the signal denoted as the reference. This reference could either be taken as the gold mirror, which offered an ideal reflected signal, or a point on the glass slide, which provided a signal peak characteristic of the sample without the tissue present. The selection of the reference was dependent on the comparison being sought. For simple normalization this choice offered no change other than setting the range of the values being plotted.

One concern with the 200 μm step size image obtained in Fig. 2.9 as well as in other images obtained in this research from simple normalization was the noticeable amount of horizontal smearing of the signal magnitude across the image in Fig 2.9(b). This effect was primarily due to noise brought about by the particularly thin tissue sample, since the variation in response across the regions was small and thus sensitive to any subtle change in reflection from the movement of the stage or minor fluctuations in the signal. There were a number of different

signal processing techniques investigated to attempt to remove the effects of this noise, such as deconvolution and signal averaging.

Deconvolution

One method for attempting to remove the contribution of system noise from the time domain image involved applying the reference signal to the measured reflections using a deconvolution process. The basic steps for applying this operation to the two time domain signals are shown in Fig. 2.10. In this process, the Fourier transform was used to find the frequency domain signal of the reference and at each point in the scan. Then the signal from each point was divided by the reference signal across the spectrum in order to obtain the new frequency domain signal. The very low signal at higher frequencies in the reference in this process caused a significant amount of large noise when the division was applied, so a filter had to be imposed on the resultant waveform prior to applying an inverse Fourier transform to obtain the deconvolved time domain signal.

The resulting signal of the deconvolution generally leaves an impulse function where the peak corresponds to the reflections in the signal. In this work a basic cutoff filter was used in the

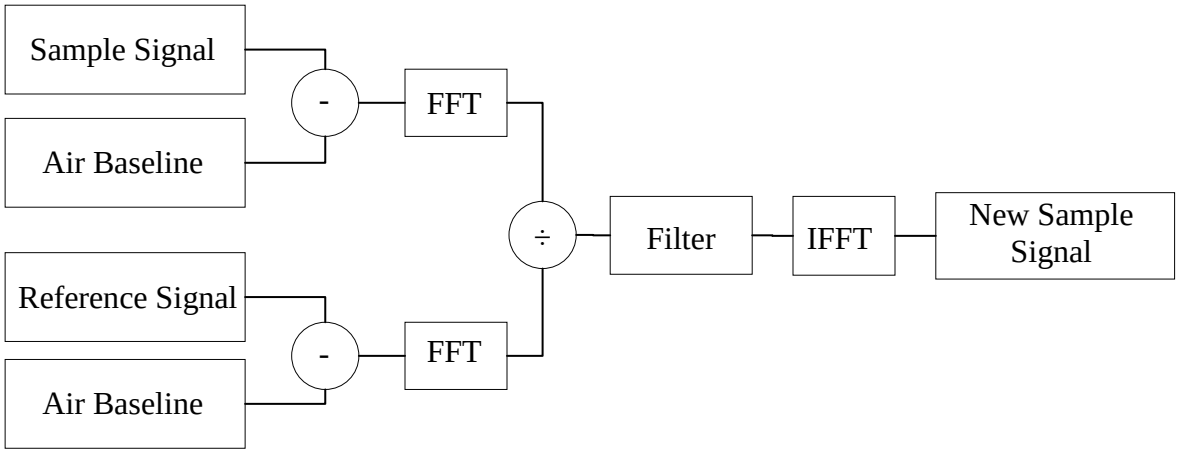

Figure 2.10. Basic deconvolution process for image processing.

frequency domain, which results in ringing effects in the final time domain signal following the inverse Fourier transform. However for a very thin tissue the only significant impulse was from the primary reflection meaning that any noisy effects away from the impulse were not important for the imaging. This process can be seen more easily in Fig. 2.11 for an arbitrary point taken from the center of the scan of slide #3 of the Sample 1 with the gold mirror serving as the reference. The strong difference between the ideal reference and the reflected signal was obvious in both the time and frequency domain comparisons. The plots in Fig. 2.11(c) show the signal of

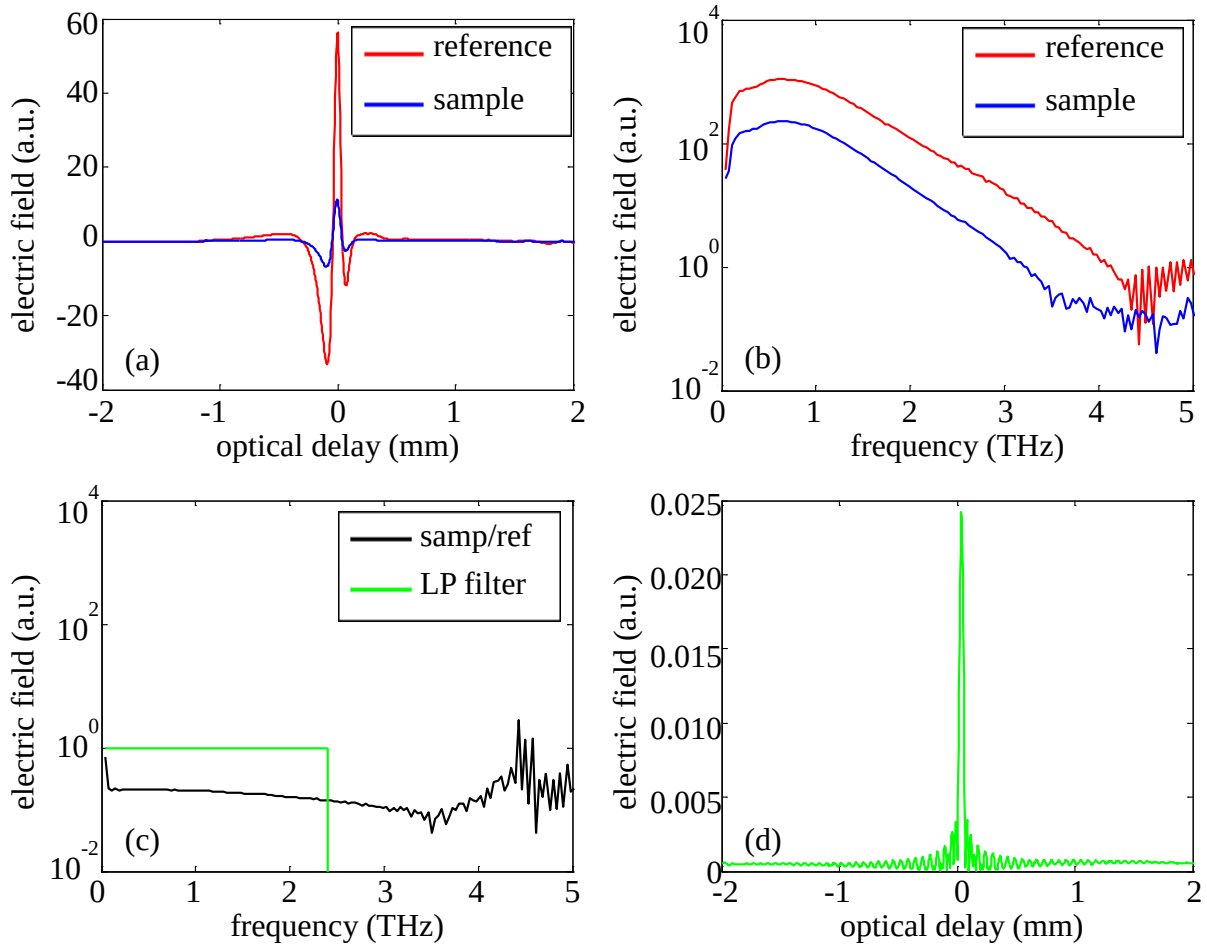

Figure 2.11. Deconvolution process for reflection imaging: (a) time domain reference and sample signals, (b) frequency domain magnitude of reference and sample signals, (c) new signal obtained from dividing sample signal by reference signal and frequency domain filter as well as the low-pass filter applied to the signal, and (d) new time domain signal obtained from inverse Fourier transform.

the sample divided by the reference in the frequency domain, as well as the low-pass filter to be applied. A fairly low cutoff of the filter was selected due to some noise beginning to arise between 2.5 and 3 THz in the frequency domain signals. The time domain signal following the inverse Fourier transform of the filtered spectrum is shown in Fig. 2.11(d). As stated before the oscillations in the new time domain signal were due to the sharp edge of the cutoff filter being applied to the new signal and did not have a significant effect in this research. However, for applications with thicker tissue it is likely that multiple reflection peaks will appear in the time domain signal. For the processing of thicker samples the Gaussian filter will be more ideal for observing possible multiple reflections in the time domain signal without causing interference between the peaks.

Figure 2.12 shows the comparison between the time domain images obtained from the normalized peak of the measured reflection signals and the image obtained from taking the peak of the deconvolved time domain signal obtained at each point in the scan. In this case it was necessary to plot the two images on separate scales due to the different processes involved in obtaining the images. It could be seen that the deconvolution method removed a small amount of the smearing in the image and improved the clarity of the different tissue regions. However, it

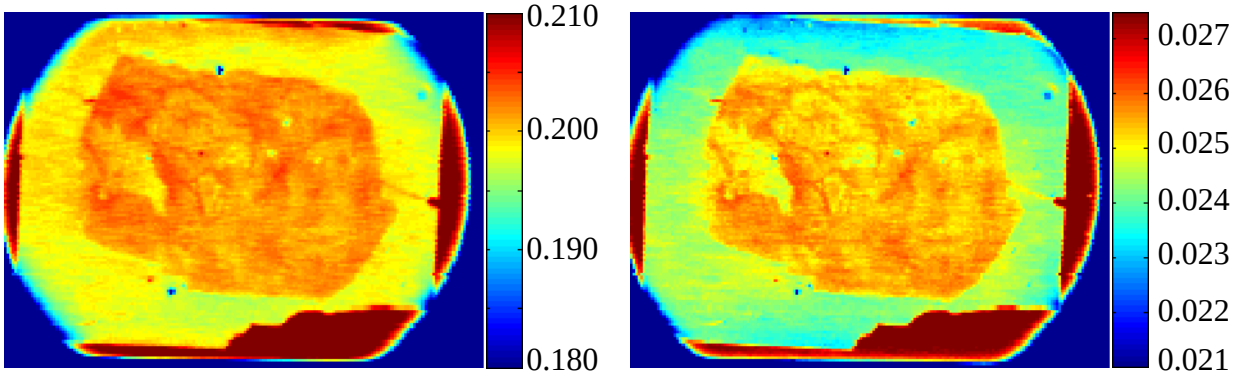

Figure 2.12. Comparison of time domain peak magnitude images using (a) normalization against reference peak and (b) deconvolution of the reference from the signal.

did not provide a significant overall improvement in this case. Additionally it was found that small changes in the reference signal did cause significant shifts in the magnitudes of the image post-deconvolution, meaning that a comparison across several days or several samples as with the normalization in Fig 2.8 was not feasible using the deconvolution process. Thus while the deconvolution image was used in this research for observing a single slide, comparisons across several slides were obtained using simple normalization of the signal peak.

Signal Averaging

Another technique that could be used to improve the images obtained from the reflection imaging scans was averaging for each point in the scan. This operation is a defined parameter of the scan settings in the TPS Spectra system and was set prior to the imaging process. Rather than a single time domain signal representing each point, a set number of measurements were taken for each point and averaged together. This operation significantly reduced the noise present in the final image. Unfortunately the sampling rate of the imaging module remains unchanged when performing the averaging, so the number of measurements taken at each point resulted in the overall scan time being multiplied by the same factor. Thus it was deemed to be inefficient for maintaining reasonable scanning times in this research.

In order to demonstrate the effectiveness of this technique, a portion of slide #3 of Sample 1 was imaged using signal averaging of four measurements. The comparison can be seen in Fig. 2.13, which shows that the noise in the one-fourth scan of the image was significantly reduced by using the signal averaging. The 200 μm image presented without averaging in this case shows even more noise than the one compared by deconvolution in Fig. 2.12 and had much more smearing. Even with the additional noise the signal averaging greatly improved the resulting image. This indicates that the smearing was likely an effect of small fluctuations in the

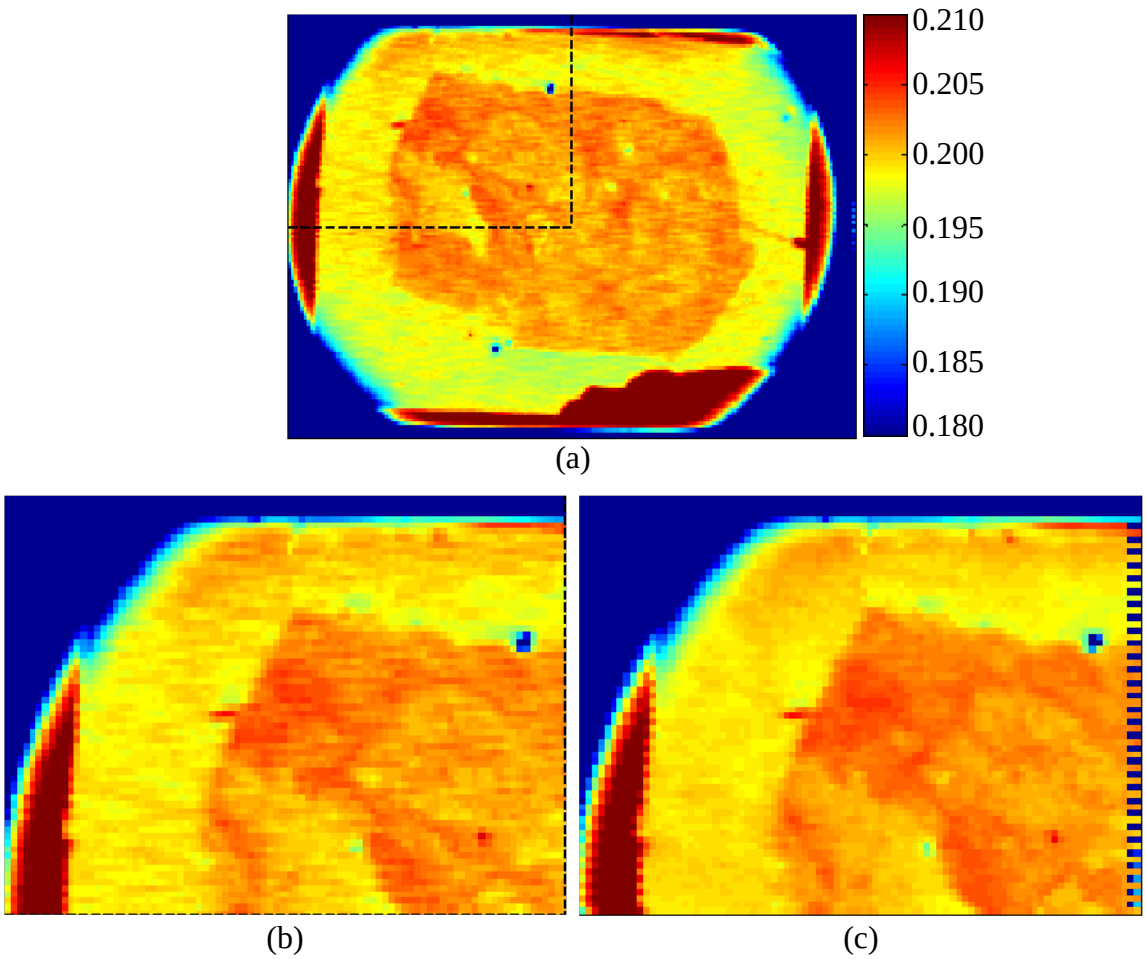

Figure 2.13. Comparison of signal averaging for Sample 1, slide #3 with (a) the full size image with 200 µm step size, (b) the upper left quadrant image with 200 µm step size and no signal averaging, and (c) the upper left quadrant scanned again with 200 µm step size obtained from the average of four signals at each point.

signal over time as the sample was scanned. This noise was then decreased when the signal was averaged over a few measurements in time. These small fluctuations were only significant in viewing the image due to the very thin section of tissue. Thus differences between the regions of the tissue were minimal. For a thicker tissue section the range of reflection peaks should be much wider, so a small change in the signal throughout the scan would become insignificant compared to the contrast in the image. The success of the averaging of the time domain signals during the scan in noise suggests that standard imaging processing techniques like averaging or filtering

would be useful. Nevertheless the use of signal averaging remains a means for improving the imaging scans for future applications as well, provided that the samples are small.

Frequency Domain Imaging

In addition to operations on the time domain signals at each point, the Fourier transform also allows for the simple images showing the magnitudes of the different frequency components of the signal. These images can then be either compared individually to the histopathology or can be normalized in order to obtain a comparison across a range of frequencies. This comparison allows for an imaging representation of how the reflections of the different regions shift over frequency. In order to obtain this normalization, the standard gold mirror reference can be used in a similar way to the time domain peak normalization, only instead each frequency range value is normalized against the frequency range magnitude of the reference at that frequency. Alternate references for the normalization are a reflection measurement from the glass slide surrounding the tissue section or from the paraffin on the slide where the tissue is not present in the section. Several frequency images were obtained as part of the comparison of the THz imaging to the histopathology, and an example of two kinds of normalization will be shown following the initial histopathology comparison to observe the change in reflection over frequency.

E. Terahertz Imaging and Histopathology Comparison

For the comparison of THz reflection imaging and the histopathology results of the H&E stained slides, imaging scans were performed on all nine FFPE slides from each of the three patients. Additionally, basic frequency domain images were obtained from slide #3 of each of the samples in order to gain a basic comparison of the images at different frequencies. For the sake of clarity the imaging of slide #3 of each sample will first be presented individually, and the comparison across several slides in from the same sample will be given as part of the discussion.

In order to provide a full comparison of the images obtained from slide #3 of each sample, both a photograph of the FFPE tissue section on glass and the H&E stained pathology image of slide #2 from the same sample are presented. The time domain image of the scan was obtained from the deconvolution method used in the previous section and corresponds to the magnitude of the resultant time domain signal at each point. Then for the frequency domain images the magnitude of the spectrum at 1.0, 1.5, and 2.0 THz was obtained at each point to obtain an image. In order to express the images on a meaningful scale, the magnitude was normalized against the maximum magnitude of the scan at that same frequency, which was invariably a point on the glass surrounding the FFPE section. Additionally, each frequency image was scaled individually in order to denote the contrast between regions. The separate scales were necessary due to the gradual decrease in values with increasing frequency, which made plotting all three frequency images on the same scale impractical for providing a useful comparison. However the scale at each frequency was kept consistent across the three samples for the sake of comparison. While frequencies up to 3.5 THz were available from the Fourier transform of the reflection image, only images up to 2.0 THz were obtained due to increasing noise at higher frequencies.

Sample 1: Comparison of THz Imaging to Pathology

The results of the 40 year old patient are given in Fig. 2.14, and the comparison of the other slides from the same sample is given in Fig. 2.15. As the histopathology of this sample noted, the tissue regions of the 40 year old patient were poorly differentiated from each other, so the regions denoted as IDC, fibroglandular, and fatty tissue in the pathology were not necessarily easy to distinguish. In addition to the three generally defined tissue regions, there was small area of interest denoted by the arrow in Fig. 2.14(b) that was defined to be a lymphoid aggregate with

an infiltrating ductal carcinoma core. This location and another area of interest, denoted by the rectangular boxes in Fig. 2.14(c), were investigated using high resolution scanning in order to compare the high power pathology imaging to the THz system. The FFPE slide in Fig. 2.14(a) did not allow for a clear visual distinction of the tissue regions independent of pathology. An

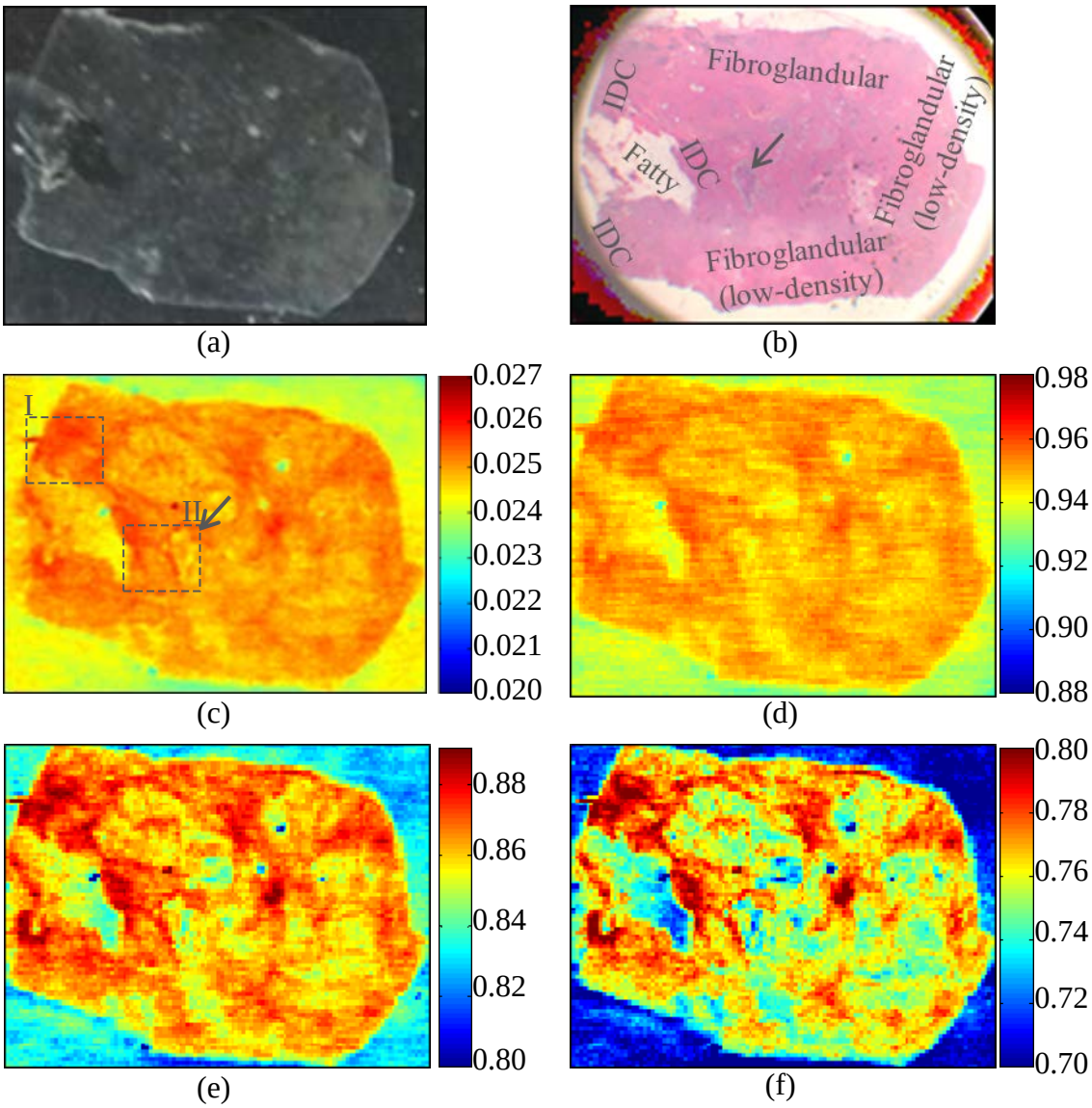

Figure 2.14. Comparison of results for slide 3 of Sample 1: 40 year old Caucaasian woman diagnosed with infiltrating ductal carcinoma (IDC). (a) Photographic image of the tissue on glass slide. (b) Low power pathology image used for correlation. (c) THz time domain image of the sample with rectangular indicators of the regions later observed in high resolution imaging. Frequency domain images at (d) 1.0 THz, (e) 1.5 THz, and (f) 2.0 THz. Frequency domain images are normalized to the maximum reflection of the surrounding glass at that frequency.

additional region of interest could be seen in the high reflection value in the center of the fibroglandular tissue. This region was not originally denoted as IDC, but due to the high heterogeneity of the tissue it is possible that this was also a region of cancer.

Comparing the time domain image in Fig. 2.14(c) to the H&E pathology slide showed that the area denoted as IDC provided the highest reflection values across the tissue. However, the regions of cancer on the slide were difficult to distinguish with great certainty due to mixing with the surrounding fibroglandular tissue. In this way the assessment of poorly differentiated infiltrating ductal carcinoma could be seen in the reflection images. Additionally the fibroglandular regions of the tissue varied from high density to low density, with lower density fibroglandular tissue corresponding to increased fat tissue in that region. These variations in the density of the fibroglandular tissue could be seen in the time domain image as well, most prominently when observing the upper left part of the tissue for high density fibroglandular and the lower right part of the tissue for low density fibroglandular tissue. From these results it was clearly seen that the density had an effect on the values that are reflected from the tissue, with the higher density tissue giving a stronger reflection that decreases moving toward the low density areas. Finally, the fatty tissue region identified in the pathology showed the lowest reflection of the three tissue regions, being very close to that of the surrounding paraffin. This supported the trend of the lower density fibroglandular tissue (i.e. increasing fatty tissue content) showing decreased values from the high density fibroglandular tissue and therefore lying between fully fibroglandular and fully fatty tissue.

Comparison across the frequency domain images showed that the higher reflection in the infiltrating ductal carcinoma was consistent in the frequencies observed. Also it could be observed that the increasing frequencies provided better definition of various regions in the scan.

However, this came with the trade-off of increased grainy noise in the image due to the effects of signal noise at higher frequency. Taking particular note of the individual frequency images showed that 1.5 THz and 2.0 THz provided the best clarity between regions and denoted all of the primary regions of IDC on the slide, whereas 1.0 THz was blurry by comparison. The 1.5 THz image even provided a better distinction of the regions of the tissue than the time domain image in this case, though there was some added grainy noise in the image.

Comparison across the different slides in the sample in Fig. 2.15 showed that the differentiation of the tissue regions was once again consistent across all slides obtained from the patient with the exception of slides #6 or #9. For slide #6 the two thin lines of lower reflection protruding into the tissue corresponded to debris trapped on the slide that scattered the incident signal and prevented proper reflection. Slide #9, on the other hand, was found to be physically

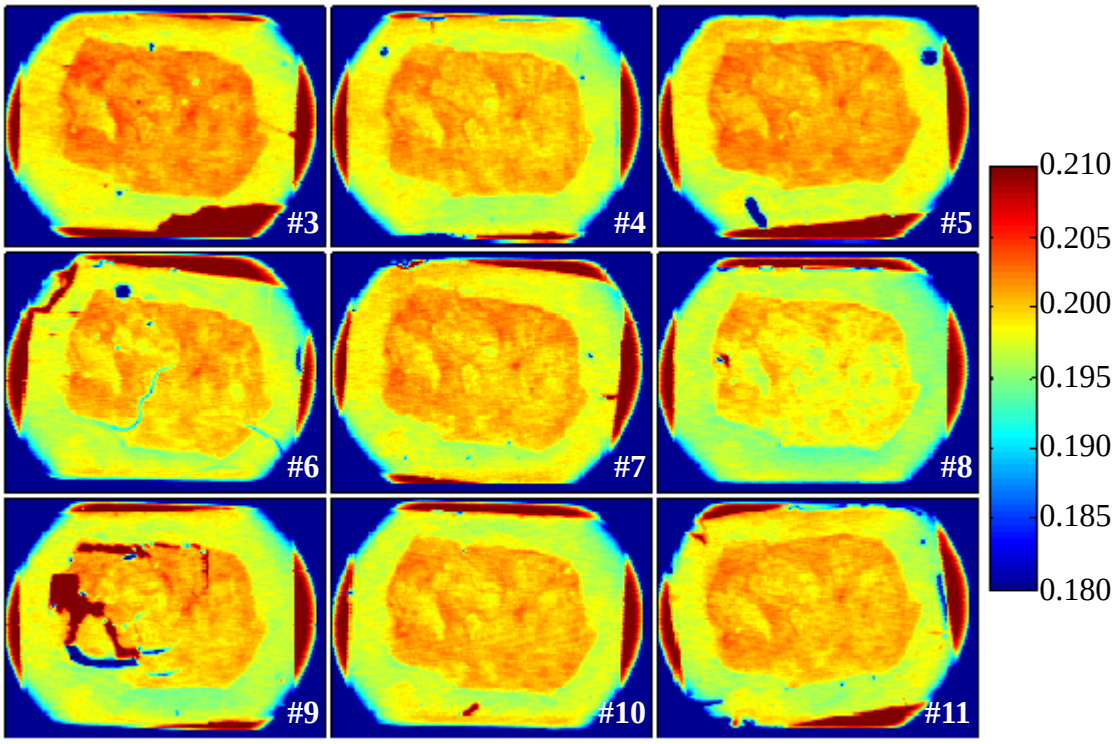

Figure 2.15. Comparison of time domain images of all slides obtained from Sample 1 and normalized to the gold mirror reference.

damaged such that the regions of IDC and fatty tissue could not be distinguished. However, for the remaining slides the distinction of the cancerous tissue regions from the fibroglandular and fatty tissue was consistent.

Sample 1: Comparison of High Power Histopathology

As mentioned previously, the areas of Fig. 2.14(c) denoted by gray rectangles were of particular interest for high resolution imaging since high power pathology images were available for these locations and due to the inclusion of different tissue regions. Thus these regions were subjected to THz imaging using a 50 μm step size instead of the 200 μm step size used in the typical imaging. The resulting time domain images were compared to the high power pathology in Fig. 2.16 with numerals I and II referring to the corresponding region in Fig. 2.14(c). For this comparison the color ranges of the THz images were set to more strongly resemble the high power pathology colors, with darker purple indicating a higher reflection. The high power pathology obtained from the pathology assessment had a much better resolution than the THz scan due to being an optical photograph. This is an inherent limitation of the system dude to THz having a much longer wavelength than optical light. However, the purpose of comparison was to show that the THz imaging could distinguish the same general regions of tissue as the pathology without the need for staining.

Region I covered areas of IDC, fibroglandular, and fatty tissue as denoted in the pathology image of Fig. 2.16(a), and these regions were correlated in the THz pathology image in Fig. 2.16(c). As with the 200 μm image, the highest reflection corresponded to the region of IDC, with lower values for fibroglandular and fatty tissue. Region II included a small region of what was diagnosed by pathology as lymphoid aggregate, with a small core of infiltrating ductal carcinoma. This could be seen in Fig. 2.16(b) as the region of dark purple pathology staining

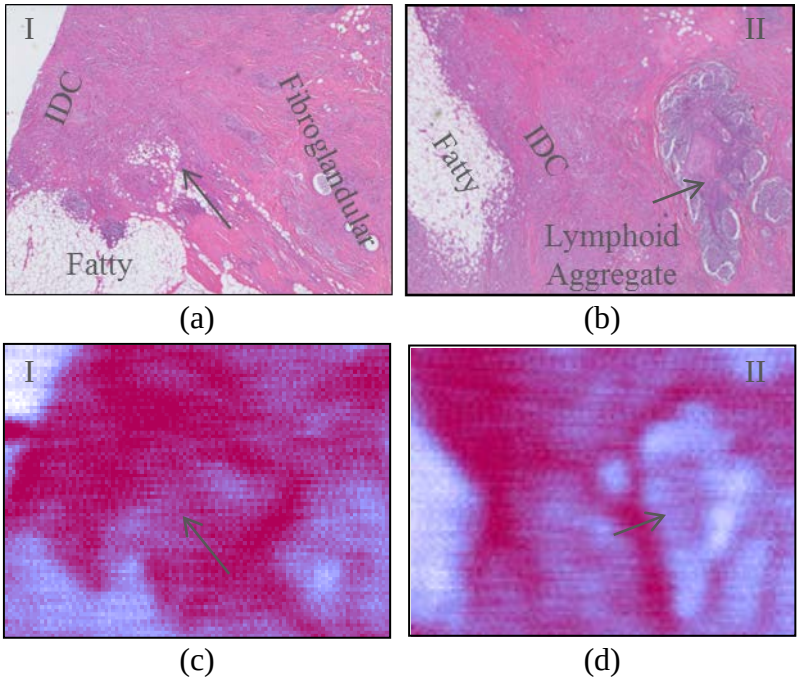

Figure 2.16. Comparison of high power pathology images to high resolution THz for Sample 1, slide #3. (a) High power pathology of region I and (b) region II, and 50 μm step size THz images for (c) region I and (d) region II of Fig. 3.12b.

with the pink core indicating the IDC. This region could also be seen in the THz scan in Fig. 2.16(d), where the lymphoid aggregate showed very little reflection while the IDC in the center showed a higher reflection. In this case the reflection was not necessarily as high as the IDC regions not located within the aggregate. While this sample area was small and there were not enough samples with similar tissue to draw a conclusion from the lymphoid aggregate, it did show the potential for very small feature imaging with the THz system.

Sample 1: Frequency Domain Comparison

In addition to the 1.0, 1.5, and 2.0 THz images obtained for each sample, a wider range of frequency values were investigated for slide #3 of the 40 year old patient with two normalization methods in order to determine what kind of specific effects could be seen over the frequency range. Fig. 2.17 shows the first set of images that had been normalized against the maximum reflection from the background glass. Fig. 2.18 shows the same set of images but with

normalization against an average of ten points taken from the paraffin surrounding the tissue. In each case the selection of the normalization signal was made in order to establish whether or not the properties of the tissue were linear with respect to the reflection of the glass surface (Fig. 2.17) or the paraffin embedding medium (Fig. 2.18).

The comparison in Fig. 2.17 showed that the reflection of the tissue and the paraffin both decrease with increasing frequency compared to the reflection on the slide. This was not surprising, as the reflected signal measured from the tissue included reflections from both the surface of the tissue and from the interface between the tissue and the glass. Attenuation generally increases with increasing frequency, so the contribution of the reflection from between the tissue and glass should decrease at higher frequencies. From the comparison in Fig. 2.18 it

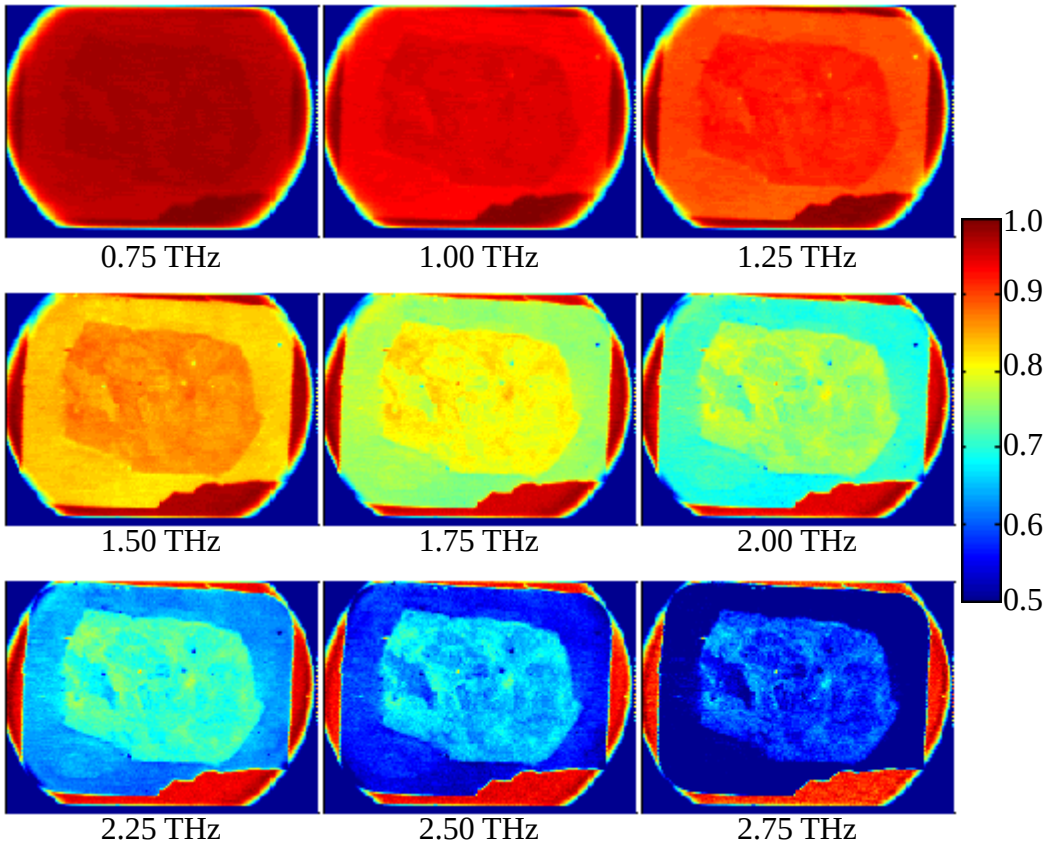

Figure 2.17. Frequency domain images from Sample 1, slide #3 obtained from the magnitude at each frequency normalized to the magnitude of the glass reference.

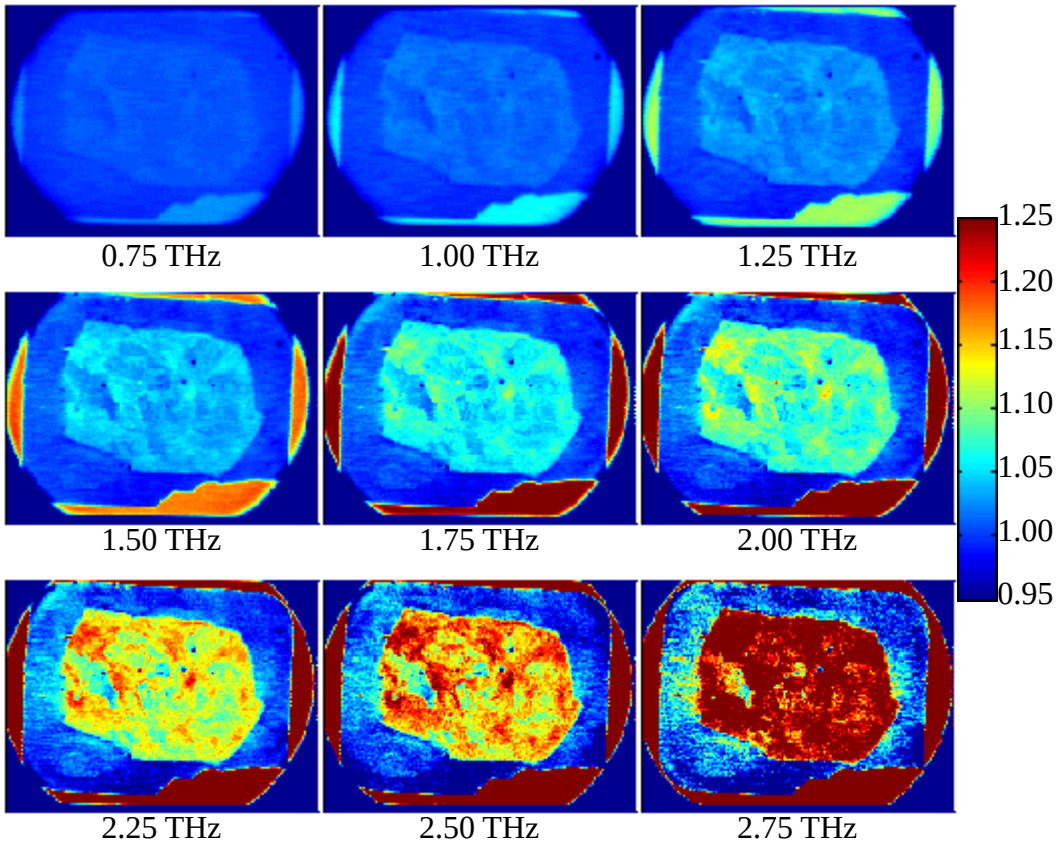

Figure 2.18. Frequency domain images from Sample 1, slide #3 obtained from the magnitude at each frequency normalized to the magnitude of the surrounding paraffin.

could be seen that the reflection in the tissue was not linear compared to the paraffin embedding material surrounding the section. This comparison was significant because it indicated that the properties of the tissue were independent of the embedding medium and thus inherent to the different tissue regions. This observation supported the knowledge that there was some unique property in the tissue that affects the optical properties of the reflection, rather than the reflection being from the surface alone or fully dependent on the paraffin absorbed into the tissue.

Sample 2: Comparison of THz Imaging to Pathology

The results of the imaging of slide #3 from sample 2 are shown in Fig 2.19, and the comparison of the different slides in the sample is presented in Fig. 2.20. It could be seen from the imaging comparison that the time domain image in Fig. 2.19(c) showed some distinction

between the regions of IDC and fibroglandular tissue denoted in the histopathology. However, the difference between the regions was small in the time domain. Additionally for this case in particular the two main regions of tissue on the slide could be distinguished visually from the

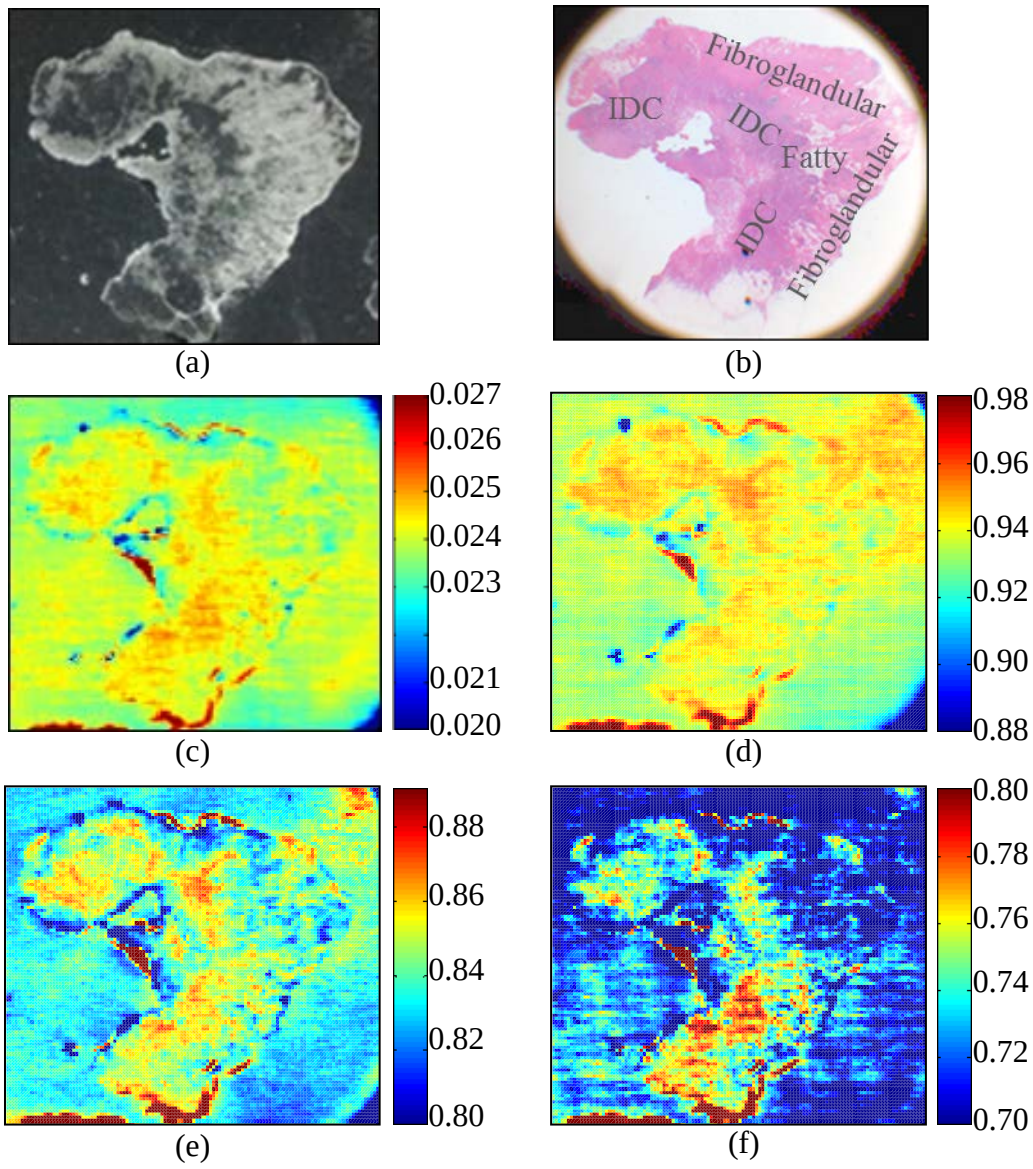

Figure 2.19. Comparison of results for slide 3 of Sample 2: 46 year old Caucasian woman diagnosed with infiltrating ductal carcinoma (IDC). (a) Photographic image of the tissue on glass slide. (b) Low power pathology image used for correlation. (c) THz time domain image of the sample. Frequency domain images at (d) 1.0 THz, (e) 1.5 THz, and (f) 2.0 THz. Frequency domain images are normalized to the maximum reflection of the surrounding glass at that frequency.

FFPE slide shown in Fig. 2.19(a). Even if the distinction between IDC and fibroglandular was not particularly wide for the THz time domain image, it could still be seen that the reflected signal was highest in the areas denoted as IDC while the fibroglandular region was closer to the lower reflection of the surrounding paraffin.

Comparison of the frequency domain images normalized against the reflection from the glass slide showed the same trend as with the 40 year old patient of Sample 1 in that increasing the frequency increased the resolution but also led to noise being introduced to the image. Once again the 1.5 THz image provided a good balance of feature resolution and accuracy in denoting the resulting magnitude plot. Unlike in the 40 year old patient, for this sample the 2.0 THz began to lose accuracy in denoting the different tissue regions and had a far more noise. Around the outermost edge of the tissue there were some regions of particularly high reflection seen. Rather

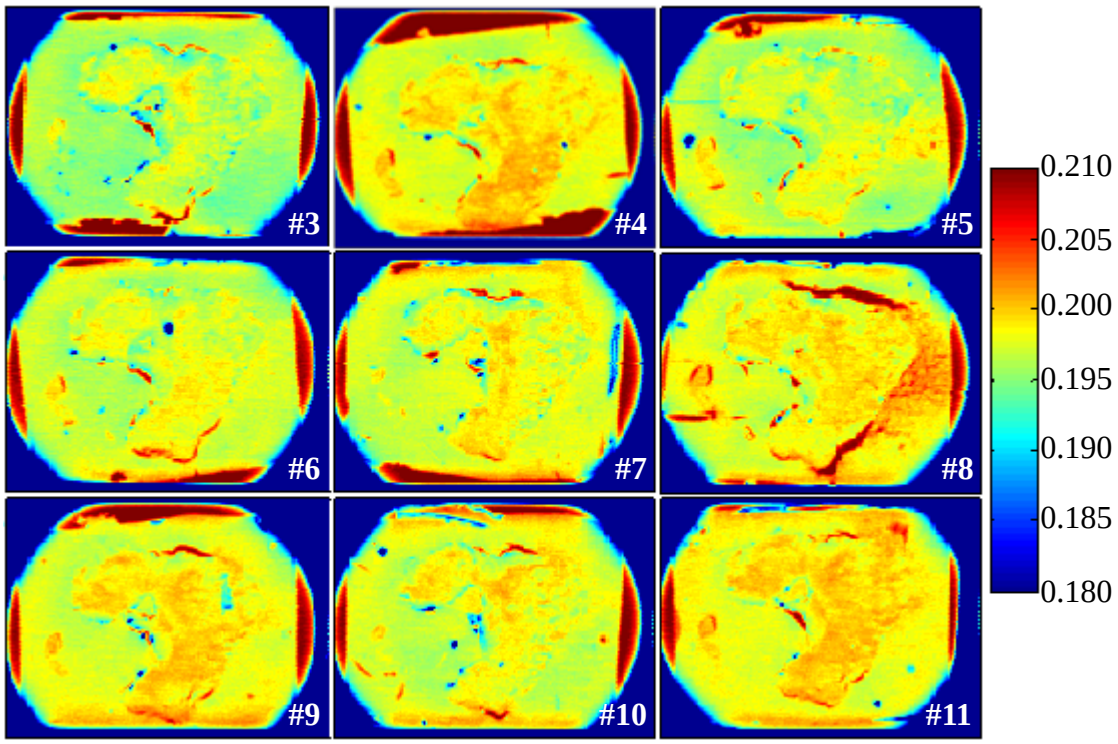

Figure 2.20. Comparison of time domain images of all slides obtained from 46 year old patient and normalized to the gold mirror reference.

than being reflection of the tissue, these locations were separations between the tissue and surrounding paraffin where the glass slide reflection was seen. This separation is also visible in the photograph of the physical FFPE tissue in Fig. 2.19(a).

The comparison of the other slides from the same sample in Fig. 2.20 showed a similar result, where the highest reflection areas were consistent across all nine slides. Due to the tissue section prepared on each slide being very thin it was reasonable to assume that variation of each tissue region across the nine slides was minimal. As such the distinction between the IDC and fibroglandular regions was consistent not only in different images obtained from the same scan but also across all of the tissue sections measured from the same sample.

Sample 3: Comparison of THz Imaging to Pathology

The results of slide #3 from the 22 year old patient are given in Fig. 2.21, and the comparison of the other slides from the same sample is given in Fig. 2.22. In this sample the tissue regions defined by histopathology were IDC, fibroglandular, and DCIS as depicted in Fig. 2.21(b). As with the other samples the different regions of the tissue were clearly differentiated in the time domain image shown in Fig. 2.21(c). Unlike the imaging obtained from the first two samples the highest reflection values were found to correspond to the fibroglandular tissue rather than the IDC tissue. The reason for this discrepancy is not currently known, however it may have been due to some morphological difference due to the tissue sample coming from a particularly young patient. Regardless of the cause, the fibroglandular tissue the DCIS region in this sample was shown to have the lowest reflections in the regions denoted by histopathology. As in the previous samples, the 1.5 THz image gave a good balance of resolution and accuracy when distinguishing the tissue regions. The 1.0 THz image had slightly less resolution and the 2.0 THz image began to lose accuracy to noise, especially in the area denoted as IDC. Additionally the

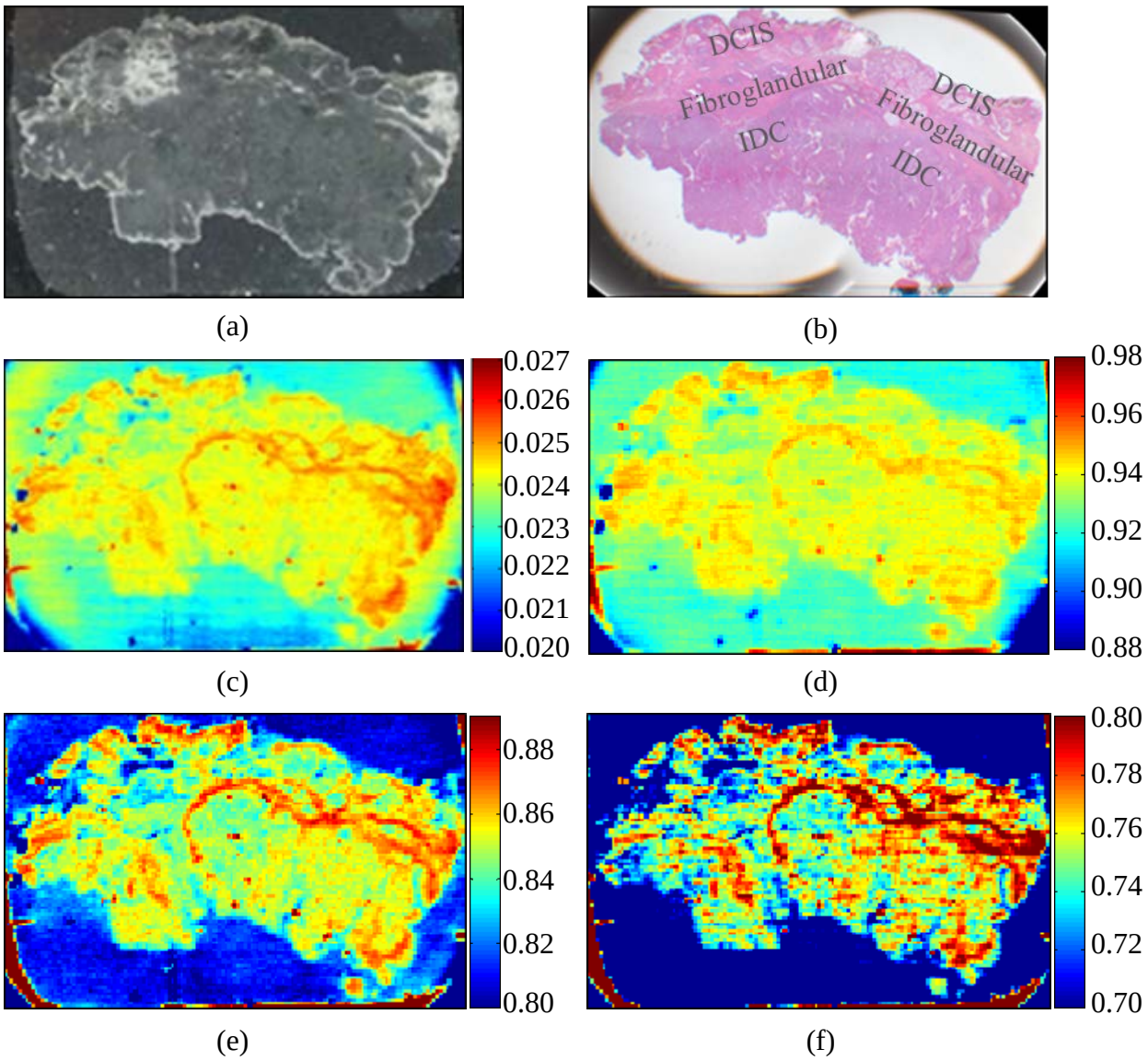

Figure 2.21. Comparison of results for 22-year old Caucasian woman diagnosed with infiltrating ductal carcinoma (IDC). (a) Photographic image of the tissue on glass slide. (b) Low power pathology image used for correlation. (c) THz time domain image of the sample. Frequency domain images at (d) 1.0 THz, (e) 1.5 THz, and (f) 2.0 THz. Frequency domain images are normalized to the maximum reflection of the surrounding glass at that frequency.

fibroglandular tissue showed the highest reflection across all frequencies, so the results of the single scan were consistent with themselves though not necessarily with the other two samples.

The comparison of the results across the different slides in the sample in Fig. 2.22 confirmed the correlation of the reflection characteristics. The fibroglandular tissue once again

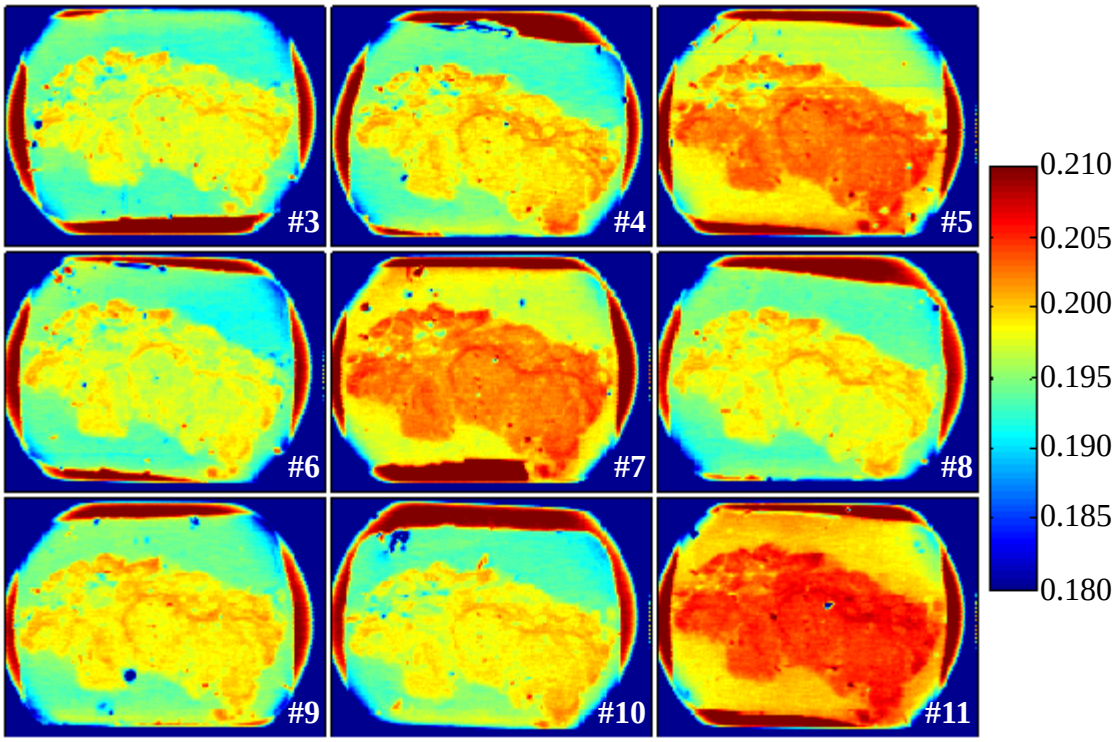

Figure 2.22. Comparison of time domain images of all slides obtained from 22 year old patient and normalized to the gold mirror reference.

gave the highest reflection followed by IDC, and DCIS gave the lowest reflection. There was a noticeable shift in the values of slides #5, #7, and #11 compared to the rest of the images, but this was just a small increase in overall values in the normalization due to a slight discrepancy in the reference signal peak in those scans. However, the key aspect of all of the images was that the results were consistent with the results for slide #3. This indicated that the discrepancy of which region provided maximum reflection compared to the other two samples was due to some property of the entire sample obtained from the 22 year old patient and not a feature of slide #3 alone. Thus any quality that was causing the inversion of the characteristic reflections of the IDC and fibroglandular tissue was a property of the sample as a whole.

F. Discussion of Reflection Mode Imaging

Within this chapter, the formulation for characterizing the measured signals obtained using the reflection imaging module was developed and tested against the spectroscopy data obtained in Chapter 3. This validation indicated that the calculations for reflection using spectroscopy results were in agreement with the measured reflection. This in turn implied strong agreement between the two different methods for analyzing the tissue.

As a part of the imaging approach of this work, several basic signal processes were explored in order to determine the best method for obtaining and displaying meaningful THz images. It was found that the use of deconvolution helped to reduce the noise levels in the resulting image, but normalization of the image against a reference signal allowed for proper comparison for a range of different slides or for the same slide across several days. As such the comparison of several slides across the same sample was performed with normalization to the gold mirror reference. It was found that for each sample all of the slides showed the same regions of tissue under THz imaging.

Comparison of a single slide from each sample set to the histopathology in both the time domain and frequency domain yielded noticeable distinction between tissue regions. These results implied a good potential for THz imaging for distinguishing breast cancer tumors from surrounding normal tissue. It should be noted, however, that the differentiation between the tissues was fairly small compared to the values of the reflected signal. This was largely due to how thin the tissue section on the slide was. Thus there was very little distance over which the tissue was able to affect in the values of the electromagnetic signal. Additionally, the small thickness of the tissue caused the measured reflection signal from the surface of the tissue to be combined with the reflected pulse from the glass behind the tissue. This further reduced the

observable effect of the tissue on the measured reflection signal at each point. However, the distinction was still clear enough to enable some conclusions.

For Samples 1 and 2, the imaging results showed a good consistency in that the regions denoted as IDC were found to have higher reflections than the fibroglandular or fatty regions of the tissue, and that the fatty tissue was the least reflective for these samples. However, for Sample 3 the reflection of the images was reversed. The fibroglandular tissue was found to have the highest reflection of the three tissues in all slides of this sample. The cause for this shift in the values may have been due to some morphological difference in the tissue due to the sample coming from a younger woman. The tissue obtained from this age range was more likely to have denser breast tissue, which could have caused some differences in the comparison of the tissue regions. However, it was not possible to say what properties of the tissue caused the different reflection effects from the other two samples without more samples to examine from this age range. In order to determine whether this effect is common in tissue obtained from younger patients or unique to the sample used in this work, a wider range of samples from younger patients would have to be obtained and analyzed.

In the case of all samples being imaged, isolating the reflected field at 1.5 THz provided an image with improved contrast as well as sufficient resolution for viewing the features of the image at a 200 μm step size. Additional investigation into the imaging of the 40 year old patient demonstrated that a much higher resolution was attainable by reducing the step size of the scan to 50 μm, but this approach was not practical for the size of the tissues in this research. Additionally, a more thorough investigation of the reflected signal across the frequency range of this sample found that the properties of the FFPE tissue are linearly independent of the reflection from the glass slide and the paraffin. This was an important distinction to make, as it indicated

that the tissue held some inherent differentiation in this range that was not dependent on the back reflection or the FFPE content of the different regions. Such information agreed with cancerous and normal tissues having distinct properties in the THz range as asserted in the literature.

In summary, THz imaging has shown capabilities to successfully obtain images of FFPE breast cancer tissue mounted on glass slides and to differentiate between regions of infiltrating ductal carcinoma and non-cancerous tissue in all three samples. However the relative reflections strengths between IDC and fibroglandular tissue were inverted in the case of the 22 year old patient compared to the two older patients. The reflection values from the imaging also showed good correlation to the calculated reflections from spectroscopy of the samples.

III. Spectroscopic Characterization of Breast Cancer Tissue

A. Formulation of a Single Dielectric Layer

One of the primary objectives of this work was to develop the equations needed to obtain the dielectric properties of a material using spectroscopy. A common method for obtaining these values is to compare the measured transmitted signal through a sample to the electromagnetic equations for the same transmitted signal. The simplest setup for this calculation is in the case of a single dielectric layer in air, as demonstrated in Fig. 3.1.

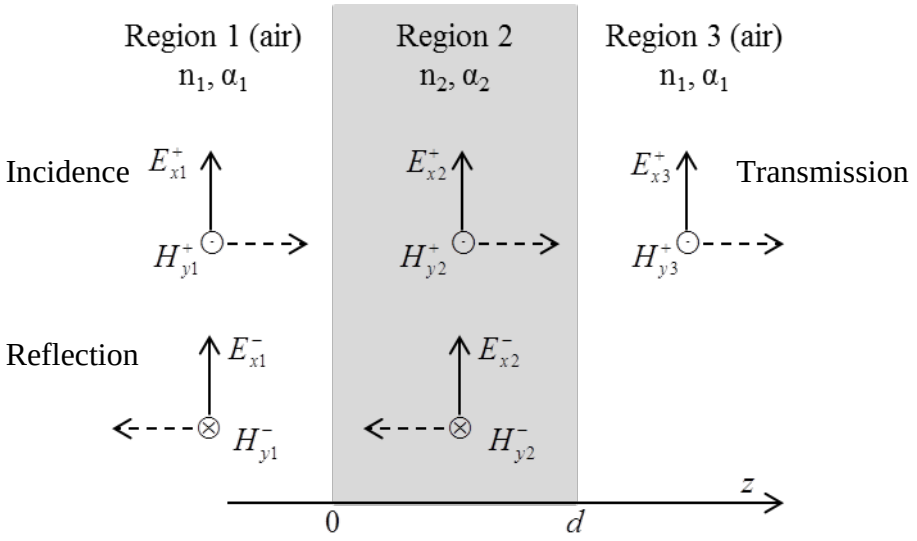

Figure 3.1. Wave propagation through single dielectric layer

In this setup, E_{x1}^{+} is designated as the incident electric field and E_{x3}^{+} is the transmitted field that is measured at the receiver. In order to solve for the transmitted field in terms of the incident field, it is necessary to calculate the total field at each boundary. The solution then follows the steps presented in [61]. The total fields in each region are first expressed in terms of their propagation in the *z*-direction.

$$E_{x1}(z) = E_{x1}^{+}e^{-\gamma_1 z} + E_{x1}^{-}e^{\gamma_1 z} \tag{3-1}$$

$$H_{y1}(z) = \frac{E_{x1}^{+}}{\tilde{\eta}_1} e^{-\gamma_1 z} - \frac{E_{x1}^{-}}{\tilde{\eta}_1} e^{\gamma_1 z} \tag{3-2}$$

$$E_{x2}(z) = E_{x2}^{+} e^{-\gamma_2 z} + E_{x2}^{-} e^{\gamma_2 z} \tag{3-3}$$

$$H_{y2}(z) = \frac{E_{x2}^{+}}{\tilde{\eta}_2} e^{-\gamma_2 z} - \frac{E_{x2}^{-}}{\tilde{\eta}_2} e^{\gamma_2 z} \tag{3-4}$$

$$E_{x3}(z) = E_{x3}^{+} e^{-\gamma_3 z} \tag{3-5}$$

$$H_{y3}(z) = \frac{E_{x3}^{+}}{\tilde{\eta}_3} e^{-\gamma_3 z} \tag{3-6}$$

Once again γ is the propagation constant and η is the intrinsic impedance of the region:

$$\gamma = j\omega\sqrt{\mu_0 \varepsilon_0 \tilde{\varepsilon}_r} = j\frac{\omega}{c}\tilde{n} = \frac{\alpha_{abs}}{2} + j\frac{\omega}{c} n \text{ cm}^{-1} \tag{3-7}$$

$$\tilde{\eta} = \sqrt{\frac{\mu_0}{\varepsilon_0 \tilde{\varepsilon}_r}} = \frac{\eta_0}{\tilde{n}} \tag{3-8}$$

Where $c = 3\times10^8$ m/s is once again the speed of light in a vacuum and $\eta_0 = 120\pi\ \Omega$ is the total field impedance in a vacuum. Returning to the equations for total field, it is possible to express each term as a function of the wave component propagating in the +*z* direction.

$$E_x(z) = E_x^{+} e^{-\gamma z} + E_x^{-} e^{\gamma z} = E_x^{+} e^{-\gamma z}\left(1 + \frac{E_x^{-}}{E_x^{+}} e^{2\gamma z}\right) = E_x^{+} e^{-\gamma z}\left(1 + \tilde{\Gamma}(z)\right) \tag{3-9}$$

$$\tilde{\Gamma}(z) = \frac{E_x^{-}}{E_x^{+}} e^{2\gamma z} \tag{3-10}$$

Where $\tilde{\Gamma}(z)$ is the reflection coefficient at any point on the *z*-axis in any region where γ is constant. For the setup in Fig. 3.1 where there are boundaries involved, the boundary conditions must be considered in order to relate the reflection coefficients in the different regions. There is no current on the sample so the tangential fields at each boundary are equal to

each other. Furthermore the signal for the spectroscopy system has a normal incidence to the sample and is therefore completely tangential for both electric and magnetic fields.

$$E_{t1} - E_{t2} = 0\,, \quad E_{t1} = E_{t2} \tag{3-11}$$

$$\hat{n} \times (H_1 - H_2) = 0\,, \quad H_{t1} = H_{t2} \tag{3-12}$$

Where $\hat{n}$ is the unit vector normal to the boundary plane. Since both the total electric and total magnetic fields are continuous at the boundary, the ratio between them defined as total wave impedance $\tilde{Z}(z)$ is also continuous and can be used to relate the reflection coefficient across the boundary without the dependence on the electric field magnitude.

$$H_y(z) = \frac{E_x^+}{\tilde{\eta}} e^{-\gamma z} - \frac{E_x^-}{\tilde{\eta}} e^{\gamma z} = \frac{E_x^+}{\tilde{\eta}} e^{-\gamma z}\left(1 - \frac{E_x^-}{E_x^+} e^{2\gamma z}\right) = \frac{E_x^+}{\tilde{\eta}} e^{-\gamma z}\left(1 - \tilde{\Gamma}(z)\right) \tag{3-13}$$

$$\tilde{Z}(z) = \frac{E_x(z)}{H_y(z)} = \tilde{\eta}\frac{1 + \tilde{\Gamma}(z)}{1 - \tilde{\Gamma}(z)} \tag{3-14}$$

$$\tilde{\Gamma}(z) = \frac{\tilde{Z}(z) - \tilde{\eta}}{\tilde{Z}(z) + \tilde{\eta}} \tag{3-15}$$

With these relations it is now possible to solve for the reflection coefficients at each boundary. First the reflection coefficient of region 3 is set to 0 since there is no wave propagating in the –*z* direction. Then equations (3-14) and (3-15) are used to find the reflection coefficient inside the dielectric moving from right to left.

$$\tilde{\Gamma}_3(d) = \frac{E_{x3}^-}{E_{x3}^+} e^{2\gamma_1 d} = 0 \tag{3-16}$$

$$\tilde{Z}_3(d) = \tilde{\eta}_1 \frac{1 + \tilde{\Gamma}_3(d)}{1 - \tilde{\Gamma}_3(d)} = \tilde{\eta}_1 = \frac{\eta_0}{\tilde{n}_1} = \tilde{Z}_2(d) \tag{3-17}$$

$$\tilde{\Gamma}_2(d) = \frac{\tilde{Z}_2(d) - \tilde{\eta}_2}{\tilde{Z}_2(d) + \tilde{\eta}_2} = \frac{\eta_0/\tilde{n}_1 - \eta_0/\tilde{n}_2}{\eta_0/\tilde{n}_1 + \eta_0/\tilde{n}_2} = \frac{\tilde{n}_2 - \tilde{n}_1}{\tilde{n}_2 + \tilde{n}_1} \tag{3-18}$$

The reflection coefficient inside the dielectric is defined by equation (3-10).

$$\tilde{\Gamma}_2(0)=\frac{E_{x2}^-}{E_{x2}^+}e^{2\gamma_2(0)}\ ,\quad \tilde{\Gamma}_2(d)=\frac{E_{x2}^-}{E_{x2}^+}e^{2\gamma_2(d)}\ ,\quad \tilde{\Gamma}_2(0)=\tilde{\Gamma}_2(d)e^{-2\gamma_2 d} \tag{3-19}$$

$$\tilde{Z}_2(0)=\tilde{\eta}_2\frac{1+\tilde{\Gamma}_2(0)}{1-\tilde{\Gamma}_2(0)}=\frac{\eta_0}{\tilde{n}_2}\frac{1+\tilde{\Gamma}_2(d)e^{-2\gamma_2 d}}{1-\tilde{\Gamma}_2(d)e^{-2\gamma_2 d}}=\tilde{Z}_1(0) \tag{3-20}$$

$$\tilde{\Gamma}_1(0)=\frac{\tilde{Z}_1(0)-\tilde{\eta}_1}{\tilde{Z}_1(0)+\tilde{\eta}_1}=\frac{\frac{1}{\tilde{n}_2}\frac{1+\tilde{\Gamma}_2(d)e^{-2\gamma_2 d}}{1-\tilde{\Gamma}_2(d)e^{-2\gamma_2 d}}-\frac{1}{\tilde{n}_1}}{\frac{1}{\tilde{n}_2}\frac{1+\tilde{\Gamma}_2(d)e^{-2\gamma_2 d}}{1-\tilde{\Gamma}_2(d)e^{-2\gamma_2 d}}+\frac{1}{\tilde{n}_1}} \tag{3-21}$$

The relation above can be rewritten in the following form:

$$\tilde{\Gamma}_1(0)=\frac{\left(\tilde{n}_1-\tilde{n}_2\right)+\left(\tilde{n}_2+\tilde{n}_1\right)\tilde{\Gamma}_2(d)e^{-2\gamma_2 d}}{\left(\tilde{n}_2+\tilde{n}_1\right)+\left(\tilde{n}_1-\tilde{n}_2\right)\tilde{\Gamma}_2(d)e^{-2\gamma_2 d}}=\frac{\frac{\tilde{n}_1-\tilde{n}_2}{\tilde{n}_2+\tilde{n}_1}+\tilde{\Gamma}_2(d)e^{-2\gamma_2 d}}{1+\frac{\tilde{n}_1-\tilde{n}_2}{\tilde{n}_2+\tilde{n}_1}\tilde{\Gamma}_2(d)e^{-2\gamma_2 d}} \tag{3-22}$$

This expression of the reflection coefficient is consistent with the equation for the reflection coefficient of a single dielectric layer in air in [60] as well as the recursive relationship for reflection coefficients in multiple layered media at normal incidence in [62]. With these equations it is then possible to find the expression for E_{x3} in terms of the incident field using the boundary condition (3-11) between each of the regions in Fig. 3.1.

$$E_{x3}(d)=E_{x2}^+(d)+E_{x2}^-(d)=E_{x2}^+(d)\left(1+\tilde{\Gamma}_2(d)\right)=E_{x2}^+(d)\frac{2\tilde{n}_2}{\tilde{n}_2+\tilde{n}_1} \tag{3-23}$$

$$E_{x2}^+(d)=E_{x2}^+(0)\,\mathrm{e}^{-\gamma_2 d} \tag{3-24}$$

Applying the boundary conditions at $z=0$,

$$E_{x2}^+(0)+E_{x2}^-(0)=E_{x1}^+(0)+E_{x1}^-(0) \tag{3-25}$$

$$E_{x2}^+(0)\left(1+\tilde{\Gamma}_2(0)\right)=E_{x1}^+(0)\left(1+\tilde{\Gamma}_1(0)\right) \tag{3-26}$$

$$E_{x2}^{+}(0) = E_{x1}^{+}(0)\left[\left(1+\tilde{\Gamma}_1(0)\right)\Big/\left(1+\tilde{\Gamma}_2(0)\right)\right] \tag{3-27}$$

$$\left(1+\tilde{\Gamma}_2(0)\right) = 1+\tilde{\Gamma}_2(d)e^{-2\gamma_2 d} \tag{3-28}$$

$$\left(1+\tilde{\Gamma}_1(0)\right) = 1+\frac{\frac{1}{\tilde{n}_2}\frac{1+\tilde{\Gamma}_2(d)e^{-2\gamma_2 d}}{1-\tilde{\Gamma}_2(d)e^{-2\gamma_2 d}}-\frac{1}{\tilde{n}_1}}{\frac{1}{\tilde{n}_2}\frac{1+\tilde{\Gamma}_2(d)e^{-2\gamma_2 d}}{1-\tilde{\Gamma}_2(d)e^{-2\gamma_2 d}}+\frac{1}{\tilde{n}_1}} = \frac{\frac{2}{\tilde{n}_2}\frac{1+\tilde{\Gamma}_2(d)e^{-2\gamma_2 d}}{1-\tilde{\Gamma}_2(d)e^{-2\gamma_2 d}}}{\frac{1}{\tilde{n}_2}\frac{1+\tilde{\Gamma}_2(d)e^{-2\gamma_2 d}}{1-\tilde{\Gamma}_2(d)e^{-2\gamma_2 d}}+\frac{1}{\tilde{n}_1}} \tag{3-29}$$

$$\frac{\left(1+\tilde{\Gamma}_1(0)\right)}{\left(1+\tilde{\Gamma}_2(0)\right)} = \frac{\frac{2}{\tilde{n}_2}\frac{1}{1-\tilde{\Gamma}_2(d)e^{-2\gamma_2 d}}}{\frac{1}{\tilde{n}_2}\frac{1+\tilde{\Gamma}_2(d)e^{-2\gamma_2 d}}{1-\tilde{\Gamma}_2(d)e^{-2\gamma_2 d}}+\frac{1}{\tilde{n}_1}} = \frac{2}{\left(1+\tilde{\Gamma}_2(d)e^{-2\gamma_2 d}\right)+\left(\tilde{n}_2/\tilde{n}_1\right)\left(1-\tilde{\Gamma}_2(d)e^{-2\gamma_2 d}\right)} \tag{3-30}$$

$$\frac{\left(1+\tilde{\Gamma}_1(0)\right)}{\left(1+\tilde{\Gamma}_2(0)\right)} = \frac{2}{\frac{\tilde{n}_1+\tilde{n}_2}{\tilde{n}_1}+\frac{\tilde{n}_1-\tilde{n}_2}{\tilde{n}_1}\tilde{\Gamma}_2(d)e^{-2\gamma_2 d}} = \frac{2\tilde{n}_1}{\tilde{n}_1+\tilde{n}_2}\frac{1}{1+\frac{\tilde{n}_1-\tilde{n}_2}{\tilde{n}_1+\tilde{n}_2}\tilde{\Gamma}_2(d)e^{-2\gamma_2 d}} \tag{3-31}$$

Thus the final expression for the transmitted field in (3-23) becomes:

$$E_{x3}(d) = \left(\frac{2\tilde{n}_2}{\tilde{n}_2+\tilde{n}_1}\right)\left(\frac{2\tilde{n}_1}{\tilde{n}_1+\tilde{n}_2}\right)\frac{1}{\left(1+\frac{\tilde{n}_1-\tilde{n}_2}{\tilde{n}_1+\tilde{n}_2}\tilde{\Gamma}_2(d)e^{-2\gamma_2 d}\right)}\mathrm{e}^{-\gamma_2 d}\ E_{x1}^{+}(0) = E_{sample} \tag{3-32}$$

The first two terms of the right-hand side of this expression are recognizable as the transmission coefficients at each of the boundaries in Fig. 3.1., and the exponential term is the phase shift and attenuation through region 2. The third term describes the contribution of multiple reflections between the two boundaries of region 2 and can be alternatively written as a power series:

$$\frac{1}{\left(1+\frac{\tilde{n}_1-\tilde{n}_2}{\tilde{n}_1+\tilde{n}_2}\tilde{\Gamma}_2(d)e^{-2\gamma_2 d}\right)} = \sum_{m=0}^{\infty}\left(\frac{\tilde{n}_2-\tilde{n}_1}{\tilde{n}_1+\tilde{n}_2}\tilde{\Gamma}_2(d)e^{-2\gamma_2 d}\right)^m \tag{3-33}$$

In this form it is more clearly seen that the term is a summation of the signal reflecting from both boundaries of region 2 as well as the phase change and attenuation from passing through the dielectric in both directions. The power series expression of the transmission corresponds with the transmission equation presented in [63], while equation (3-32) corresponds to the equations for a single dielectric layer in [60].

It was not possible to solve equation (3-32) directly due to the fact that the incident field at $z = 0$ was not known. Instead, the equation had to be compared to a reference in order to remove the dependence of the transmitted field on the incident at the first boundary. For a single dielectric layer the most efficient reference is the transmitted signal through air. There is no reflection in this case, so the transmitted signal on the right side of the right boundary is simply a phase shift of the incident through air across the distance between the two boundaries. Denoting the transmission equation (3-32) as E_{sample} and the signal transmitted through air as E_{ref}, the following comparison is obtained:

$$E_{ref} = E_{x1}^{+}(0)\,\mathrm{e}^{-\gamma_1 d} \tag{3-34}$$

$$\frac{E_{sample}}{E_{ref}} = \left(\frac{2\tilde{n}_2}{\tilde{n}_2 + \tilde{n}_1}\right)\left(\frac{2\tilde{n}_1}{\tilde{n}_1 + \tilde{n}_2}\right)\frac{1}{\left(1 + \frac{\tilde{n}_1 - \tilde{n}_2}{\tilde{n}_1 + \tilde{n}_2}\tilde{\Gamma}_2(d)e^{-2\gamma_2 d}\right)}\mathrm{e}^{(\gamma_1 - \gamma_2)d} \tag{3-35}$$

This equation can then be compared to the measured E_{sample} and E_{ref} obtained from the THz system. In this comparison, the desired properties of the refractive index n and absorption coefficient α_{abs} can be solved for numerically by minimizing the difference between the magnitude and phase of equation (3-35) and the measured signals. The magnitude and phase can be separated by taking the natural logarithm on both sides.

$$\text{Let } \tilde{\tau} = \left(\frac{2\tilde{n}_2}{\tilde{n}_2 + \tilde{n}_1}\right)\left(\frac{2\tilde{n}_1}{\tilde{n}_1 + \tilde{n}_2}\right)\frac{1}{\left(1 + \frac{\tilde{n}_1 - \tilde{n}_2}{\tilde{n}_1 + \tilde{n}_2}\tilde{\Gamma}_2(d)e^{-2\gamma_2 d}\right)} \tag{3-36}$$

$$\ln\left(\left|\frac{E_{sample}}{E_{ref}}\right|\right) + j\arg\left(\frac{E_{sample}}{E_{ref}}\right) = \ln\left(\tilde{\tau}\right) + \left(\gamma_1 - \gamma_2\right)d \tag{3-37}$$

Then using the definition of γ given in equation (2-19):

$$\arg\left(\frac{E_{sample}}{E_{ref}}\right) = \Im\left\{\ln\left(\tilde{\tau}\right)\right\} + \frac{\omega}{c}\left(n_1 - n_2\right)d \tag{3-38}$$

$$\ln\left(\left|\frac{E_{sample}}{E_{ref}}\right|\right) = \Re\left\{\ln\left(\tilde{\tau}\right)\right\} + \left(\alpha_{abs,1} - \alpha_{abs,2}\right)\frac{d}{2} \tag{3-39}$$

In order to obtain the numerical solution to the right hand side of equations (3-38) and (3-39), the theoretical values are compared against the measurements obtained from the pulsed THz system. This can be expressed as a set of error functions for the phase (err_{phase}) and the magnitude ($err_{magnitude}$), with the total error of the system expressed by err_{total}.

$$err_{phase} = \left[\arg\left(\frac{E_{sample}}{E_{ref}}\right)_{meas} - \arg\left(\frac{E_{sample}}{E_{ref}}\right)_{theoretical}\right] \tag{3-40}$$

$$\boxed{err_{phase} = \left[\arg\left(\frac{E_{sample}}{E_{ref}}\right)_{meas}\right] - \left[\Im\left\{\ln\left(\tilde{\tau}\right)\right\} + \frac{\omega}{c}\left(n_1 - n_2\right)d\right]} \tag{3-41}$$

$$err_{magnitude} = \left[\ln\left(\left|\frac{E_{sample}}{E_{ref}}\right|\right)_{meas} - \ln\left(\left|\frac{E_{sample}}{E_{ref}}\right|\right)_{theoretical}\right] \tag{3-42}$$

$$\boxed{err_{magnitude} = \left[\ln\left(\left|\frac{E_{sample}}{E_{ref}}\right|\right)_{meas}\right] - \left[\Re\left\{\ln\left(\tilde{\tau}\right)\right\} + \left(\alpha_{abs,1} - \alpha_{abs,2}\right)\frac{d}{2}\right]} \tag{3-43}$$

$$err_{total} = \sqrt{err_{phase}^2 + err_{magnitude}^2} \tag{3-44}$$

Where $\left(E_{sample}/E_{ref}\right)_{meas}$ is the measurement data taken from the system. In order to find the best solution to the total error, a range of values for of n_2 and $\alpha_{abs,2}$ are input into equations (3-41) and (3-43) in order to find the solution with the lowest err_{total}. Since there is a contribution of both refractive index and absorption coefficient in equation (3-36), equations (3-41) and (3-43) cannot just be minimized individually. Instead values of n_2 and $\alpha_{abs,2}$ are selected to minimize the combined error of both functions in equation (3-44). The MATLAB code for finding the dielectric properties of the glass is given in Appendix A.

Linear Solution: Single Dielectric

In addition to the solution found numerically by reducing the error function, a linear solution to (3-35) can be approximated if two assumptions are made. This is the process used by the TPS Spectra 3000 solver to find the dielectric properties of the material. The first assumption would be that the multiple reflections inside the dielectric do not contribute to the transmitted signal. This can be assumed only if the refractive index compared to air is very small, the absorption coefficient of the glass is large, or the thickness of the glass is thick compared to the wavelength.

$$\frac{\tilde{n}_1 - \tilde{n}_2}{\tilde{n}_1 + \tilde{n}_2}\tilde{\Gamma}_2(d)e^{-2\gamma_2 d} \Rightarrow 0\,, \quad \frac{1}{\left(1 + \frac{\tilde{n}_1 - \tilde{n}_2}{\tilde{n}_1 + \tilde{n}_2}\tilde{\Gamma}_2(d)e^{-2\gamma_2 d}\right)} \Rightarrow 1 \tag{3-45}$$

The second assumption is that the absorption coefficient's contribution to the transmission and reflection coefficients is negligible, such that $\tilde{\tau}$ can be assumed to be real. If both of these assumptions are used, then equations (3-38) and (3-39) simplify to:

$$n_2 = -\frac{c}{\omega d}\arg\left(\frac{E_{sample}}{E_{ref}}\right) + n_1 \tag{3-46}$$

$$\alpha_{abs,2} = \frac{2}{d}\left[\ln\left(\frac{4n_1 n_2}{(n_1+n_2)^2}\right) - \ln\left(\left|\frac{E_{sample}}{E_{ref}}\right|\right)\right] + \alpha_{abs,1} \tag{3-47}$$

Thus with some approximations the equations can simplify to a linear form since the sample and reference measurements are known values at the time of the solution. The effect of using these approximations will be investigated with the validation of the properties of the glass slide.

B. Formulation of Tissue Layer on Glass Slide

The purpose of the spectroscopy in this research was to characterize the dielectric properties of formalin-fixed, paraffin-embedded (FFPE) breast cancer tissue on glass slides. Thus the solution of a single dielectric layer must be expanded to a solution for the signal passing through glass and the tissue. This setup is shown in Fig. 3.2. Due to the layout of the sample holder inside the THz system, it is necessary to orient the glass and tissue with the tissue

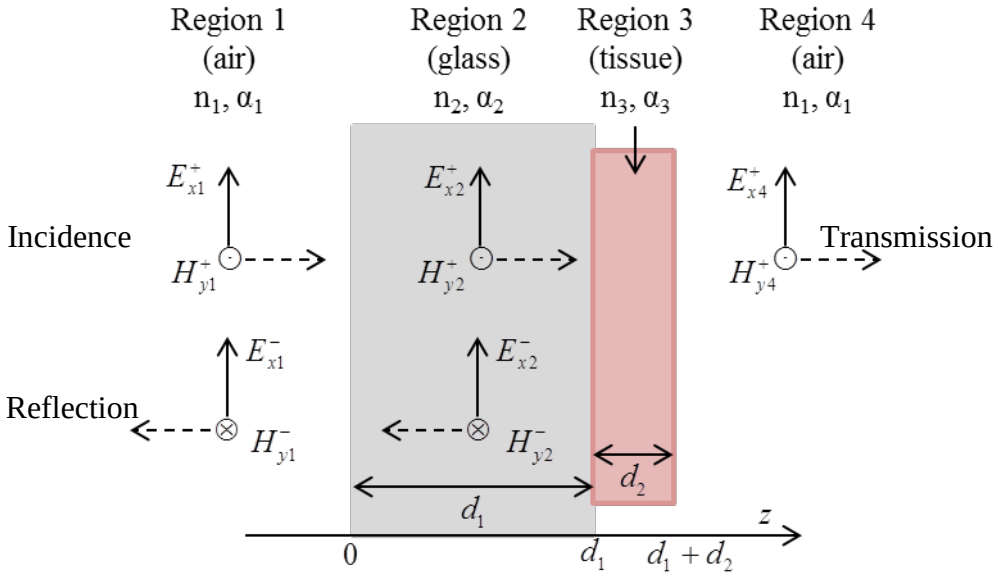

Figure 3.2: Setup for finding properties of tissue on glass

facing away from the incident signal. Thus the signal passes first through the glass before interacting with the tissue.

In this setup, it is assumed that the properties of the glass have already been found via the process given for the single dielectric layer. Then the same process for finding the properties of the single dielectric layer is used for the properties in region 3. Equations (3-23) and (3-31) are used to solve for the reflection coefficients at each boundary moving from right to left.

$$\tilde{\Gamma}_4\left(d_1+d_2\right)=0\,,\quad \tilde{\Gamma}_3\left(d_1+d_2\right)=\frac{\tilde{n}_3-\tilde{n}_1}{\tilde{n}_3+\tilde{n}_1} \tag{3-48}$$

$$\tilde{\Gamma}_3\left(d_1\right)=\tilde{\Gamma}_3(d_1+d_2)e^{-2\gamma_3 d_2}\,,\quad \tilde{\Gamma}_2\left(d_1\right)=\frac{\frac{1}{\tilde{n}_3}\frac{1+\tilde{\Gamma}_3(d_1+d_2)e^{-2\gamma_3 d_2}}{1-\tilde{\Gamma}_3(d_1+d_2)e^{-2\gamma_3 d_2}}-\frac{1}{\tilde{n}_2}}{\frac{1}{\tilde{n}_3}\frac{1+\tilde{\Gamma}_3(d_1+d_2)e^{-2\gamma_3 d_2}}{1-\tilde{\Gamma}_3(d_1+d_2)e^{-2\gamma_3 d_2}}+\frac{1}{\tilde{n}_2}} \tag{3-49}$$

$$\tilde{\Gamma}_2\left(0\right)=\tilde{\Gamma}_2(d_1)e^{-2\gamma_2 d_1}\,,\quad \tilde{\Gamma}_1\left(0\right)=\frac{\frac{1}{\tilde{n}_2}\frac{1+\tilde{\Gamma}_2(d_1)e^{-2\gamma_2 d_1}}{1-\tilde{\Gamma}_2(d_1)e^{-2\gamma_2 d_1}}-\frac{1}{\tilde{n}_1}}{\frac{1}{\tilde{n}_2}\frac{1+\tilde{\Gamma}_2(d_1)e^{-2\gamma_2 d_1}}{1-\tilde{\Gamma}_2(d_1)e^{-2\gamma_2 d_1}}+\frac{1}{\tilde{n}_1}} \tag{3-50}$$

The calculation of the transmitted field then follows the same process starting in equation (3-23) until it can be found in terms of the incident field in region 1.

$$E_{x4}(d_1+d_2)=\left(1+\tilde{\Gamma}_3(d_1+d_2)\right)e^{-\gamma_3 d_2}\left(\frac{1+\tilde{\Gamma}_2(d_1)}{1+\tilde{\Gamma}_3(d_1)}\right)e^{-\gamma_2 d_1}\left(\frac{1+\tilde{\Gamma}_1(0)}{1+\tilde{\Gamma}_2(0)}\right)E_{x1}^{+}(0) \tag{3-51}$$

The ratios of the reflection coefficients simplify in the same form as equation (3-31).

$$E_{x4}(d_1+d_2)=\left(\frac{2\tilde{n}_3}{\tilde{n}_1+\tilde{n}_3}\right)\left(\frac{2\tilde{n}_2}{\tilde{n}_2+\tilde{n}_3}\frac{1}{1+\frac{\tilde{n}_2-\tilde{n}_3}{\tilde{n}_2+\tilde{n}_3}\tilde{\Gamma}_3(d_1+d_2)e^{-2\gamma_3 d_2}}\right)\times \left(\frac{2\tilde{n}_1}{\tilde{n}_1+\tilde{n}_2}\frac{1}{1+\frac{\tilde{n}_1-\tilde{n}_2}{\tilde{n}_1+\tilde{n}_2}\tilde{\Gamma}_2(d_1)e^{-2\gamma_2 d_1}}\right)e^{-\gamma_3 d_2-\gamma_2 d_1}E_{x1}^{+}(0) \tag{3-52}$$

$$E_{x4}(d_1+d_2)=\frac{\left[\frac{8\tilde{n}_1\tilde{n}_2\tilde{n}_3}{\left(\tilde{n}_1+\tilde{n}_2\right)\left(\tilde{n}_2+\tilde{n}_3\right)\left(\tilde{n}_1+\tilde{n}_3\right)}\right]e^{-\gamma_3 d_2-\gamma_2 d_1}E_{x1}^{+}(0)}{\left(1+\frac{\tilde{n}_1-\tilde{n}_2}{\tilde{n}_1+\tilde{n}_2}\tilde{\Gamma}_2(d_1)e^{-2\gamma_2 d_1}\right)\left(1+\frac{\tilde{n}_2-\tilde{n}_3}{\tilde{n}_2+\tilde{n}_3}\tilde{\Gamma}_3(d_1+d_2)e^{-2\gamma_3 d_2}\right)} \tag{3-53}$$

This equation is very similar to the transmission solution found in equation (3-32), but with the added terms for transmission, internal reflection, and phase shift in region 3. Once again the incident field at $z=0$ was not explicitly known, so the measured transmission had to be compared to another measured signal in order to solve for the unknown properties of the tissue. The reference can be taken as either the signal through air with a phase change corresponding to the thickness of the tissue and glass, or it can be obtained as the signal through glass with a phase change corresponding to the thickness of the tissue alone. In the latter case, the reference signal can be obtained from equation (3-32).

$$E_{ref,glass}(d_1+d_2)=\frac{2\tilde{n}_1\tilde{n}_2}{\left(\tilde{n}_2+\tilde{n}_1\right)^2}\frac{1}{\left(1+\frac{\tilde{n}_1-\tilde{n}_2}{\tilde{n}_1+\tilde{n}_2}\frac{\tilde{n}_2-\tilde{n}_1}{\tilde{n}_1+\tilde{n}_2}e^{-2\gamma_2 d_1}\right)}\mathrm{e}^{-\gamma_2 d_1-\gamma_1 d_2}\,E_{x1}^{+}(0) \tag{3-54}$$

Then by taking equation (3-53) to be E_{sample}, the ratio of the two measured signals is calculated in order to remove the dependence on the incident signal.

$$\frac{E_{sample}}{E_{ref}} = \frac{\left[\frac{2\tilde{n}_3\left(\tilde{n}_1+\tilde{n}_2\right)}{\left(\tilde{n}_2+\tilde{n}_3\right)\left(\tilde{n}_1+\tilde{n}_3\right)}\right]\left(1-\left[\frac{\tilde{n}_1-\tilde{n}_2}{\tilde{n}_1+\tilde{n}_2}\right]^2 e^{-2\gamma_2 d_1}\right)}{\left(1+\frac{\tilde{n}_1-\tilde{n}_2}{\tilde{n}_1+\tilde{n}_2}\tilde{\Gamma}_2(d_1)e^{-2\gamma_2 d_1}\right)\left(1+\frac{\tilde{n}_2-\tilde{n}_3}{\tilde{n}_2+\tilde{n}_3}\tilde{\Gamma}_3(d_1+d_2)e^{-2\gamma_3 d_2}\right)} e^{(\gamma_1-\gamma_3)d_2} \tag{3-55}$$

As in the case with the single dielectric, the values for the components of the complex refractive index are found by minimizing the difference in magnitude and phase between the measured signals and equation (3-55). For convenience, all of the transmission terms will again be combined into term $\tilde{\tau}$.

$$\tilde{\tau} = \frac{\left[\frac{2\tilde{n}_3\left(\tilde{n}_1+\tilde{n}_2\right)}{\left(\tilde{n}_2+\tilde{n}_3\right)\left(\tilde{n}_1+\tilde{n}_3\right)}\right]\left(1-\left[\frac{\tilde{n}_1-\tilde{n}_2}{\tilde{n}_1+\tilde{n}_2}\right]^2 e^{-2\gamma_2 d_1}\right)}{\left(1+\frac{\tilde{n}_1-\tilde{n}_2}{\tilde{n}_1+\tilde{n}_2}\tilde{\Gamma}_2(d_1)e^{-2\gamma_2 d_1}\right)\left(1+\frac{\tilde{n}_2-\tilde{n}_3}{\tilde{n}_2+\tilde{n}_3}\tilde{\Gamma}_3(d_1+d_2)e^{-2\gamma_3 d_2}\right)} \tag{3-56}$$

$$\ln\left(\left|\frac{E_{sample}}{E_{ref}}\right|\right) + j\arg\left(\frac{E_{sample}}{E_{ref}}\right) = \ln\left(\tilde{\tau}\right) + \left(\gamma_1-\gamma_3\right)d_2 \tag{3-57}$$

$$\arg\left(\frac{E_{sample}}{E_{ref}}\right) = \Im\left\{\ln\left(\tilde{\tau}\right)\right\} + \frac{\omega}{c}\left(n_1-n_3\right)d_2 \tag{3-58}$$

$$\ln\left(\left|\frac{E_{sample}}{E_{ref}}\right|\right) = \Re\left\{\ln\left(\tilde{\tau}\right)\right\} + \left(\alpha_{abs,1}-\alpha_{abs,3}\right)\frac{d_2}{2} \tag{3-59}$$

As with the single dielectric layer, equations (3-58) and (3-59) are solved numerically by expressing them as the difference in the measured signals and the calculated equations.

$$err_{phase} = \left[\arg\left(\frac{E_{sample}}{E_{ref}}\right)_{meas} - \arg\left(\frac{E_{sample}}{E_{ref}}\right)_{theoretical}\right] \tag{3-60}$$

$$err_{phase,2diel} = \left[\arg\left(\frac{E_{sample}}{E_{ref}}\right)_{meas}\right] - \left[\Im\left\{\ln\left(\tilde{\tau}\right)\right\} + \frac{\omega}{c}\left(n_1-n_3\right)d_2\right] \tag{3-61}$$

$$err_{magnitude} = \left[\ln\left(\left| \frac{E_{sample}}{E_{ref}} \right| \right)_{meas} - \ln\left(\left| \frac{E_{sample}}{E_{ref}} \right| \right)_{theoretical} \right] \tag{3-62}$$

$$\boxed{err_{magnitude,2diel} = \left[\ln\left(\left| \frac{E_{sample}}{E_{ref}} \right| \right)_{meas} \right] - \left[\Re\left\{ \ln\left(\tilde{\tau} \right) \right\} + \left(\alpha_{abs,1} - \alpha_{abs,3} \right) \frac{d_2}{2} \right]} \tag{3-63}$$

$$err_{total} = \sqrt{err_{phase}^2 + err_{magnitude}^2} \tag{3-64}$$

Where $\left(E_{sample} / E_{ref} \right)_{meas}$ is the measurement data taken from the system. It should be noted that the form of the error equations does not change significantly from those used for the single dielectric layer, except that now the properties of region 3 are being solved and the combined transmission term $\tilde{\tau}$ in equation (3-56) is different than in the single dielectric layer. As in the case of the single dielectric layers, the error of the magnitude and phase in equations (3-61) and (3-63) cannot be minimized individually. Thus the range of values for n_3 and $\alpha_{abs,3}$ seek to find the minimum value of the combined error in equation (3-64).

Linear Solution: Tissue on Glass Slide

In the same way that the final solution of the single dielectric layer could be simplified by various assumptions based on the experimental setup, it is possible to reduce the expression of $\tilde{\tau}$ by assuming that one or both of the dielectric regions attenuate the signal such that there is no contribution of the internal reflected signals on the measured transmission signal. For a signal that does not have multiple reflections in glass,

$$\tilde{\tau} = \left[\frac{2\tilde{n}_3\left(\tilde{n}_1 + \tilde{n}_2 \right)}{\left(\tilde{n}_2 + \tilde{n}_3 \right)\left(\tilde{n}_1 + \tilde{n}_3 \right)} \right] \Bigg/ \left(1 + \frac{\tilde{n}_2 - \tilde{n}_3}{\tilde{n}_2 + \tilde{n}_3} \tilde{\Gamma}_3 (d_1 + d_2) e^{-2\gamma_3 d_2} \right) \tag{3-65}$$

It is additionally possible to assume that there are no contributions from secondary reflections in the tissue. However, the tissue in the actual measurements is very thin compared to

the glass so this is not necessarily a reasonable approximation. The approximation removes the remaining denominator term:

$$\tilde{\tau} = \frac{2\tilde{n}_3\left(\tilde{n}_1 + \tilde{n}_2\right)}{\left(\tilde{n}_2 + \tilde{n}_3\right)\left(\tilde{n}_1 + \tilde{n}_3\right)} \tag{3-66}$$

This expression of the transmission corresponds to the transmission coefficients of the setup with tissue on glass divided by the transmission coefficients of the glass only. In order to obtain a truly linear expression for equations (3-58) and (3-59), it must be assumed that the absorption coefficient does not contribute significantly to the complex refractive index. Thus the equations become:

$$\boxed{n_3 = -\frac{c}{\omega d}\arg\left(\frac{E_{sample}}{E_{ref}}\right) + n_1} \tag{3-67}$$

$$\boxed{\alpha_{abs,3} = \frac{2}{d}\left[\ln\left(\frac{2n_3\left(n_1 + n_2\right)}{\left(n_2 + n_3\right)\left(n_1 + n_3\right)}\right) - \ln\left(\left|\frac{E_{sample}}{E_{ref}}\right|\right)\right] + \alpha_{abs,1}} \tag{3-68}$$

The effects of these approximations will be explored in more detail later in the chapter.

C. Spectroscopy Measurement Setup

Prior to finding the properties of the tissue on glass slides it was first necessary to find the properties of the glass material to serve as a reference. All measurements taken for spectroscopy in this research used the same TPS Spectra setup which can be seen in Fig. 3.3. First the time window of the spectroscopy measurement was decreased in order to avoid a second reflection present in the glass slide measurements. Then a total of 1800 individual measurements were averaged together in order to get the time domain signal for a single point. The THz signal is particularly sensitive to water content, so all spectroscopy measurements were preceded by a

minimum of 15 minutes of dry nitrogen purging of the system chamber to avoid any influence of the water vapor on the final measurement.

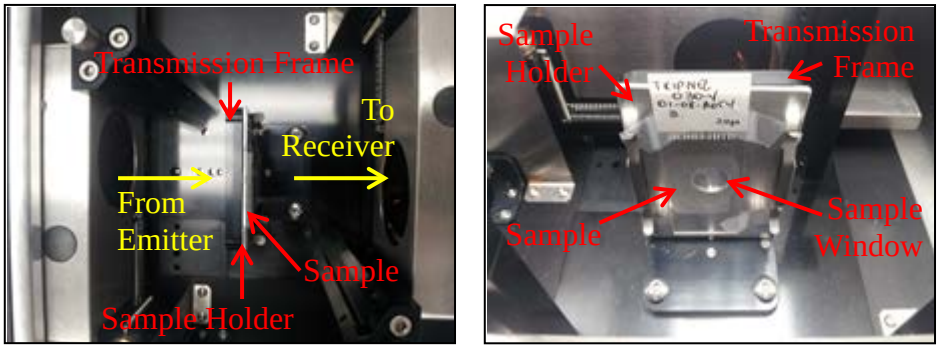

(a) (b)

Figure 3.3. Tissue sample on glass slide mounted in the standard spectroscopy module using an aluminum sample holder. Views given from (a) top and (b) the side.

The FFPE tissue from CHTN was received mounted on glass, since glass slides are the standard material for tissue sections in medical applications. However, it was later found that glass was not an ideal material for spectroscopy of the tissue due to its high attenuation of THz frequency signals. In order to determine an ideal material for mounting tissue slides, the transmitted field through the glass slide was compared to the transmitted field through two other materials. Additionally each transmitted spectrum was compared to the transmitted electric field in air without any slide material. The two other materials chosen as potential mounting media for the slides were polystyrene, a common plastic used for laboratory equipment, and tsurupica, a polymer used for THz lenses. Of the slides of each material tested, the glass and polystyrene slides were approximately 1 mm thick and the tsurupica slide was 2 mm thick. The transmitted fields measured through each material are shown in Fig. 3.4.

The frequency dependent amplitude of the transmitted electric field showed the strong attenuation of the glass slide even without the presence of tissue. In particular, the signal was taken over by the system noise around 1.2 THz. Thus any spectroscopy results that could be

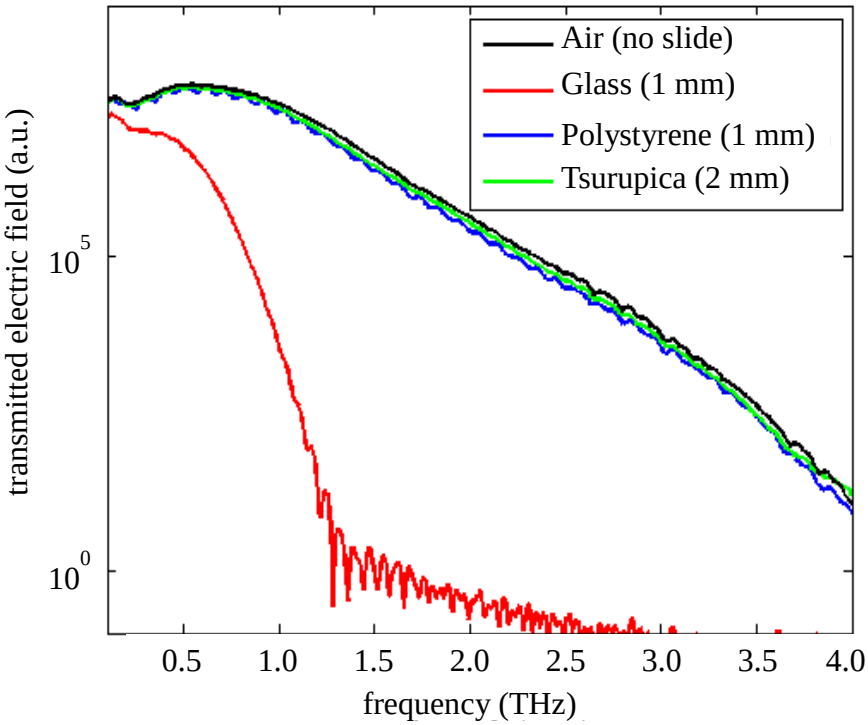

Figure 3.4. Frequency domain transmitted field versus frequency for various slide materials (glass, polystyrene, and tsurupica) compared to air

gathered from tissue on glass slides were limited to frequencies below this cutoff. The two non-glass slide materials, on the other hand, showed very good transmission characteristics for the full range of frequencies obtainable by the system. These high-transmission materials will be useful for future spectroscopy work in order to obtain the characteristics of the tissue over a wider range of frequency. However within the current work set the spectroscopy range was limited by the attenuation of the signal in glass.

Validation of THz Experimental Data of Single Layer

Prior to obtaining spectroscopy results from the tissue on glass, it was first necessary to find the THz frequency properties of the glass slide itself. As detailed in Section 3.A, this was done by comparing the measured transmitted signal through the glass slide to the measured signal when no slide was present in the system (the measurement through air). Once both signals

were obtained and the frequency-dependent ratio between the two signals was solved, the properties of the slide were determined numerically by solving equations (3-41) and (3-43) for a range of values for n_2 and $\alpha_{abs,2}$. This calculation was performed using the MATLAB code in Appendix A using a range of values defined by $0 < n_2 < 9$ and $-50 < \alpha_{abs,2} < 150$ at each frequency. Then the minimum value of the total error in equation (3-44) was used to determine which selection of the dielectric properties was the best fit at that frequency.

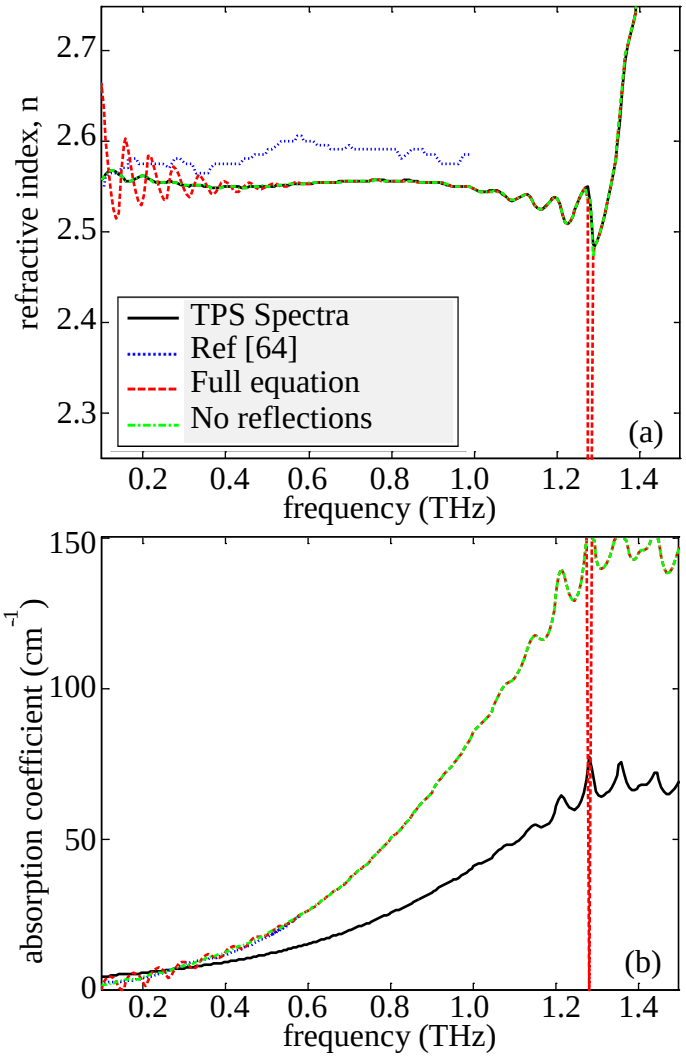

Figure 3.5: Comparison of calculated values of glass for (a) the refractive index real, and (b) the absorption coefficient.

Fig. 3.5 compares four plots in regards to the properties of the glass: 1) the values for the refractive index and absorption coefficient presented in TPS Spectra, 2) the values obtained from [64] for the measured refractive index of glass up to 1.0 THz and the absorption coefficient of glass up to 0.6 THz, 3) the values obtained from the minimization of equations (3-41) and (3-43) using the transmission term with no approximations from equation (3-36), and 4) the values obtained from equations (3-46) and (3-47) using the approximation of no internal glass reflections. The internal solution of the TPS Spectra 3000 solver uses equations of the same form as (3-46) and (3-47), except that the version of equation (3-47) used by the system utilizes a base 10 logarithm rather than the natural logarithm. The solution without approximations was referred to as the full solution, and the solution assuming that the glass internal reflections were fully attenuated was denoted as the glass approximation.

The comparison of the plots showed that all of the calculated refractive index values overlap for the range of reasonable frequency values. Although there was a small distinction between the calculated values and the properties found in [64], the separation was very small compared to the value of the refractive index. Additionally the cutoff point for the viable frequency range of spectroscopy through glass could be clearly seen in the refractive index plot. For the absorption coefficient there was a difference between the values solved numerically and the value given by TPS Spectra due to the logarithm used. The reason for the base 10 logarithm in the TPS spectra calculations is unknown. However the solutions of equations (3-41) and (3-43) using the natural logarithm agreed strongly with the absorption coefficient given by [64].

Another aspect of Fig. 3.5 to note was the wave-like effect at low frequency in the plot for the full equation solved numerically. These oscillations arose as a result of accounting for the multiple reflections in glass in the transmission term of equation (3-36). This could be intuitively

explained in that if there were multiple reflections expressed in the signal then low frequency oscillations would be seen. This was a result of the low frequency being able to reflect multiple times and still be measured while higher frequencies were fully attenuated before they could leave the glass. The large increase in attenuation over frequency shown in Fig. 3.5(b) supported this explanation as well.

D. Experimental Spectroscopy Results for Tissue Samples

In order to solve for the properties of the tissue on a glass slide in equations (3-61) and (3-63), it was first necessary to determine the variables aside from the tissue properties. The properties of the glass slide (corresponding to region 2 in the equations) were obtained from three different glass slides using the full equations in (3-41) and (3-43). It was also necessary to know the thickness of both the tissue and the glass in order to solve for the properties. In order to obtain these values, a micrometer was used to measure the thickness of the glass alone and of the tissue on the glass. These measurements were obtained from each slide as an average of six points each from glass and paraffin. The thickness of the tissue alone was the difference between the two measurements. All measurements are given in terms of millimeters in Table 1.

Table 1: Glass and/or Tissue Thickness Measurements in Millimeters (mm)

	Sample 1: 40 year old			**Sample 2: 46 year old**			**Sample 3: 22 year old**		
Slide #	Glass Only	Glass & Tissue	Tissue Only	Glass Only	Glass & Tissue	Tissue Only	Glass Only	Glass & Tissue	Tissue Only
3	1.0295	1.0390	0.0095	1.0350	1.0450	0.0100	1.0085	1.0210	0.0125
4	1.0405	1.0525	0.0120	0.9980	1.0080	0.0100	1.0320	1.0450	0.0130
5	1.0315	1.0410	0.0095	1.0365	1.0475	0.0110	1.0040	1.0160	0.0120
6	1.0190	1.0295	0.0105	1.0365	1.0460	0.0095	1.0335	1.0470	0.0135
7	0.9940	1.0040	0.0100	0.9870	0.9950	0.0080	1.0065	1.0190	0.0125
8	1.0090	1.0215	0.0125	0.9700	0.9820	0.0120	1.0320	1.0450	0.0130
9	1.0315	1.0440	0.0125	0.9680	0.9785	0.0105	1.0310	1.0460	0.0150
10	1.0295	1.0405	0.0110	0.9700	0.9820	0.0120	1.0025	1.0160	0.0135
11	1.0330	1.0475	0.0145	0.9680	0.9790	0.0110	1.0040	1.0170	0.0130

Once the values of the thickness of each region and the properties of the glass layer and air background were known, the remaining terms of refractive index and absorption coefficient in equations (3-61) and (3-63) could be solved numerically to minimize the total error between the measurements and calculated values in equation (3-64).

Another concern when applying equations (3-61) and (3-63) had to do with what approximations could be made regarding the internal reflections in the glass and the tissue. The effects of each approximation could be viewed in the same way that the different calculated values of the glass properties were viewed in Fig. 3.5. In this instance there was not a point of comparison in the literature for the properties of different FFPE tissue, so the results of the different approximations were simply shown in comparison to each other. For this comparison a single point was taken from an area of IDC from slide #8 of the 46 year old patient (Sample 2), and the reference in each formulation was the signal through glass.

The five plots that are being compared in Fig 3.6 are as follows: 1) the values for refractive index and absorption coefficient presented in TPS Spectra, 2) the values obtained from equations (3-41) and (3-43) for a single dielectric layer of the using the thickness of the tissue, 3) the solution of equations (3-58) and (3-59) with the approximation in equation (3-66) that both tissue and glass attenuate the signal instead of providing internal reflections, 4) the solution of equations (3-58) and (3-59) with the approximation in equation (3-65) that the glass attenuates the signal without providing internal reflections, and 5) the full solution of equations (3-58) and (3-59) with no approximations.

The comparison of the results showed that the TPS Spectra output and the equation for a single dielectric layer were still fairly close, with the difference in the absorption coefficient coming as a result of the different logarithms used between the THz system and equation (3-39).

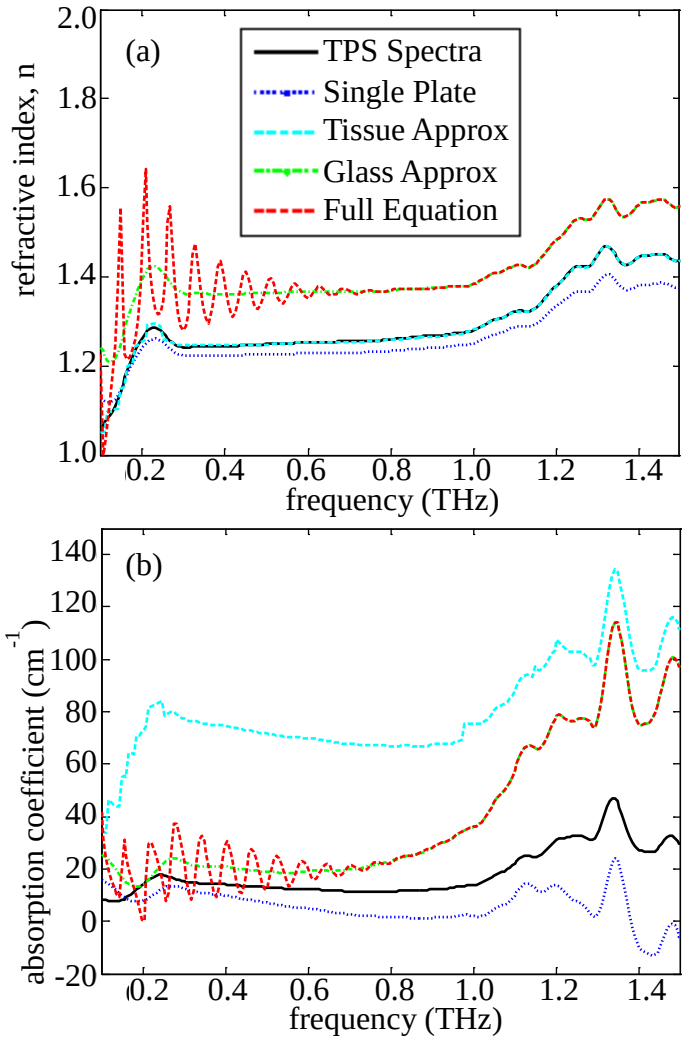

Figure 3.6: Comparison of calculated values of infiltrating ductal carcinoma on glass for (a) the refractive index (real), and (b) the absorption coefficient.

Additionally, the approximation for neither glass nor tissue having internal reflections caused the refractive index to be very close to the equations for a single plane. This arose because the effect of the imaginary part of the transmission term in equation (3-58) from equation (3-66) was very small. However, this approximation did create a substantial difference in the solution of equation (3-59) for the absorption coefficient. Finally the results of the equation with the approximation of no reflections in glass gave comparable results to the solution for the full equation except for the low-frequency wave patterns that were present in the case of the glass alone. Thus it was

reasonable to assume that the internal reflections in the glass could be ignored, as the overall effect of doing so simply removed the low frequency effects. However, the additional reflections in the tissue could not be removed from the equation in order to maintain the full solution. This was due to the fact that the tissue was very thin compared to the glass, and thus it could not be assumed to attenuate the signal that passes through it enough to justify the approximation. Thus in extending the equations to the remainder of the samples, only the full equation or the glass approximation could be used. Since the approximation did not significantly reduce the computational time of the calculation, the full solution was applied for all of the spectroscopy measurements taken within this research.

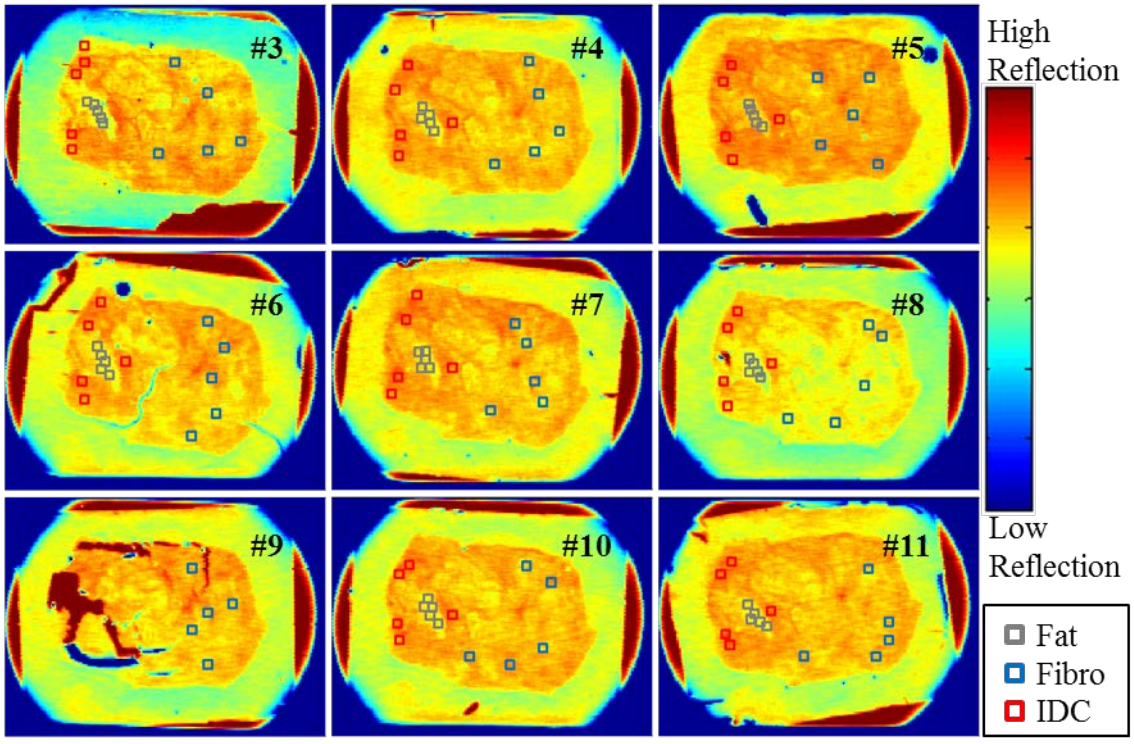

Figure 3.7: Spectroscopy Points from 40 year old patient (Sample 1). Five points from fatty (Fat), fibroglandular (Fibro), and IDC were selected from each region on each slide. Due to physical damage, only fibroglandular was taken from slide #9.

Selected Spectroscopy Points on Tissue

In order to have a statistically wide comparison of the properties of the different regions of tissue, five points were selected from each tissue region present on the slide. For this purpose it was assumed that each tissue region designated in the pathology slides (Figs. 1.5, 1.6, and 1.7) remained the same across all sections in the same sample. The THz imaging shown in Chapter 2 for the nine FFPE sections in each sample confirmed the regions being selected. These images are once again shown, now with the selected spectroscopy points from each region in Fig. 3.7 for Sample 1, Fig. 3.8 for Sample 2, and Fig. 3.9 for Sample 3.

From Sample 1, points were selected from the IDC, fibroglandular (Fibro), and fatty tissue regions of the sample. Slide #9 of this sample was found to be damaged, likely during the original mounting of the section on the slide, so only points from the fibroglandular regions

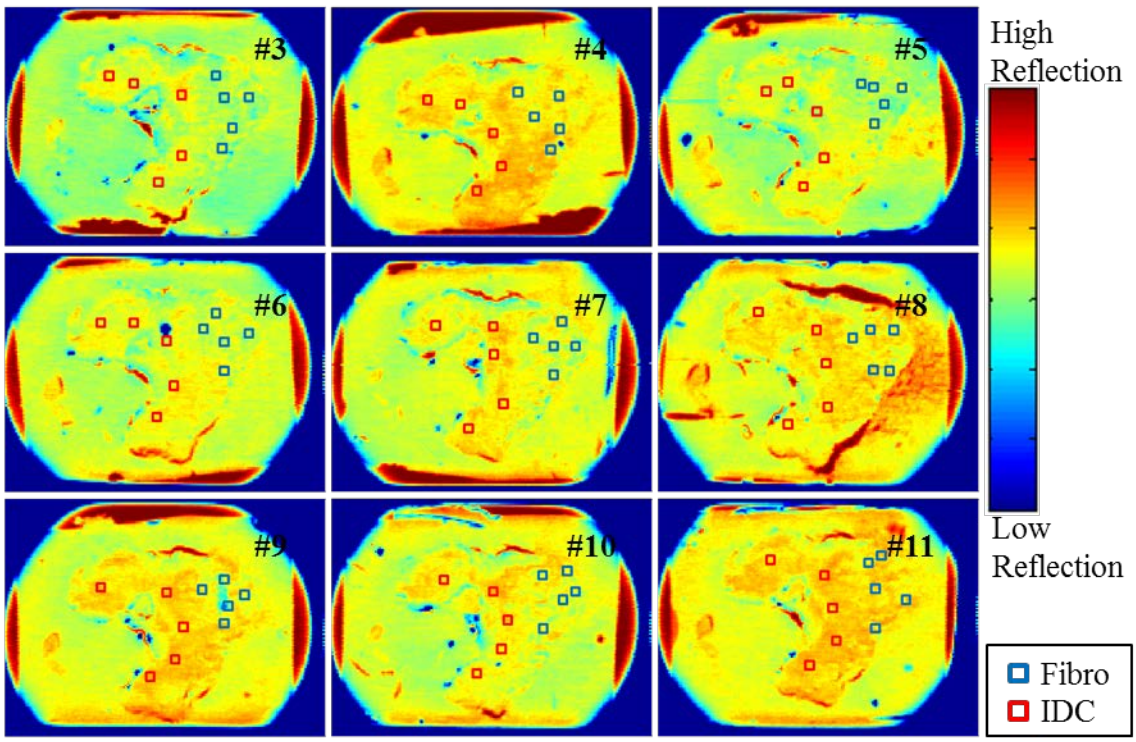

Figure 3.8. Spectroscopy points from 46 year old patient (Sample 2). Five points from fibroglandular (Fibro) and IDC were selected from each region on each slide. Although an area of fatty tissue is present in pathology, it could not be resolved for spectroscopy.

could be obtained from that particular slide. From Sample 2 the pathology denoted a small region of fatty tissue, but it was not easily seen in the FFPE slides. Thus only points from IDC and fibroglandular regions were taken. Finally from Sample 3 spectroscopy measurements were taken at points in areas denoted as DCIS, Fibroglandular, and IDC. Thus a total of 45 points was selected from each tissue type present in each sample with the exception of IDC and fatty tissue in Sample 1 due to the damaged slide #9.

Each measurement followed the same process defined before: the tissue was mounted into the system as shown in Fig. 3.3 with the point to be measured centered in the window of the aluminum sample holder, the system was purged with dry nitrogen for 15 minutes to remove water vapor, and the measurement was taken as an average of 1800 received signals. The

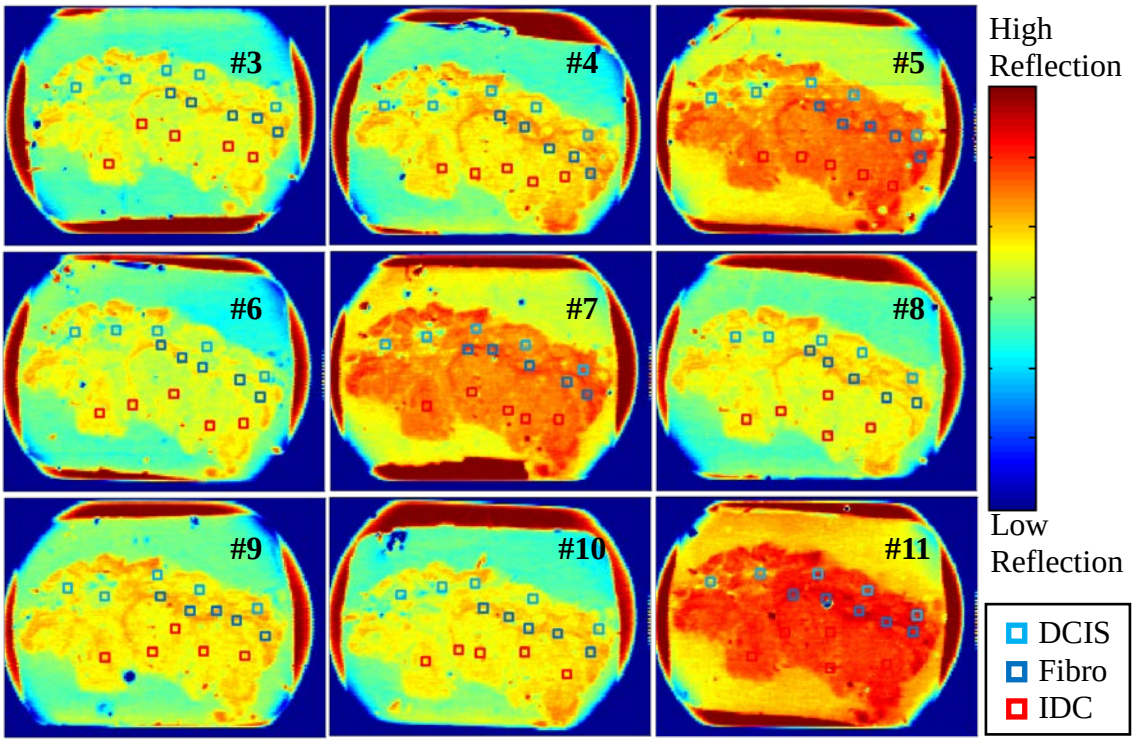

Figure 3.9. Spectroscopy points from 22 year old patient (Sample 3). Five points from ductal carcinoma in situ (DCIS), fibroglandular (Fibro) and IDC were selected from each region on each slide.

reference signal was taken from glass on the same slide as the tissue point to minimize errors from varying glass thicknesses between different slides.

Retrieving Tissue Properties from Experimental Spectroscopy Data

The full solution of equations (3-61) and (3-63) for each of the spectroscopy points was found numerically using the MATLAB code given in Appendix A. For the sake of calculating the numerical solution, the real refractive index solution was given a possible range from 0 to 9, and the absorption coefficient solution was given a possible range from -50 to 150 cm^{-1}. However, standard dielectric materials should not have a refractive index that is less than 1 or an absorption coefficient less than 0. The calculation's numerical range extended beyond those values to account for any numerical error in the solutions, and several results had values consistently outside of the reasonable range for the two values. This was due to numerical error from how thin the tissue was compared to glass. The instances of low refractive index values were due to a negative phase shift between the reference and the measured sample signals in equation (3-17). This arose from different glass thicknesses between where the reference was taken and the glass under the point where the tissue spectroscopy was obtained. The thickness of the tissue was very small and therefore easily affected by shifts in the underlying glass. Likewise the absorption coefficient was strongly affected by small magnitude shifts in the ratio between the sample and reference and changes in the real part of the refractive index.

Sample 1: Experimental Spectroscopy Results

The individual plots of the calculated refractive index versus frequency of the 40 year old patient are given in Fig. 3.10, and the absorption coefficient plots are given in Fig. 3.11. These results made use of the full solution for the dielectric properties with no approximations. In order

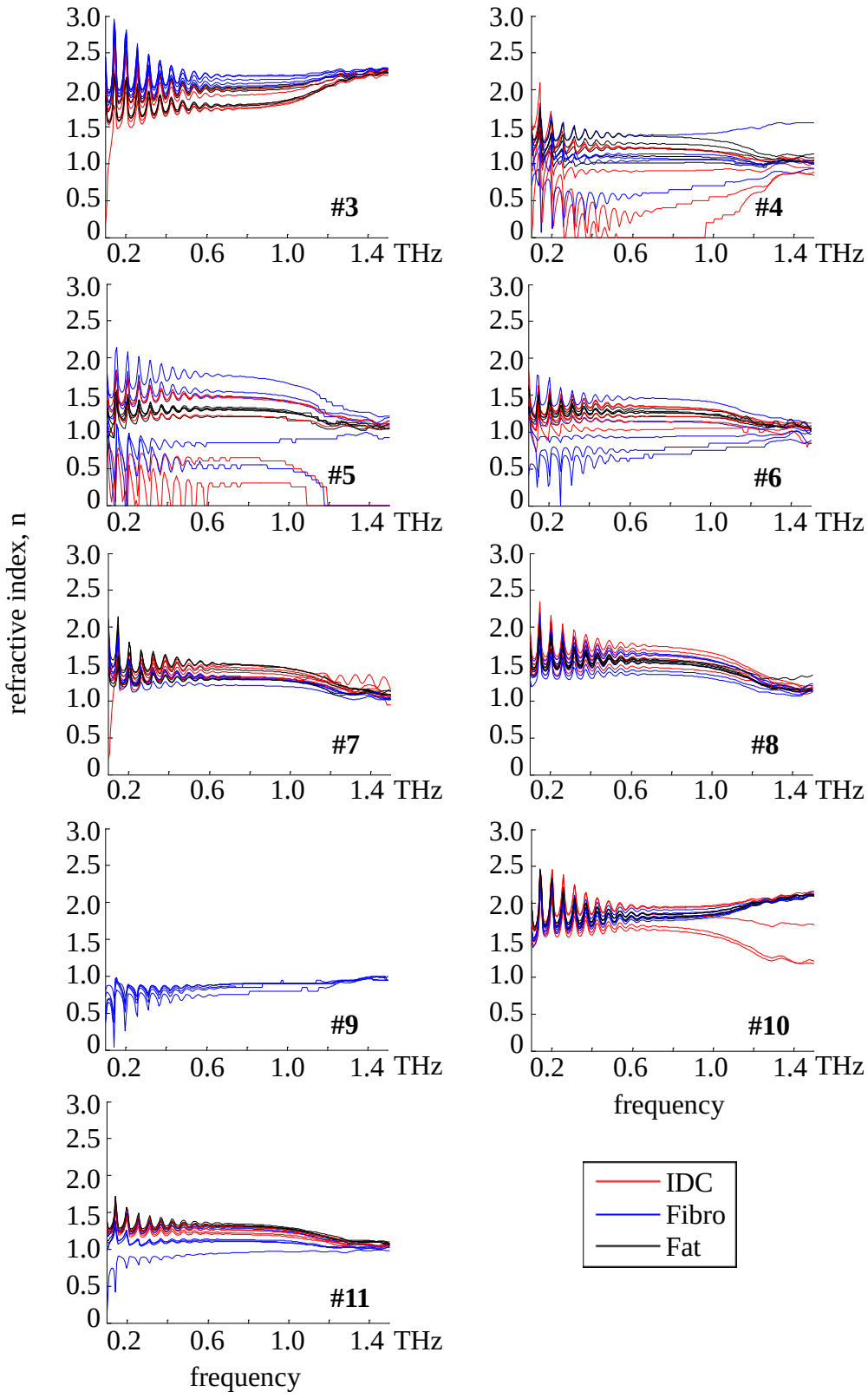

Figure 3.10: Calculated refractive index vs frequency for 40 year old patient

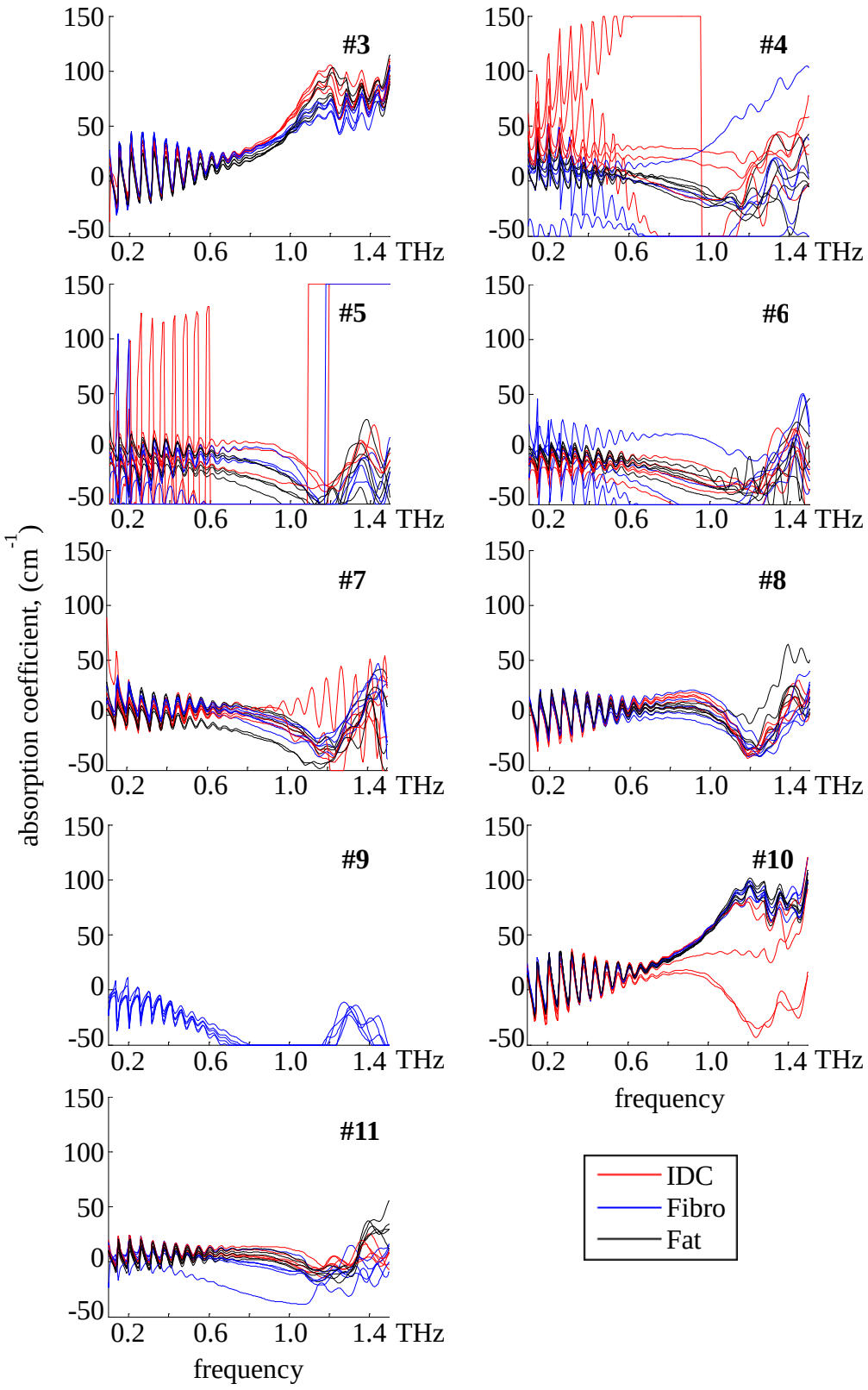

Figure 3.11: Calculated absorption coefficient vs frequency for 40 year old patient

to obtain some meaningful expression of the overall trends of the plot, slides #4 and #5 were dropped prior to obtaining the statistical expressions of the overall properties of the tissue. It should be noted that in addition to these two plots being dropped that slide #9 also had values that were unreasonable, as can be seen by the refractive index less than 1 in Fig. 3.10 and the negative absorption coefficient seen in Fig. 3.11. However, in this case the slide was kept in the statistical analysis in order to not remove too much data from the set.

With regards to the other slides, for the most part all calculated values were within the logical limits of the dielectric properties of a material except for the low frequency oscillations. As discussed in the results of the glass slide spectroscopy, these oscillations were primarily due to the calculations accounting for multiple low frequency reflections within the glass. These oscillations were shown to not be problematic for the statistical analysis of the results.

Sample 2: Experimental Spectroscopy Results

The individual plots of the calculated refractive index versus frequency of the 46 year old patient are given in Fig. 3.12, and the absorption coefficient plots are given in Fig. 3.13. These results made use of the full solution for the dielectric properties with no approximations. As was the case with the 40 year old patient, two slides with unreasonable calculated values for the dielectric properties were excluded from statistical analysis. For this sample, slide #6 was removed due to very negative refractive index calculations for some points. Additionally slide #10 was removed from the statistical analysis due to negative calculated absorption coefficients. Slide #9 was also considered for removal, but slide #10 was found to have several results against the lower limit of the calculation and would have had more significant effects on the statistical analysis if not removed.

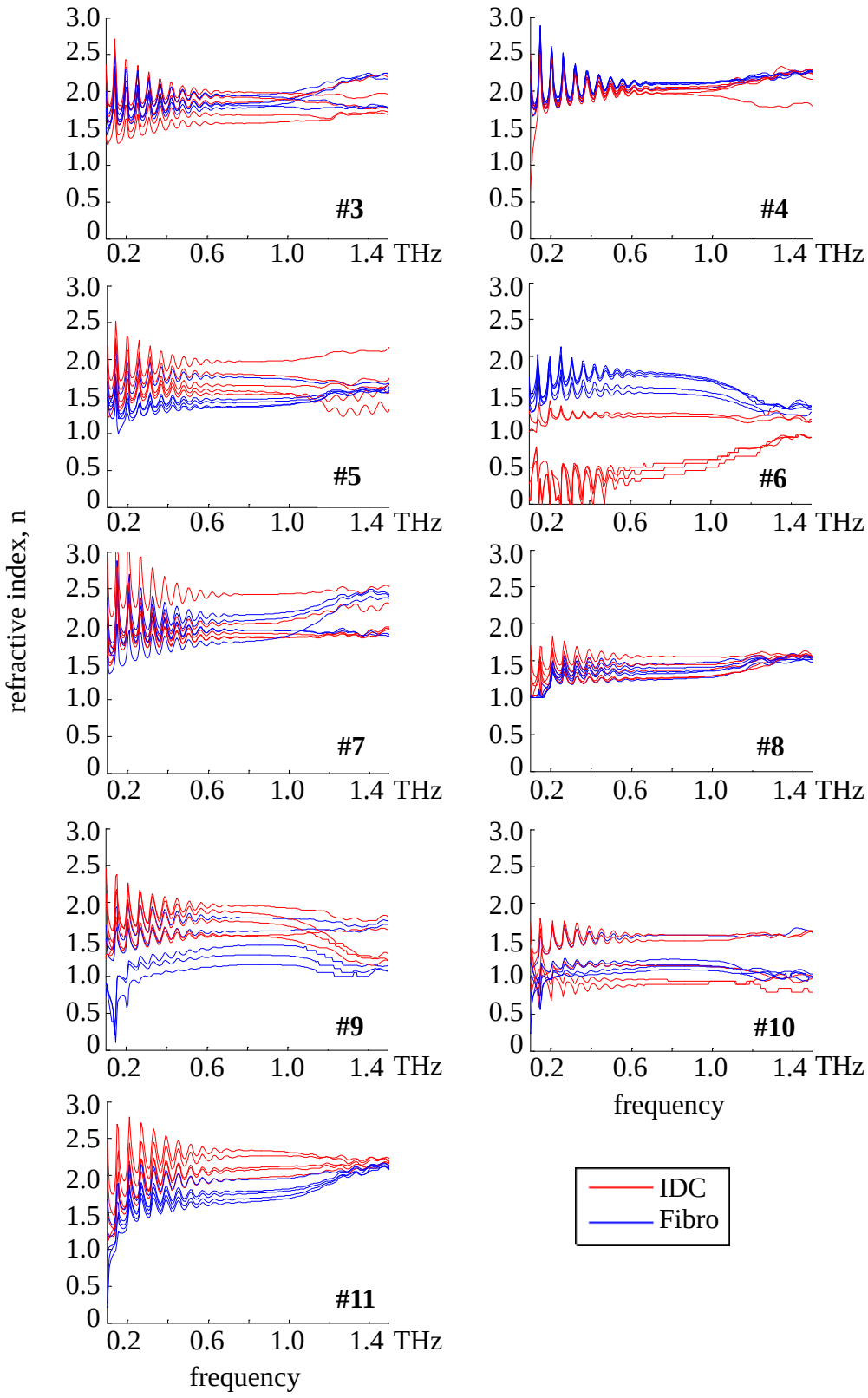

Figure 3.12: Calculated refractive index vs frequency for 46 year old patient

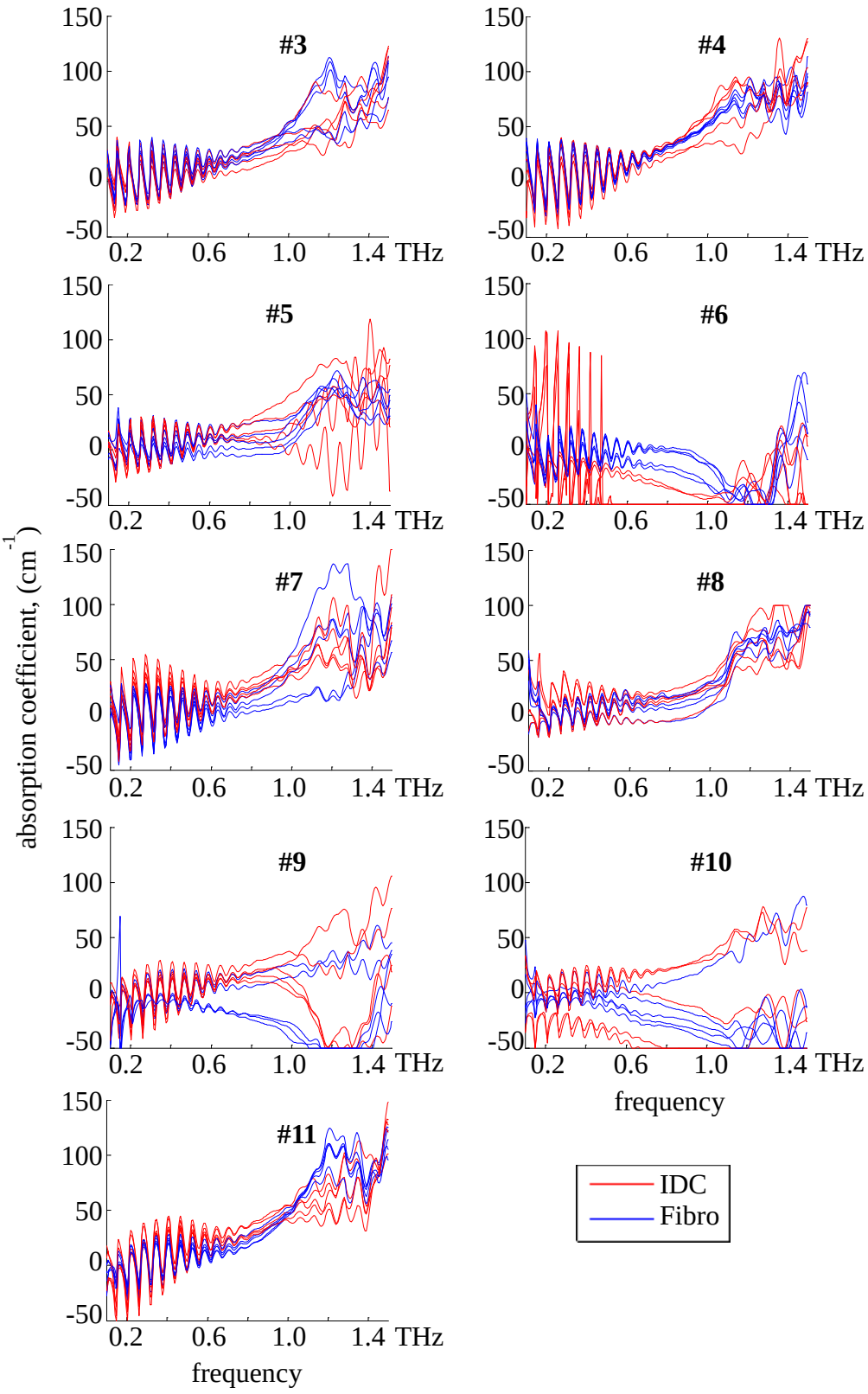

Figure 3.13: Calculated absorption coefficient vs frequency for 46 year old patient

Sample 3: Experimental Spectroscopy Results

The individual plots of the calculated refractive index versus frequency of the 22 year old patient are given in Fig. 3.14, and the absorption coefficient plots are given in Fig. 3.15. These results made use of the full solution for the dielectric properties with no approximations. Once again the individual results were first inspected for any unreasonable outlier results that might need to be removed from statistical analysis of the calculations. However, unlike with the previous samples there were not any values calculated for the refractive index that were significantly below 1. Slide #3 was the only one found to have any values significantly out of the range of permissible values. However, in viewing the plots of the absorption coefficient against frequency in Fig. 3.15 it could be seen that for slides #7 and #10 there were significantly negative values. Since these values were not dependent on the refractive indices at those points, this was likely due to unreasonable values of the amplitude in comparing the sample and reference rather than a negative phase shift. These two slides were then excluded from the statistical analysis.

Statistical Analysis of Experimental Spectroscopy Results

In order to express the overall spectroscopy results in a meaningful matter, the simplest means was to take the average of all of the data from each tissue type in each sample. This resulted in an average of 45 spectroscopy results if no outliers were removed from the statistical analysis. In order to obtain a better analysis, two slides that were found to have particularly unreasonable values were removed from each sample. This resulted in the average results expressing a combination of 35 points for most of the tissue types. The effects of removing the slides from the averaging were observed as well for each sample.

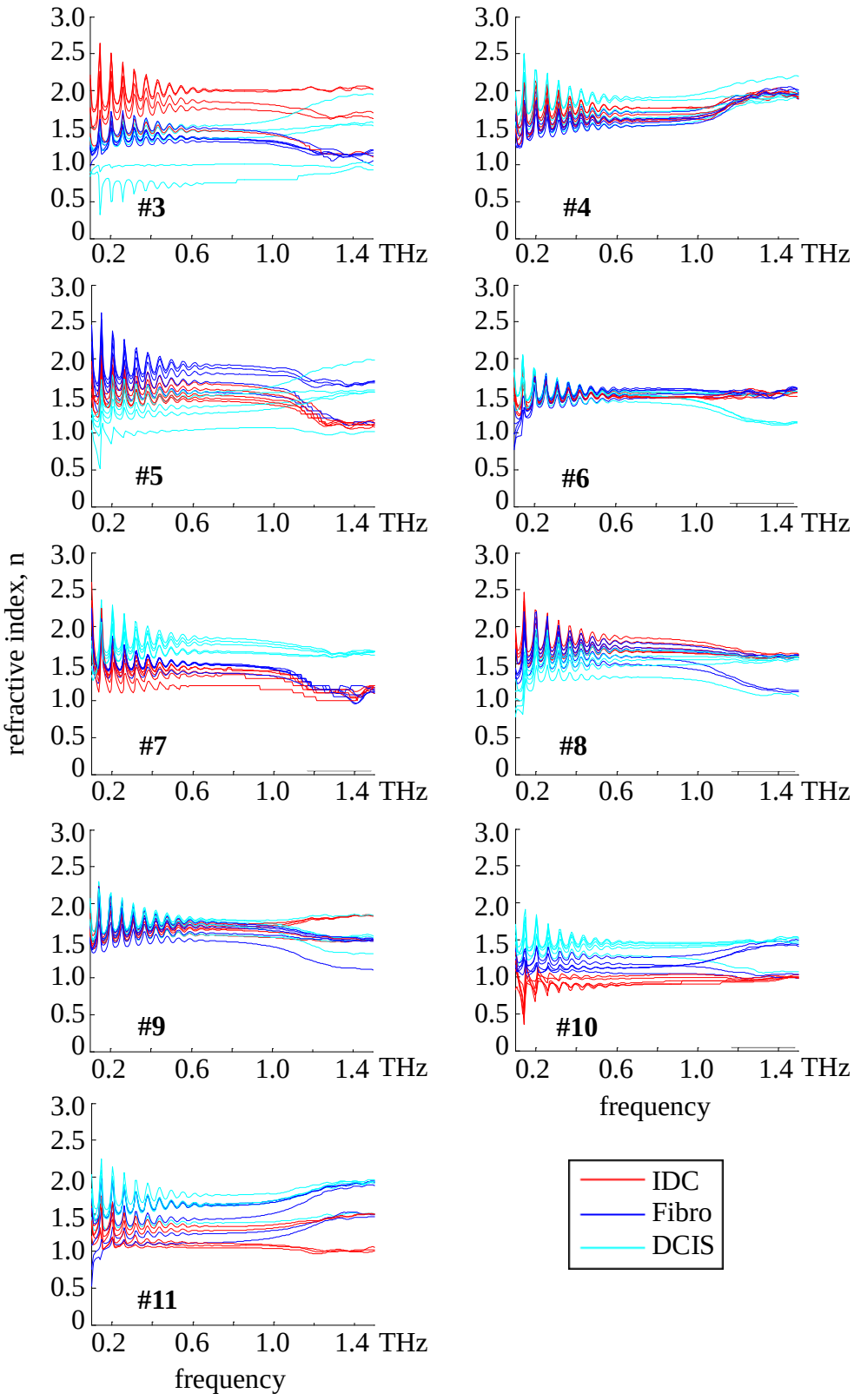

Figure 3.14: Calculated refractive index vs frequency for 22 year old patient

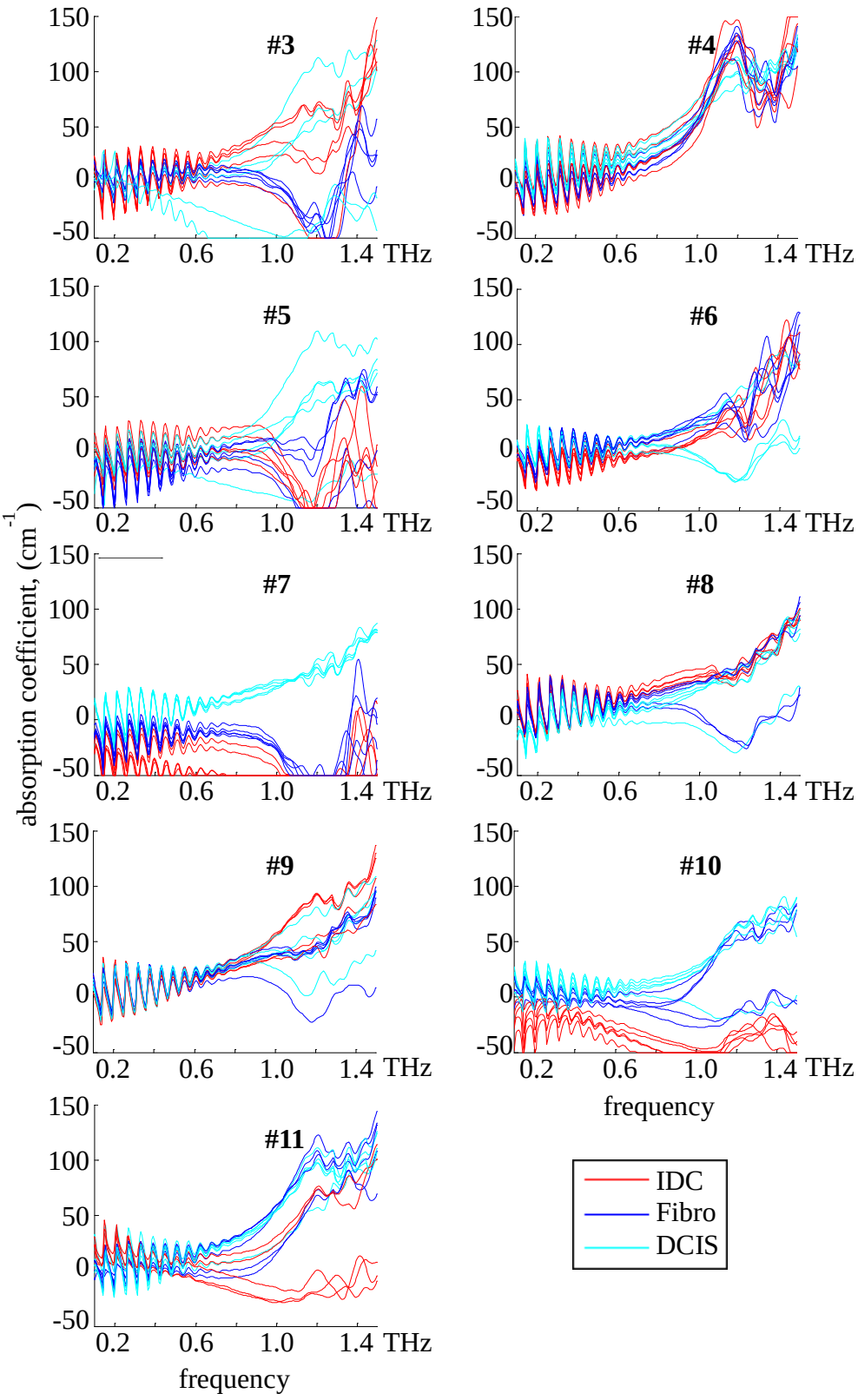

Figure 3.15: Calculated absorption coefficient vs frequency for 22 year old patient

The average results of the spectroscopy results for the 40 year old patient are given in Fig. 3.16, with parts (a) and (b) representing the average of all slides and parts (c) and (d) displaying the same results with the two outlier slides, #4 and #5, removed. The error bars applied to the plots represent the standard deviation of each average. Fig. 3.16(a) and (b) show particularly wide standard deviations for both the IDC and fibroglandular averages. The removal of slides #4 and #5 showed a significant decrease in the standard deviation for the IDC in particular, though the deviation of the fibroglandular remains high. This was likely due to the

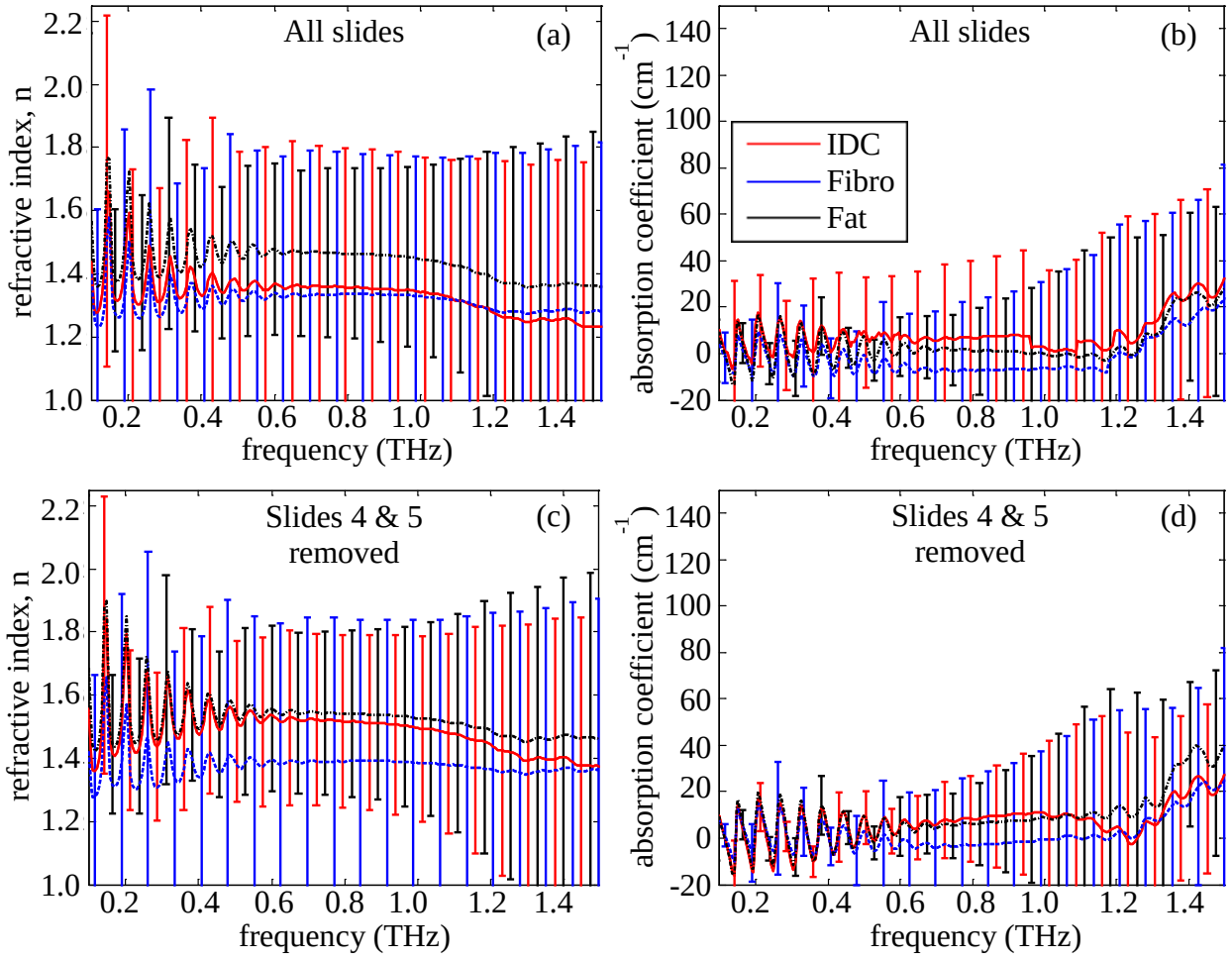

Figure 3.16: Comparison of average results and their standard deviation for 40 year old patient: (a) refractive index of all points, (b) reflection coefficient of all points, (c) refractive index with outliers removed, and (d) absorption coefficient with outliers removed

contribution of slide #9 causing a particularly wide average. The significance of the results will be discussed in the following section. Even with the outliers removed, the standard deviation of the plots overlapped considerably, indicating that there were some shared values between the different regions.

The average results of the spectroscopy results for the 46 year old patient are given in Fig. 3.17, with parts (a) and (b) representing the average of all slides and parts (c) and (d) displaying the same results with the two outlier slides, #6 and #10, removed. As with the 40 year

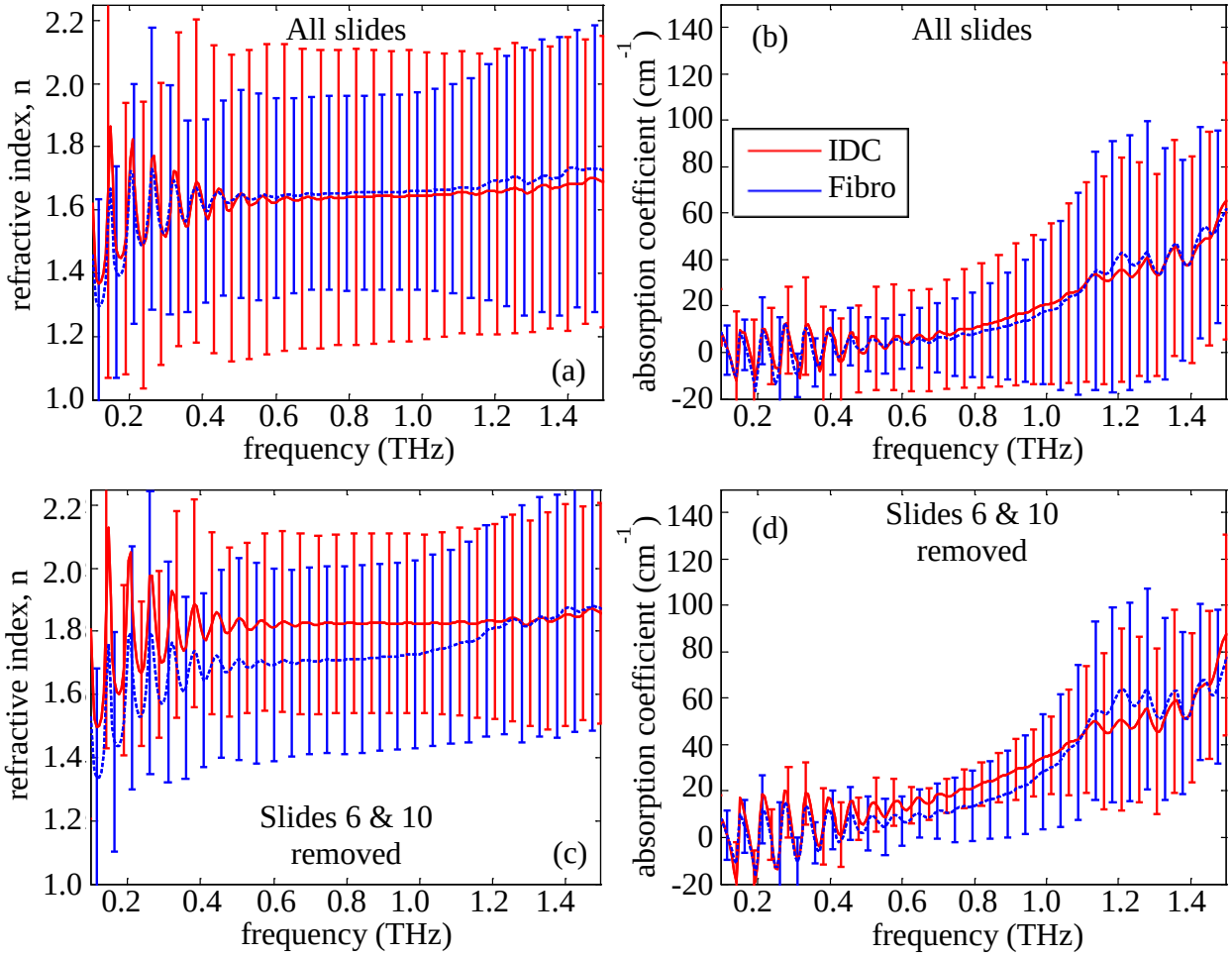

Figure 3.17: Comparison of average results and their standard deviation for 46 year old patient: (a) refractive index of all points, (b) absorption coefficient of all points, (c) refractive index with outliers removed, and (d) absorption coefficient with outliers removed

old patient, the average plots of the two tissue regions depicted in Fig. 3.17(a) and (b) showed very close results with wide standard deviations, which made any distinction between the tissues difficult. However, removing slides #6 and #10 significantly reduced the standard deviation of the IDC in particular and shifted the average away from the fibroglandular. In the plot of the absorption coefficient in Fig. 3.17 this distinction begins to create a significant differentiation between the two regions such that the average value for the fibroglandular tissue nearly lies outside of the standard deviation of the IDC.

The average results of the spectroscopy results for the 22 year old patient are given in

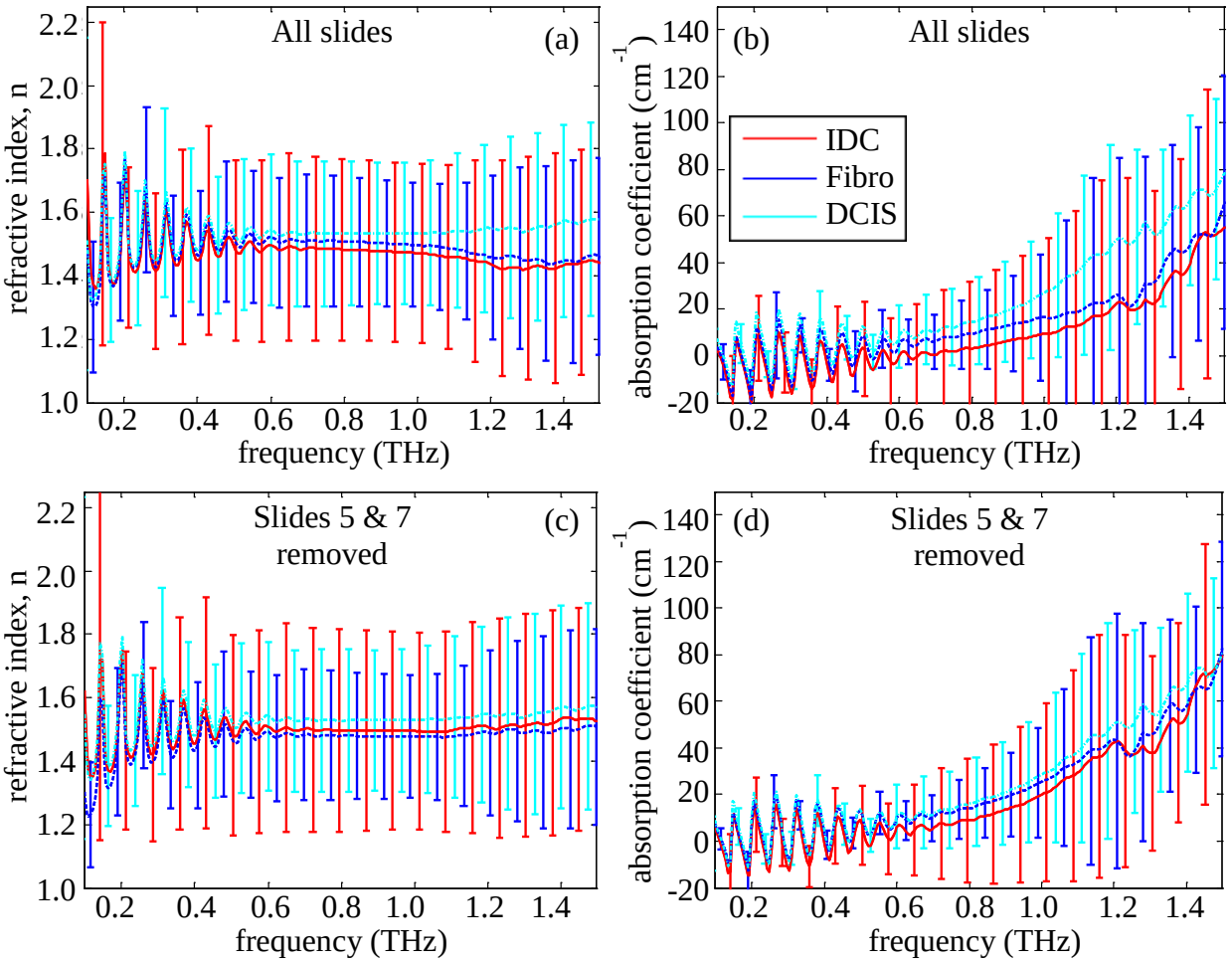

Figure 3.18: Comparison of average results and their standard deviation for 22 year old patient: (a) refractive index of all points, (b) absorption coefficient of all points, (c) refractive index with outliers removed, and (d) absorption coefficient with outliers removed.

Fig. 3.18, with parts (a) and (b) representing the average of all slides and parts (c) and (d) displaying the same results with the two outlier slides, #5 and #7, removed. The standard deviation found in the experimental spectroscopy of this sample was shown to be much lower in general than the standard deviations of the other two samples. Additionally the removal of slides #5 and #7 did not significantly improve the standard deviation of the refractive index but the deviation in the absorption coefficient was improved for both the IDC and fibroglandular plots as seen in Fig. 3.18(d). In this case there was no clear differentiation of the plots, which will be discussed in greater detail in the following section.

E. Discussion of Spectroscopy Results

The contents of this chapter showed the steps that can be taken in order to obtain the dielectric properties of tissue on glass once the dielectric properties of the glass alone are known. The methodology used to solve for the single dielectric layer of glass was compared against known values from literature and confirmed to be within a reasonable range for refractive index and very close for the published values of the absorption coefficient. It was also shown that the glass background of the tissue was thick enough such that any secondary reflections could be considered irrelevant with very little effect on the resulting calculated properties. However, this also came at the cost of the glass slide significantly attenuating the entirety of the signal such that the spectroscopy of this research was limited to less than 1.3 THz.

The spectroscopy applied to the individual samples showed that despite the strong attenuation of the glass it was still possible to obtain spectroscopy properties of the tissue on the glass slide. However this was accompanied by a fairly large occurrence of numerical error and some unreasonable values. Many of the large discrepancies in calculated values could be attributed to sensitivity of the measurement to changes in glass thickness between the reference

and sample points. However, it was still possible to draw some comparisons from the obtained spectroscopy slides.

For the 40 year old patient in Sample 1 it was possible to see a clear distinction in Fig. 3.16(c) and (d) between the calculated values from IDC and fibroglandular measurements. In addition, the average values of the fatty tissue properties overlapped closely with the IDC properties despite clear differences in the pathology of these regions. This was likely due to the region of selected fatty tissue points being small and surrounded by IDC, leading to possible overlapping of IDC tissue into the fatty tissue measurements. This was especially prominent at low frequencies, where the resolution limit of the frequency was comparatively large. Also there remained a significant overlap of the standard deviations in this tissue, which was attributable to the poorly differentiated nature of the tissue sample where the regions of IDC and fibroglandular are poorly defined. In summary, the overlap and interference of the different tissue regions was very likely, especially of fibroglandular into in the small areas of IDC tissue and surrounding IDC tissue into the very small region of fatty tissue.

For the 46 year old patient in Sample 2 the differentiation of the IDC and fibroglandular tissue was once again seen in Fig. 3.17(c) and (d) with a more distinct separation than the 40 year old patient. The standard deviations of the measurements from this sample were also far narrower than in the previous sample. This was likely due to the areas of the two different regions being clearly defined in the pathology. Of particular note were the average values given for the absorption coefficient, where the standard deviation of the IDC was very narrow and separate from the average value of fibroglandular tissue. This indicates that there was a strong distinction between the properties of these regions. Additionally, working with thicker tissue and less absorptive slide material would mean that the sensitivity of the measurements to small

fluctuations in the glass slide would no longer cause a wide standard deviation. Continued use of this methodology to find the properties of tissue with a more optimized preparation should provide even more distinct differentiation of the properties.

For the 22 year old patient in Sample 3, shown in Fig. 3.18(c) and (d), the differentiation between the regions was no longer clear. There was a strong possibility that the thin width of the fibroglandular region, estimated to be only 1-2 mm, caused some interference in the measurement points of the fibroglandular tissue, especially at lower frequencies. The lack of distinction in this range also may have been a result of the sample being obtained from a much younger patient than the other two. Differentiating cancer in younger patients is a difficulty faced by many detection techniques due to more dense breast tissue, and a greater number of samples from this age range is required in order to determine if the poor differentiation is typical or simply due to difficulty in isolating the points to measure the fibroglandular tissue.

In summary, two of the three samples showed strong distinctions between cancerous and fibroglandular tissues in the usable THz frequency ranges, while the third sample may have shown different results due to either lack of precision in selection of the fibroglandular points or due to some morphology difference due to the difference in the patient's age from the other two samples. The results of this chapter will be correlated with imaging and discussed in Chapter 4.

IV. Conclusions

Comparison of Spectroscopy and Imaging

In this work, THz techniques were successfully applied to obtain characterization of FFPE breast cancer and normal breast tissues via spectroscopy techniques. Additionally THz imaging was able to obtain reflection imaging of the same samples that provided distinction between the different tissue regions present on each slide. There was also strong agreement that can be drawn between the results of the two techniques.

Spectroscopy and characterization of Sample 1 from the 40 year old patient obtained values for the refractive index and absorption coefficient of the IDC that were distinctly larger than the values for the fibroglandular tissue. Due to the thin nature of the tissue, there was very little effect of absorption within the sample except for the glass slide. This meant that the primary contributions to the reflected signal when the tissue was analyzed with reflection imaging would have been the surface reflection of the tissue and air and the underlying reflection of tissue and the glass slide. In this situation, where reflection was the primary contribution to the signal, the region with higher refractive index had a greater reflection. This assertion could be clearly seen in the results for the IDC and fibroglandular regions of this tissue, where the imaging was able to designate the region with the highest reflection as the IDC, with fibroglandular tissue providing lower reflection. In this way the spectroscopy and imaging techniques each supported the findings of the other. The exception in this sample was the high refractive index value of the fatty tissue region compared to the fibroglandular tissue, but as stated previously this was most likely due to lack of precision in isolating the points taken from the fatty region from the surrounding IDC. This problem would be especially prevalent at the low frequencies where the spot size of the incident frequencies was large. This could also be seen in the comparison of reflection characterization, where the calculated values of the

reflection were very similar between the IDC and fatty regions while the measured values of the fatty regions were much lower than that of IDC. The difference between the spectroscopy measurements and the imaging measurements, then, is that the spectroscopy signal was greatly attenuated as it was passed through the glass. This resulted in a lower usable frequency range as seen in the plot for the transmission spectrum of the glass slide compared to the transmission through air. Additionally the small difference in values from the comparison to the theoretical value for the reflection could be explained due to there being several different densities of fibroglandular tissue present in this sample. This was sure to cause some variance in results even with the average of several points taken.

The comparison of the spectroscopy and imaging results for the 46 year old patient in Sample 2 yielded largely similar results to the case of the 40 year old. The results showed that the average values of IDC in the sample were distinctly higher than fibroglandular for both refractive index and the absorption coefficient. The absorption coefficient in particular showed clear differentiation from the average value of the fibroglandular tissue. Once again this corresponds to the results obtained from the THz reflection imaging where the region of highest reflection was also the region with the highest calculated refractive index. Additionally the results showed a very reasonable agreement between the measured values and the calculated reflection magnitudes.

As has been mentioned before, the results obtained from the 22 year old patient in Sample 3 were atypical compared to the other two samples when viewed from either the spectroscopy or imaging. However, even for this case it was possible to draw parallels between the results obtained from spectroscopy and imaging. Unlike the results of the other two samples, the refractive index and absorption coefficient obtained for the 22 year old patient did not show

any strong differentiation in value between the three different regions. However, this was in agreement with the reflection imaging, where the IDC no longer showed a particularly strong reflection and instead appeared much like the DCIS of the sample, with the higher reflection belonging to the narrow region of fibroglandular tissue. Although the spectroscopy results did not necessarily support the fibroglandular region as having a higher refractive index in this sample, this was likely due to the aforementioned difficulties in taking a precise point measurement through the glass slides in the same way as the fatty tissue region for the 40 year old patient. For the comparison of the reflection, the signals for all three regions were found to be close to the calculated values.

Future Work

The continuation of this research will seek to address two of the largest problems encountered in the spectroscopy and imaging: (1) tissue thickness and (2) the slide material. With the 10 μm thick tissue used in this research, there was very little allowance for the incident THz signal, whether transmitted or reflected, to be affected by the sample in a significant way. Additionally the relatively thick glass slide attenuated the transmission signal at higher frequencies, reducing the range for spectroscopy and causing the signal to be particularly sensitive to any change in the glass beneath the tissue. Addressing both of these challenges by working with the tissue preparation to obtain thicker tissue sections on a less absorptive material, such as polystyrene, should greatly improve the accuracy and consistency of the spectroscopy and will provide additional contrast to THz imaging. Additionally, the less absorptive slide material should make the use of transmission mode imaging a possibility. This would open up another analysis technique for future research and perhaps enable more reliable characterization in the future.

Overall, both the spectroscopy and imaging techniques in the THz range provided results in with strong correlation to each other. This was shown with the basic comparison of the refractive index and reflection magnitude and mathematically with the calculation of the reflection from the average characteristics found via spectroscopy. The agreement of these two techniques despite non-ideal preparation of the samples for THz applications, as well as the agreement of the THz imaging with the pathology assessment of the H&E slides, provides a strong case for the use of THz in continuing forward with breast cancer applications. The work successfully set up the methodology needed to expand this research to a wider number of samples and to other applications.

Ongoing research is working to image and characterize three-dimensional FFPE tissue obtained from NDRI and to obtain thicker sections for imaging. Once the methodology has been successfully applied to the three-dimensional case, the research will move into bulk fresh tissue in order to more closely address the problem of breast cancer margins.

V. References

[1] "Breast Cancer." American Cancer Society [Online]. 2013 Copyright American Cancer Society. Available: http://www.cancer.org/acs/groups/cid/documents/webcontent/003090-pdf.pdf Last revised 31 January 2014.

[2] R. G. Pleijhuis, M. Graafland, J. de Vries, J. Bart, J. S. de Jong, and G. M. van Dam. "Obtaining Adequate Surgical Margins in Breast-Conserving Therapy for Patients with Early-Stage Breast Cancer: Current Modalities and Future Directions." *Ann. Surg. Oncol.*, vol. 16, pp. 2717-2730, July 2009.

[3] American Cancer Society. Cancer Facts & Figures 2013. Atlanta. American Cancer Society, Inc.

[4] S. Glück and T. Mamounas. "Improving outcomes in early-stage breast cancer." *Oncology* (Williston Park), vol. 24, no. 11, suppl. 4, pp. 1-15, Oct. 2010.

[5] V. S. Klimberg, J. Kepple, G. Shafirstein, L. Adkins, R. Henry-Tillman, E. Youssef, J. Brito, L. Talley, and S. Korourian. "eRFA: Excision Followed by RFA—a New Technique to Improve Local Control in Breast Cancer." *Ann. Surg. Oncol.*, vol. 13, no. 11, pp. 1422-1433, September 2006.

[6] C. Arentz, K. Baxter, C. Boneti, R. Henry-Tillman, K. Westbrook, S. Korourian, and V. S. Klimberg. "Ten-Year Experience with Hematoma-Directed Ultrasound-Guided (HUG) Breast Lumpectomy." *Ann. Surg. Oncol.*, vol. 17, suppl. 3, pp. 378–383, 2010.

[7] J. A. Margenthaler, F. Gao, and V. S. Klimberg. "Margin Index: A New Method for Prediction of Residual Disease After Breast-Conserving Surgery." *Ann. Surg. Oncol.*, vol. 17, no. 10, pp. 2696–2701, 2010.

[8] A. Mackey, S. Feldman, A. Vaz, L. Durrant, C. Seaton, and V. S. Klimberg. "Radiofrequency Ablation After Breast Lumpectomy Added to Extend Intraoperative Margins in the Treatment of Breast Cancer (ABLATE): A Single-institution Experience." *Ann. Surg. Oncol.*, vol. 19, no. 8, pp. 2618-2619, March 2012.

[9] M. Dillon, E. Mc Dermott, A. O'Doherty, C. Quinn, A. Hill, N. O'Higgins. "Factors affecting successful breast conservation for ductal carcinoma in situ." *Ann. Surg. Oncol.*, vol. 14, no. 5, pp.1618-1628, February 2007.

[10] J. Uecker, E. Bui, K. Foulkrod, and J. Sabra. "Intraoperative assessment of breast cancer specimens decreases cost and number of reoperations." *Am. Surg.*, vol. 77, no. 3, pp. 342-344, 2011.

[11] L. Jacobs, "Positive Margins: The Challenge Continues for Breast Surgeons," *Ann. Surg. Oncol.*, vol. 15, no. 5, pp. 1271-1272, May 2008.

[12] L. Bathla, A. Harris, M. Davey, P. Sharma, and E. Silva. “High resolution intra-operative two-dimensional specimen mammography and its impact on second operation for re-excision of positive margins at final pathology after breast conservation surgery.” *Am. J. Surg.*, vol. 202, no. 4, pp. 387-394, 2011.

[13] M. Morrow and G. Freedman. “A Clinical Oncology Perspective on the Use of Breast MR.” *Magn. Reson. Imaging Clin. N. Am.*, vol. 14, pp. 363-378, August 2006.

[14] S. Kennedy, J. Geradts, T. Bydlon, J. Q. Brown, J. Gallagher, M. Junker, W. Barry, N. Ramanujam, and L. Wilke. “Optical breast cancer margin assessment: an observational study of the effects of tissue heterogeneity on optical contrast.” *Breast Cancer Research*, vol. 12:R91, 2010.

[15] T. P. Olsen, J. Harter, A. Muñoz, D. M. Mahvi, and T. M. Breslin. “Frozen Section Analysis for Intraoperative Margin Assessment During Breast-Conserving Surgery Results in Low Rates of Re-excision and Local Recurrence.” *Ann. Surg. Oncol.*, vol. 14, no. 10, pp. 2953-2960, August 2007.

[16] N. Cabioglu, K. K. Hunt, A. A. Sahin, H. M. Kuerer, G. V. Babiera, S. E. Singletary, G. J. Whitman, M. I. Ross, F. C. Ames, B. W. Feig, T. A. Buchholz, and F. Meric-Berstam. “Role of Intraoperative Margin Assessment in Patients Undergoing Breast-Conserving Surgery.” *Ann. Surg. Oncol.*, vol. 14, no. 4, pp. 1458-1471.

[17] V. S. Klimberg, C. Boneti, L. L. Adkins, M. Smith, E. Seigel, V. Zharov, S. Ferguson, R. Henry-Tillman, B. Badgwell, and S. Korourian. “Feasibility of Percutaneous Excision Followed by Ablation for Local Control in Breast Cancer.” *Ann. Surg. Oncol.*, vol. 18, no. 11, October 2011.

[18] B. Ferguson and X. Zhang. “Materials for terahertz science and technology.” *Nature Materials*, vol. 1, pp 26-33, 2002.

[19] I. Duling and D. Zimdars. “Terahertz imaging: Revealing hidden defects.” *Nature Photonics*, vol. 3, pp. 630-632, 2009.

[20] Y. C. Shen, T. Lo, P. F. Taday, B. E. Cole, W. R. Tribe, and M. C. Kemp. “Detection and identification of explosives using terahertz pulsed spectroscopic imaging.” *Appl. Phys. Lett.* vol. 86, 241116, 2005.

[21] V. Sharma, S. Shivalingaiah, Y. Peng, D. Euhus, Z. Gryczynski, and H. Liu. “Auto-fluorescence lifetime and light reflectance spectroscopy for breast cancer diagnosis: potential tools for intraoperative margin detection.” *Biomedical Optics Express*, vol. 3, no. 8, pp. 1825-1840, 9 July 2012.

[22] J. Q. Brown, T. M. Bydlon, L. M. Richards, B. Yu, S. A. Kennedy, J. Geradts, L. G. Wilke, M. K. Junker, J. Gallagher, W. T. Barry, and M. Ramanujam. “Optical Assessment of Tumor Resection margins in the Breast.” *IEEE J. Selected Topics Quantum Electronics*, vol. 16, no. 3, pp. 530-544, May 2010.

[23] A. S. Haka, Z. Volynskaya, J. A. Gardecki, J. Nazemi, J. Lyons, D. Hicks, M. Fitzmaurice, R. R. Dasari, J. P. Crowe, and M. S. Feld. “In vivo Margin Assessment during Partial Mastectomy Breast Surgery Using Raman Spectroscopy.” *Cancer Res.*, vol. 66, 15 March 2006.

[24] H. L. Fu, B. Yu, J. Y. Lo, G. M. Palmer, T. F. Kuech, and N. Ramanujam. “A low-cost, portable, and quantitative spectral imaging system for application to biological tissues.” *Optics Express*, vol. 18, no. 12, 7 June 2010.

[25] F. T. Nguyen, A. M. Zysk, E. J. Chaney, J. G. Kotynek, U. J. Oliphant, F. J. Bellafiore, K. M. Rowland, P. A. Johnson, and S. A. Boppart. ”Intraoperative Evaluation of Breast Tumor Margins with Optical Coherence Tomography.” *Cancer Res.*, vol. 69, pp. 8790-8796, 2009.

[26] I. J. Bigio, S. G. Bown, G. Briggs, C. Kelley, S. Lakhani, D. Pickard, P. M. Ripley, I. G. Rose, and C. Saunders. “Diagnosis of breast cancer using elastic-scattering spectroscopy: Preliminary clinical results.” *J. Biomed. Opt.*, vol. 5, pp. 221–228, Apr. 2000.

[27] P. Y. Han, G. C. Cho, and X. Zhang. “Time-domain transillumination of biological tissues with terahertz pulses.” *OPTICS LETTERS*, vol. 25, no. 4, 15 February 2000.

[28] G. J. Wilmink and J. E. Grunt. “Invited Review Article: Current State of Research on Biological Effects of Terahertz Radiation.” *J. Infrared Milli-Terahz Waves*, vol. 32, pp. 1074-1122, 2011.

[29] M. S. Sherwin, C. A. Schmuttenmaer, and P. H. Bucksbaum, “DOE-NSF-NIH Workshop on Opportunities in THz Science,” science.energy.gov/~/media/bes/pdf/reports/files/thz_rpt.pdf

[30] P. H. Siegel. “Terahertz Technology in Biology and Medicine.” *IEEE Trans. on Microwave Theory and Techniques*, vol. 53, no. 10, pp. 2438-2447, 2004.

[31] A. J. Fitzgerald, V. P. Wallace, M. Jimenez-Linan, L. Bobrow, R. J. Pye, A. D. Purushotham, and D. D. Arnone. “Terahertz Pulsed Imaging of Human Breast Tumors.” *Radiology*, vol. 239, no. 2, pp. 533-540, May 2006.

[32] P. C. Ashworth, E. Pickwell-MacPherson, E. Provenzano, S. E. Pinder, A. D. Purushotham, M. Pepper, and V. P. Wallace. “Terahertz pulsed spectroscopy of freshly excised human breast cancer.” *Opt. Express*, vol. 17, no. 15, pp. 12444-12454, 2009.

[33] C. Yu, S. Fan, Y. Sun, and E. Pickwell-MacPherson. “The potential of terahertz imaging for cancer diagnosis: A review of investigations to date.” *Quant. Imaging Med. Surg. 2012*, vol. 2, pp. 33-45.

[34] Y. Miura, A. Kamataki, M. Uzuki, T. Sasaki, J. Nishizawa, and T. Sawai. “Terahertz-Wave Spectroscopy for Precise Histopathological Imaging of Tumor and Non-tumor Lesions in Paraaffin Sections.” *Tohoku J. Exp. Med.*, vol. 223, no. 4, pp. 291-296, 17 March 2011.

[35] M. H. Arbab, T. C. Dickey, D. P. Winebrenner, A. Chen, M. B. Klein, and P. D. Mourad. "Terahertz reflectrometry of burn wounds in a rat model." *Biomedical Optics Express*, vol. 2, no. 8, pp. 2339-2347, 1 August 2011.

[36] S. Sy, S. Huang, Y. J. Wang, J. Yu, A. Ahuja, Y. Zhang, and E. Pickwell-MacPherson, "Terahertz spectroscopy of liver cirrhosis: investigating the origin of contrast," *Phys. Med. Biol.*, vol. 55, pp. 7587-7596, 2010.

[37] Y. Sun, M. Y. Sy, Y. J. Wang, A. T. Ahuja, Y. Zhang, and E. Pickwell-MacPherson. "A promising diagnostic method: Terahertz pulsed imaging and spectroscopy." *World J. Radiol.*, vol. 3, iss. 3, pp. 55-65, 28 March 2011.

[38] A. J. Fitzgerald, E. Berry, N. N. Zinov'ev, S. Homer-Vanniasinkam, R. E. Miles, J. M. Chamberlain, and M. A. Smith. "Catalogue of Human Tissue Optical Properties at Terahertz Frequencies." *Journal of Biological Physics*, vol. 129, pp. 123-128, 2003.

[39] S. Y. Huang, Y. X. J. Wang, D. K. W. Yeung, A. T. Ahuja, Y. Zhang, and E. Pickwell-MacPherson. "Tissue characterization using terahertz pulsed imaging in reflection geometry." *Phys. Med. Biol.*, vol. 54, pp. 149-160, 2009.

[40] F. Formanek, M. Brun, and A. Yasuda. "Contrast improvement of terahertz images of thin histopathologic sections." *Biomedical Optics Express*, vol. 2, no. January 2011.

[41] C. J. Strachan, P. F. Taday, D. A. Newnham, K. C. Gordon, J. A. Zeitler, M. Pepper, and T. Rades. "Using Terahertz Pulsed Spectroscopy to Quantify Pharmaceutical Polymorphism and Crystallinity." *Journal of Pharmaceutical Sciences*, vol. 94, pp. 837-846, 2005.

[42] M. Brun, F. Formanek, A. Yasuda, M. Sekine, N. Ando, and Y. Eishii. "Terahertz imaging applied to cancer diagnosis." *Phys. Med. Biol*., vol. 55, pp. 4615-4623, 2010.

[43] G. Reese, C. Reid, R. Goldin, M. Tran-Dang, A. Fitzgerald, P. Tekkis, and V. P. Wallace. "Using terahertz pulsed imaging (TPI) to identify colonic pathology." *33rd International Conference on IRMMW-THz*, 15-19 September 2008.

[44] F. Wahaiaa, G. Valusis, L. M. Bernardo, A. Almeida, J. A. Moreira, P. C. Lopes, J. Macutkevic, I. Kasalynas, D. Seliuta, R. Adomavicius, R. Henrique, and M. Lopes. "Detection of colon cancer by terahertz techniques." *Journal of Molecular Structure*, vol. 1006, iss. 1-3, pp. 77-82, 14 December 2011.

[45] Y. C. Sim, J. Y. Park, K. Ahn, C. Park, and J. Son. "Terahertz imaging of excised oral cancer at frozen temperature." *Biomedical Optics Express*, vol. 4, no. 8, 1 August 2013.

[46] A. J. Fitzgerald, V. P. Wallace, M. Jimenez-Linan, L. Bobrow, R. J. Pye, A. D. Purushotham, and D. D. Arnone. "Terahertz Pulsed Imaging of Human Breast Tumors." *Radiology*, vol. 239, no. 2, pp. 533-540, May 2006.

[47] P. C. Ashworth, E. Pickwell-Macpherson, E. Provenzano, S. E. Pinder, A. D. Purushotham, M. Pepper, and V. P. Wallace. “Terahertz pulsed spectroscopy of freshly excised human breast cancer.” *Opt. Express*., vol. 17, no. 15, pp. 12444-12454, 2009.

[48] S. W. Smye, J. M. Chamberlain, A. J. Fitzgerald, and E. Berry. “The interaction between Terahertz radiation and biological tissue.” *Physics in Medicine and Biology*, vol. 46, no. 9, 22 August 2001.

[49] A. M. Hassan, D. C. Hufnagle, M. El-Shenawee, and G. E. Pacey. “Terahertz Imaging for Margin Assessment of Breast Cancer Tumors.” *Proc. of 2012 IEEE MTT-S International Microwave Symposium Digest*, 17-22 June 2012.

[50] A. M. Hassan, D. C. Hufnagle, G. E. Pacey, and M. El-Shenawee. “Terahertz Tomography Technique for the Assessment of Breast Cancer Tumor Margins.” *Proc. of 2012 IEEE Antennas and Propagation Society International Symposium*, Chicago, Illinois, 8-14 July 2012.

[51] T. C. Bowman, A. M. Hassan, and M. El-Shenawee. "Imaging 2D Breast Cancer Tumor Margin at Terahertz Frequency using Numerical Field Data based on DDSCAT." *Applied Computational Electromagnetics Society Journal*, vol. 28, no. 11, November 2013.

[52] N. Burford, M. El-Shenawee, C. O’Neal, and K. Olejniczak. “Terahertz Imaging for Nondestructive Evaluation of Packaged Power Electronic Devices.” *International Journal of Emerging Technology and Advanced Engineering*, vol. 4, no. 1, pp. 395-401, January 2014.

[53] T. Bowman and M. El-Shenawee. "Pulsed Terahertz Spectrometry of Excised Breast Cancer Tissue." *Proc. of the IEEE Int. Symp. on Antennas and Prop. and USNC/URSI National Radio Science Meeting*, Orlando, USA, 7-13 July 2013.

[54] T. Bowman and M. El-Shenawee. "Terahertz Spectroscopy and Imaging of FFPE Breast Cancer Tissue Samples." *Proc. of the 8th Annual Breast Cancer Challenge Conference*, Branson, USA, 26-27 July 2013.

[55] T. Bowman, M. El-Shenawee, and S. G. Sharma. "Pulsed Terahertz Imaging of Heterogeneous Breast Cancer Tissue." Poster. *2013 ABI Fall Research Symposium*, Little Rock, USA, 15 October 2013.

[56] T. Bowman, M. El-Shenawee. "Imaging and Analysis of Heterogeneous Breast Cancer Tissue Using Pulsed Terahertz System." *Proc. of 2014 National Radio Science Meeting*, Boulder, USA, 8-11 January 2014.

[57] T. Bowman, M. El-Shenawee, and S. G. Sharma. "Terahertz Spectroscopy for the Characterization of Excised Human Breast Tissue." *Proc. of 2014 IEEE MTT-S International Microwave Symposium*, Tampa Bay, FL, 1-6 June 2014.

[58] http://hugin.sourceforge.net/

[59] http://www.teraview.com

[60] S. J. Orfanidis. *Electromagnetic Waves and Antennas*. Copyright 1999-2013 Sophocles J. Orfanidis. Published online at www.ece.rutgers.edu/~orfanidi/ewa

[61] Carl T.A. Johnk. *Engineering Electromagnetic Fields and Waves*. 2nd ed. John Wiley & Sons, Inc. Copyright 1988.

[62] K. Sato, T. Ihara, H. Saito, S. Ito, T. Tanaka, K. Sugai, N. Ohmi, Y. Murakami, M. Shibayama, Y. Konishi, and T. Kimura. "Measurements of Reflection and Transmission Characteristics of Interior Structures of Office Building in the 60-GHz Band." *IEEE Trans. on Ant. and Propag.*, vol. 45, no. 12, pp. 1783-1792, 12 August 1997.

[63] L. Duvillaret, F. Garet, and J. Coutaz. "A Reliable Method for Extraction of Material Parameters in Terahertz Time-Domain Spectroscopy." *IEEE Journal of Selected Topics in Quantum Mechanics*, vol. 2, no. 3, pp. 739-746, 19 November 1996.

[64] R. Piesiewicz, C. Jansen. S. Wietzke, D. Mittleman, M. Koch, and T. Kürner. "Properties of Building and Plastic Materials in the THz Range." *Int J Milli Waves*, vol. 28, iss. 5, pp. 363-371, May 2007.

Appendix A: MATLAB Code for Retrieving the Electrical Properties of Tissue

Single Dielectric Layer

The following code was used to calculate the spectroscopy results of a point taken from an empty glass slide (or other single layer sample) once the transmission magnitude and phase compared to the reference were exported from the THz system.

```
% =======
% This file reads the 'Transmission' and 'Transmission Phase' files
% produced by TPS Spectra in order to calculated the dielectric
% properties of a single layer of material

mag=csvread('PSTxnh.csv');  % Load Tx magnitude for point of glass
pha=csvread('PSPhnh.csv');    % Load Tx phase for point on glass

nmin=0;                 % Minimum for swept refractive index
nmax=9;                 % Maximum for swept refractive index
nsteps=150;             % Number of refractive index steps
alphamin=-50;           % Minimum for swept absorption coefficient (1/cm)
alphamax=150;           % Maximum for swept absorption coefficient (1/cm)
alphasteps=500;         % Number of absorption coefficient steps
refinesteps=50;         % Number of refinement steps

dsample=1;              % Thickness of sample im mm

nbg=1+j*0;              % Refractive index of background material (air)

waven=mag(:,1);                     % Frequency range from system
magfreq=mag(:,2);                   % Tx magnitudes from file
phasefreq=-1*pha(:,2);              % Tx phase from file
phasefrequn=unwrap(phasefreq);      % Unwrap Tx phase to be continuous

L=length(waven);

clear Enorm n alph

% Expression of Tx signal in exponential form
for ii=1:L
   Enorm(ii)=sqrt(magfreq(ii))*exp(j*phasefreq(ii));
end

% Solve at each frequency
for stat=1:700
```

```
% Define range of n and alpha
nrange=nmin:(nmax-nmin)/(nsteps):nmax;
alpharange=alphamin:(alphamax-alphamin)/(alphasteps):alphamax;

clear tx1 phasediff internal1 internal2 transmitted transmitphase zerobalance
clear zerobalancereal zerobalanceimag2 zerobalancetotal

zeromin=1;
refnindex=1;
alphindex=1;

% Solve across range of n and alpha
for nn=1:nsteps+1
   for aa=1:alphasteps+1
      nreal=nrange(nn);
      cn=nreal-j*1/(2*2*pi*waven(stat))*alpharange(aa);
      gamma1=j*2*pi*waven(stat)*100*nbg;
      gamma2=j*2*pi*waven(stat)*100*cn;

      % Transmission components
      tx1(nn,aa)=(2*nreal/(nreal+nbg));
      phasediff(nn,aa)=exp(-1*(gamma2-gamma1)*dsample*1e-3);
      phasenorm(nn,aa)=-1*(gamma2-gamma1)*dsample*1e-3;
      internal1(nn,aa)=2/((nbg+nreal)/nbg);
      internal2(nn,aa)=1/(1-(nbg-nreal)^2/(nbg+nreal)^2*exp(-2*gamma2*dsample*1e-3));

      transmitted(nn,aa)=tx1(nn,aa)*internal1(nn,aa)*internal2(nn,aa);
      transmitphase(nn,aa,stat)=angle(transmitted(nn,aa));

      % Magnitude and phase error
      zerobalancereal(nn,aa)=real(log(transmitted(nn,aa)))+...
         real(phasenorm(nn,aa))-log(sqrt(magfreq(stat)));
      zerobalanceimag2(nn,aa)=imag(log(transmitted(nn,aa)))+...
         imag(phasenorm(nn,aa))-phasefrequn(stat);

      % Total error
      zerobalancetotal(nn,aa)=zerobalancereal(nn,aa)+i*zerobalanceimag2(nn,aa);

      if abs(zerobalancetotal(nn,aa))<zeromin;
         zeromin=abs(zerobalancetotal(nn,aa));
         refnindex=nn;
         alphindex=aa;
      end
   end
end
```

```
% If within limit of initial range, refines solution
if (refnindex~=1)&&(refnindex~=nsteps+1)&&...
      (alphindex~=1)&&(alphindex~=alphasteps+1)

nrange2=nrange(refnindex-1):(nrange(refnindex+1)-...
   nrange(refnindex-1))/refinesteps:nrange(refnindex+1);
alpharange2=alpharange(alphindex-1):(alpharange(alphindex+1)-...
   alpharange(alphindex-1))/refinesteps:alpharange(alphindex+1);
refnindex2=26;
alphindex2=26;

for nn2=1:(refinesteps+1)
   for aa2=1:(refinesteps+1)
      nreal=nrange2(nn2);
      cn=nreal-j*1/(2*2*pi*waven(stat))*alpharange2(aa2);
      gamma1=j*2*pi*waven(stat)*100*nbg;
      gamma2=j*2*pi*waven(stat)*100*cn;

      tx1(nn2,aa2)=(2*nreal/(nreal+nbg));
      phasediff(nn2,aa2)=exp(-1*(gamma2-gamma1)*dsample*1e-3);
      phasenorm(nn2,aa2)=-1*(gamma2-gamma1)*dsample*1e-3;
      internal1(nn2,aa2)=2/((nbg+nreal)/nbg);
      internal2(nn2,aa2)=1/(1-(nbg-nreal)^2/(nbg+nreal)^2*exp(-2*gamma2*dsample*1e-3));

      transmitted(nn2,aa2)=tx1(nn2,aa2)*internal1(nn2,aa2)*internal2(nn2,aa2);
      transmitphase(nn2,aa2)=angle(transmitted(nn2,aa2));

      zerobalancereal(nn2,aa2)=real(log(transmitted(nn2,aa2)))+...
         real(phasenorm(nn2,aa2))-log(sqrt(magfreq(stat)));
      zerobalanceimag2(nn2,aa2)=imag(log(transmitted(nn2,aa2)))+...
         imag(phasenorm(nn2,aa2))-phasefrequn(stat);
      zerobalancetotal(nn2,aa2)=zerobalancereal(nn2,aa2)+i*zerobalanceimag2(nn2,aa2);

      if abs(zerobalancetotal(nn2,aa2))<zeromin;
         zeromin=abs(zerobalancetotal(nn2,aa2));
         refnindex2=nn2;
         alphindex2=aa2;
      end
   end
end

   n(stat)=nrange2(refnindex2);
   alph(stat)=alpharange2(alphindex2);
   waven(stat);
```

```
else
   n(stat)=nrange(refnindex);
   alph(stat)=alpharange(alphindex);
   waven(stat);

end
end

% Output n and alph are each arrays of the n and alpha at the point
```

Tissue on Glass Calculation

The following code was used to calculate the spectroscopy results of every point of a slide once the transmission magnitude and phase compared to the reference were exported from the THz system.

```
% =======
% This file reads the 'Transmission' and 'Transmission Phase' files
% produced by TPS Spectra as well as loading a defined reference substrate
% (glass) properties file in order to calculate the dielectric properties.

mag=csvread('035-3Txnh.csv');       % Load Tx magnitude for all points on slide
pha=csvread('035-3Phnh.csv');       % Load Tx phase for all points on slide
Glass=load('Glassref.mat');         % Load glass slide material properties
Glassn=Glass.n;
Glassalph=Glass.alph;

nmin=0;             % Minimum for swept refractive index
nmax=9;             % Maximum for swept refractive index
nsteps=100;         % Number of refractive index steps

alphamin=-50;       % Minimum for swept absorption coefficient (1/cm)
alphamax=150;       % Maximum for swept absorption coefficient (1/cm)
alphasteps=600;     % Number of absorption coefficient steps

refinesteps=50;     % Number of refinements in second step
freqsteps=350;      % Cutoff for frequency range (~2.5 THz)
numpoints=15;       % Number of points included in Tx data

dglass=1.0365;      % Thickness of glass sublayer in mm
dsample=0.0095;     % Thickness of tissue sample im mm

nbg=1+j*0;          % Refractive index of background material (air)
```

```
clear n alph

% Solve for each point for which Tx data is loaded
for point=1:numpoints

waven=mag(:,1);                 % Frequency range from system
magfreq=mag(:,point+1);         % Tx magnitudes from file
phasefreq=-1*pha(:,point+1);    % Tx phase from file
phasefrequn=unwrap(phasefreq);  % Unwrap Tx phase to be continuous

L=length(waven);

% Expression of Tx signal in exponential form
for ii=1:L
   Enorm(ii)=sqrt(magfreq(ii))*exp(j*phasefreq(ii));
end

% Solve at each frequency
for stat=1:freqsteps

% Define range of n and alpha
nrange=nmin:(nmax-nmin)/(nsteps):nmax;
alpharange=alphamin:(alphamax-alphamin)/(alphasteps):alphamax;

clear tx1 phasediff transmitted zerobalance
clear zerobalancereal zerobalanceimag zerobalancetotal
clear zerobalancereal2 zerobalanceimag2 zerobalancetotal2

% Set glass parameters at frequency
nglass=Glassn(stat)-j*1/(2*2*pi*waven(stat))*Glassalph(stat);

zeromin=1;
refnindex=1;
alphindex=1;

% Solve across range of n and alpha
for nn=1:nsteps+1
   for aa=1:alphasteps+1
      nreal=nrange(nn);
      cn=nreal-j*1/(2*2*pi*waven(stat))*alpharange(aa);
      gamma1=j*2*pi*waven(stat)*100*nbg;
      gamma2=j*2*pi*waven(stat)*100*nglass;
      gamma3=j*2*pi*waven(stat)*100*cn;

      tx1(nn,aa)=(2*cn*(nglass+nbg)/((cn+nbg)*(cn+nglass)));
      phasediff(nn,aa)=exp(-1*(gamma3-gamma1)*dsample*1e-3);
```

```
      phasenorm(nn,aa)=-1*(gamma3-gamma1)*dsample*1e-3;

      reflect23(nn,aa)=(cn-nbg)/(cn+nbg)*exp(-2*gamma3*dsample*1e-3);

      reflect12(nn,aa)=((nglass-cn)+(nglass+cn)*reflect23(nn,aa))/...
                  ((nglass+cn)+(nglass-cn)*reflect23(nn,aa))*...
                  exp(-2*gamma2*dglass*1e-3);

      internal1(nn,aa)=1/(1+(nglass-cn)/(nglass+cn)*reflect23(nn,aa));
      internal2(nn,aa)=1/(1+(nbg-nglass)/(nbg+nglass)*reflect12(nn,aa));
      internalref(nn,aa)=1+((nbg-nglass)*(nglass-nbg)/((nbg+nglass)^2)*...
                    exp(-2*gamma2*dglass*1e-3));

      transmitted(nn,aa)=tx1(nn,aa)*internal1(nn,aa)*internal2(nn,aa)*...
         internalref(nn,aa);
      transmitphase(nn,aa,stat)=angle(transmitted(nn,aa));

      % Magnitude and phase error
      zerobalancereal(nn,aa)=real(log(transmitted(nn,aa)))+...
         real(phasenorm(nn,aa))-log(sqrt(magfreq(stat)));
      zerobalanceimag(nn,aa)=imag(log(transmitted(nn,aa)))+...
         imag(phasenorm(nn,aa))-phasefrequn(stat);

      % Total error
      zerobalancetotal(nn,aa)=zerobalancereal(nn,aa)+...
         i*zerobalanceimag(nn,aa);

      if abs(zerobalancetotal(nn,aa))<zeromin;
         zeromin=abs(zerobalancetotal(nn,aa));
         refnindex=nn;
         alphindex=aa;
      end
   end
end

% If within the limits of the initial range, refines the solution
if (refnindex~=1)&&(refnindex~=nsteps+1)&&(alphindex~=1)&&...
      (alphindex~=alphasteps+1)

nrange2=nrange(refnindex-1):(nrange(refnindex+1)-...
   nrange(refnindex-1))/refinesteps:nrange(refnindex+1);
alpharange2=alpharange(alphindex-1):(alpharange(alphindex+1)-...
   alpharange(alphindex-1))/refinesteps:alpharange(alphindex+1);
refnindex2=26;
alphindex2=26;
```

```
for nn2=1:(refinesteps+1)
   for aa2=1:(refinesteps+1)
      nreal=nrange2(nn2);
      cn=nreal-j*1/(2*2*pi*waven(stat))*alpharange2(aa2);
      gamma1=j*2*pi*waven(stat)*100*nbg;
      gamma2=j*2*pi*waven(stat)*100*nglass;
      gamma3=j*2*pi*waven(stat)*100*cn;

      tx12(nn2,aa2)=(2*cn*(nglass+nbg)/((cn+nbg)*(cn+nglass)));
      phasediff(nn2,aa2)=exp(-1*(gamma3-gamma1)*dsample*1e-3);
      phasenorm(nn2,aa2)=-1*(gamma3-gamma1)*dsample*1e-3;

      reflect232(nn2,aa2)=(cn-nbg)/(cn+nbg)*exp(-2*gamma3*dsample*1e-3);
      reflect12(nn2,aa2)=((nglass-cn)+(nglass+cn)*reflect232(nn2,aa2))/...
                  ((nglass+cn)+(nglass-cn)*reflect232(nn2,aa2))*...
                  exp(-2*gamma2*dglass*1e-3);

      internal12(nn2,aa2)=1/(1+(nglass-cn)/(nglass+cn)*reflect232(nn2,aa2));
      internal22(nn2,aa2)=1/(1+(nbg-nglass)/(nbg+nglass)*reflect12(nn2,aa2));
      internalref2(nn2,aa2)=1+((nbg-nglass)*(nglass-nbg)/((nbg+nglass)^2)*...
                   exp(-2*gamma2*dglass*1e-3));

      transmitted2(nn2,aa2)=tx12(nn2,aa2)*internal12(nn2,aa2)*...
         internal22(nn2,aa2)*internalref2(nn2,aa2);
      transmitphase2(nn2,aa2,stat)=angle(transmitted2(nn2,aa2));

      zerobalancereal2(nn2,aa2)=real(log(transmitted2(nn2,aa2)))+...
         real(phasenorm(nn2,aa2))-log(sqrt(magfreq(stat)));
      zerobalanceimag2(nn2,aa2)=imag(log(transmitted2(nn2,aa2)))+...
         imag(phasenorm(nn2,aa2))-phasefrequn(stat);
      zerobalancetotal2(nn2,aa2)=zerobalancereal2(nn2,aa2)+...
         i*zerobalanceimag2(nn2,aa2);

      if abs(zerobalancetotal2(nn2,aa2))<zeromin;
         zeromin=abs(zerobalancetotal2(nn2,aa2));
         refnindex2=nn2;
         alphindex2=aa2;
      end
   end
end

   n(stat,point)=nrange2(refnindex2);
   alph(stat,point)=alpharange2(alphindex2);
   waven(stat);

else
```

```
    n(stat,point)=nrange(refnindex);
    alph(stat,point)=alpharange(alphindex);
    waven(stat);

end
end
end

% Output n and alph is a 2D array of the n and alpha at each point for each frequency
```